Reactive Molecular Dynamics of Network Polymers: Generation, Characterization and Mechanical Properties

by

Chandrashekar Shankar

A dissertation submitted in partial fulfillment
of the requirements for the degree of
Doctor of Philosophy
(Materials Science and Engineering)
in The University of Michigan
2009

Doctoral Committee:

Professor John Kieffer, Chair
Associate Professor Eitan Geva
Assistant Professor Joerg Lahann
Professor Michael Falk, Johns Hopkins University

To

Amma, Baba, Malini and Vinayak

Acknowledgements

I would like to thank my advisor Prof. John Kieffer for many useful discussions and financial support. Also special thanks to my friends Dr. Arun Kumar Upadayay, Dr. Liping Huang, Dr. Yunfeng Shi, Changgua Zhen and Dr. Natalia Gorska for many intellectually stimulating conversations and copious research help without which this thesis could not have been completed. I am forever indebted to my family specially Amma, whose constant support and encouragement made things brighter when I was not in the best of moods and Baba for his deep love of science and inculcating the same in me and my siblings. Kudos to all the staff, notably Kevin Worth and Renee Hilgendorf at the MSE department for their untiring efforts that have helped resolve many a sticky situation and for creating a family like atmosphere. Hi fives to the many friends and companions who have shared my love of the outdoors. I will remember fondly the merry times during the many adventures, escapades and assorted shindigs we got ourselves into, thank you all for lifetime of memories, smiles, jokes and camaraderie. Lastly I would to felicitate the entire Inter-Cooperative Council (ICC) for being the most awesome housing organization. Bureaucracy aside, living in ICC houses has lead me to lasting friendship, excellent adventures and a diverse network of friends in every corner of the world.

Table of Contents

List of Figures

List of Tables

List of Appendices

List of Abbreviations

Å	Angstrom
A_{ij}	Simulation box area in the ij plane
CAC	Center for advanced Computing
CG	Coarse Grained
COM	Center of Mass
COMPASS	Condensed-phase Optimized Molecular Potentials for Atomistic Simulation Studies
d	Graph fractal dimension
D	Fick's diffusion coefficient
DC	Diamond cubic
DCPD	Di-cyclo-penta-diene
DSC	Differential Scanning Calorimetry
E	Young's Modulus
fs	Femto-second = 10^{-15} seconds
FTIR	Fourier Transform Infrared Spectroscopy
FLX	In-house MD code with reactive potentials
GHz	Gigahertz
G^{affine}	Affine theory Shear modulus
$G^{phantom}$	Phantom theory Shear modulus
HDPE	High density polyethylene
ΔH_R	Enthalpy change of reaction
$H_{products}$	Enthalpy of products

$H_{reactants}$	Enthalpy of reactants
J	Diffusion Flux
K	Bulk Modulus
k_b	Boltzmann’s constant
LAMMPS	Large-scale Atomic/Molecular Massively Parallel Simulator
LJ	Lennard Jones
MD	Molecular dynamics
MC	Monte Carlo
MM2	Moelcular Mechanics 2
MPa	Mega Pascal
M_x	Molecular mass between cross-links
N	number of nodes in a network
N_A	Avogadro’ number
ps	pico-second $=10^{-12}$ seconds
P	Hydrostatic pressure
PE	Poly-ethylene
$P(r,n)$	Probablity function for end to end distances
PET	Poly ethylene terepthalate
PBC	Periodic boundary conditions
PCF	Pair Correlation Function
Q_X	Concetration of species with X bonds
R	Gas Constant
RAND	Random
R_c	Reaction cutoff distance
RDF	Radial Distribution Function
ROMP	Ring Opening Metathesis Polymerization
rRESPA	reversible Reference System Propagator
S	Entropy

$S(r)$	Number of nodes reachable in exactly r edge moves of a central node
S_N	Number of surface node that divides a PBC simulation box into 2 disjoint parts
SW	Stillinger-Weber potential
T	Temperature
V	Volume
$V(r)$	Number of nodes reachable in less than r edge moves of a central node
VLE	Vapor Liquid Equilibria
XRD	X-Ray Diffraction
ZPE	Zero Point Energy
ΔH_{vap}	Heat of Vaporization
ε	Interaction energy for Lennard Jones systems
ε_k	Strain in the k direction
ρ	Density
σ	Sigma parameter for Lennard Jones systems
σ_{jk}	Stress tensor component in the jk dimension
λ_i	Simulation box extension ratio in the i direction
μ	Cross-links per unit volume
τ	Coarse grained MD simulation time unit
τ_1	Time constant for first order rate reaction
τ_2	Time constant for first order rate reaction
ψ	Fractional coefficient in rate equation
ζ	Fractional coefficient in rate equation

Abstract

This work is an effort to understand the mechanical properties of the catalytically cross-linked polymer system, created by the ring opening metathesis polymerization (ROMP) of dicyclopentadiene (DCPD). This system is used as a healing agent in a novel self-healing material that promises much improvement in reliability and performance of polymer composites.

We used multi-scale molecular simulation methods, including coarse-grained and fully atomistic molecular dynamics (MD) simulations to generate realistic structures of DCPD networks, characterized their structures, and determined their mechanical properties. Using density functional theory (DFT) calculations, complemented by structural information derived from molecular dynamics simulations we reconstruct experimentally observed Raman spectra and differential scanning calorimetry (DSC) data, allowing us to identify details about the ROMP reaction mechanisms and the temporal evolution of chemical species during this process. These insights along with information from experimental studies helped formulate the reactive molecular simulation algorithm we developed for this investigation.

We performed coarse-grained simulations of networks generated via the ROMP reaction process and compared them to those generated via a process in which bonds between network nodes are formed randomly (RANDOM reaction process). This

comparison led us to the fundamental realization that the polymerization process has a unique influence on the network topology, as understood by the distribution of bonds between structural units, and accordingly, results in a unique mechanical response of the structure. The insights generated from our coarse grained models particularly the maximum extent of reaction achieved were then used to parameterize the reaction process for the atomistic simulations.

To generate more realistic cross-linked networks we carried out fully atomistic simulations of DCPD using a novel algorithm for recreating ROMP reactions between DCPD molecules. We found that the mechanical properties derived from these atomistic networks are in excellent agreement with those obtained from our coarse-grained simulations in which interactions between nodes are subject to angular constraints. This comparison provided self-consistent validation of our molecular simulation results, and helped to identify the level of detail necessary for the coarse-grained interaction model.

Based on the understanding we gained from our simulation investigation, we propose a classification of networks into three distinct stages of cure: fluid-like, rubber-like or glass-like. In each stage the polymer system exhibits a different predominant mechanical response to deformation at low degrees of reaction the system tends to flow and fluid mechanics becomes relevant, at intermediate stages the mechanical response is entropic or is solely due to structural rearrangements with no change in internal energy and at high degree of reaction the mechanical behavior is enthalpic or due to change in internal energy..

Lastly we developed graph theory-based network characterization approaches to correlate observed mechanical properties with network topologies. We calculate four different graph theory-based quantities: 1) eigenvector centrality of nodes, which is a measure of the importance of a particular node within a network, 2) graph fractal dimension, which is a dimension that depends solely on the connectivity of the graph, 3) Fiedler or Laplacian partitioning of networks to calculate the fraction of cut bonds in order to split the graph into two disconnected sub-graphs, and 4) The fraction of cross-linkers in a network which is the sum Q_3 and $Q_{4.}$ species in the network. Of these quantities we find that the Fiedler partition method is the best characteristic for the prediction of Young's Modulus.

These computational methodologies and characterization tools can also be applied to study other networked systems, such as epoxies that lie between the boundaries of glass and polymer science and therefore are of great fundamental and practical interest.

Chapter 1
Introduction

1.1 Motivation

Self-healing materials are a new frontier in the polymer materials, capable of healing damage from environmental conditions or applied loads. These therefore have tremendous potential to enhance the performance of polymer matrix composites in applications that are prone to subcritical fatigue crack growth. For example, highly cross-linked polymers exhibit a tendency to undergo brittle fracture, unlike many metals that generally exhibit significant plasticity before complete failure. This catastrophic failure behavior has been a serious impediment in the wider use of polymer composites in critical load bearing structures such as a bridge spans, pressure vessels and aircraft wings etc. Self-healing ameliorates the catastrophic failure modes of the polymer matrices by healing micro-cracks as they appear in the system, increasing lifespan and decreasing the need for non-destructive testing such as ultrasonic testing (UT) and servicing requirements as a result.

The purpose of our investigations into self-healing behaviors is to understand at a molecular level the kinetics with which structural integrity is restored in a new class of self-healing materials, first synthesized by White et al. [1]. A schematic of this system is shown in Figure 1.1. The epoxy polymer matrix contains healing agent filled microcapsules with specially engineered shells that break when a crack approaches them. The microcapsules themselves act as stress concentrators nudging emerging cracks in the matrix towards themselves. After the shell of the capsule is breached the healing agent flows out into the crack due to capillary effects. The epoxy matrix also contains pre-embedded catalyst particles. These catalyst particles are exposed at the crack surfaces and promote the healing process after coming in contact with the healing agent. The healing agent is a monomer that upon polymerization and cross-linking bonds to the crack surfaces to restore mechanical cohesion in the matrix when the material is in an unstressed state during the load cycle.

In Figure 1.2 the load displacement curves of a virgin and a self-head specimen tested by White et al. [1] are shown, revealing almost total recovery of mechanical integrity due to the action of the self-healing system. Figure 1.3 shows the change in healing efficiency with time, defined as.

$$\eta = \frac{K_{Ic}^{healed}}{K_{Ic}^{virgin}}, \tag{1.1}$$

where K_{Ic} is the mode-I fracture toughness, generally measured by pulling a specimen perpendicular to a notch of standard depth. K_{Ic} is determined by measuring the failure stress at which crack propagation takes place by using the formula below

$$K_{Ic} = \sigma_f \sqrt{\pi a} \tag{1.2}$$

where σ_f is the failure stress and a is the depth of the notch.

The self-healing system developed by White et al. [1] involves a healing agent, initially in monomer form, and a catalyst. The healing agent they chose is dicycopentadiene (DCPD) and the catalyst is a first generation Grubb's catalyst that mediates the ring opening metathesis polymerization (ROMP) of DCPD under ambient conditions. The system was chosen for its chemical stability and the high modulus of the fully cured resulting polymer. In Section 1.2 we explore the chemistry of endo and exo isomers of DCPD that show differing reactivities for ROMP reaction. We can use these differences in reactivity to create mixtures of isomeric DCPD molecules, that along with carefully chosen catalyst concentrations and careful design of catalyst sensitivity to reaction sites in differing molecules, can be used in order to create self healing reaction mixtures which can cure in as little as a few minutes to a few hours [2] with final mechanical properties tailored to meet specific requirements from rubbery solids that have a low crosslink density achieved by inhibiting the cross-linking reaction to tough epoxy like matrices by ensuring that the cross-linking reaction occurs with high probability

1.2 Ring opening metathesis reaction (ROMP)

Ring opening metathesis polymerization or ROMP as it is commonly known is a new olefin polymerization technique that was first discovered in 1971 by Hérisson and Chauvin [3] during their work on Tungsten compounds and later by Schrock et. al in 1980 [4] while investigating Tungsten and Molybdenum based compounds. Their seminal contributions were followed by Grubbs and Tumas in 1989 [5], who discovered Ruthenium based catalysts that were more selective than the previous generation catalysts in olefin metathesis. For their contributions to metathesis chemistry Yves Chauvin, Robert H. Grubbs and Richard R. Schrock were awarded the Nobel Prize for Chemistry in 2005. Since those early days the field of olefin metathesis has exploded with many new catalysts mostly based on heavy transition metals such as Nickel, Tungsten, Ruthenium and Molybdenum. Each of these catalysts has either different reactivity or selectivity to different substrates or show unique behavior after exposure to specific solvents [6].

Typically Grubb's catalysts appear in two varieties commonly termed as first generation and second generation catalysts, Figure 1.4 shows a typical first generation Ruthenium based Grubbs catalyst, which is more stable to moisture and oxygen than the second generation catalyst which is more reactive. Typically a ROMP reaction is initiated by the Metal carbene $M=C$ species attacking a strained $C=C$ double bond in a carbon ring forming a highly unstable metallo-cyclo-butane intermediate. The unstable intermediate then exchanges its double bonds and falls open due to ring strain giving the beginnings of a linear chain. The polymer now also contains a linear chain double bonded to the catalytic metal with a terminal double bond as well. The new $M=C$ bond can now further react with the double bonds on the next monomer, thus propagating the reaction, giving rise to so-called living tip polymerization as shown in Figure 1.5.

One of the advantages of ROMP olefin metathesis is its specificity and stability in moist or oxygen rich conditions that other free radical type living tip reactions cannot function in. ROMP reactions also create monodisperse polymer chains in linear polymers since each living tip generally grows at the same rate. ROMP catalysts can also be functionalized to allow only stereo specific products such as *cis* only or *trans* only configurations to form. Second generation Grubbs catalysts however are not stereo specific and react without prejudice to form both *cis* and *trans* compounds, whereas first generation catalysts show slight stereo selectivity with the *trans* conformer product being formed 87% of the time in linear polymerizations of DCPD[7]. Due to their environmental stability second generation Grubb's catalysts have found industrial use in synthesizing mono-disperse high-strength linear polymers with inexpensive reactants or as a method to make specialty compounds with tailored properties[8]. Organic chemists consider metathesis reactions an important accoutrement in their arsenal of available molecular reaction tools to achieve synthesis goals.

1.3 ROMP of DCPD

We focus on a specific application of ROMP of dicyclopentadiene (DCPD) in the synthesis of cross-linked networks for use in self-healing materials. The substrate DCPD occurs in 2 major conformations endo and exo DCPD as shown in Figure 1.6 The molecule consists of a 5 membered ring called the cyclo-pentene ring and a 6 member bicyclic ring with a buckled carbon across the middle, generally described as the norborene ring in literature. Both rings contain strained double bonds and are candidate sites for ROMP reaction. Since the driving force for ROMP is due to the ring strain it is thought that the norborene ring in both endo and exo DCPD is more reactive than the cyclo-pentene double.

It is however known from kinetic studies that the exo-DCPD has higher reactivity than the endo-DCPD conformer during ROMP. This reactivity difference is thought to be due to difficulties in steric access to the reaction sites in the endo DCPD as compared to the exo DCPD conformer [9,10]. But there is a lack of experimental techniques capable of probing these differences. We will clarify these questions in Chapter 2 using DFT simulations.

Recent experimental work by Schaubroeck et al.[11] explores the extent of reaction at each of the two reaction sites i.e. the cyclo-pentene and norborene double bond on a single DCPD molecule in exo-DCPD. They show that the norborene preferentially reacts and then masks the signal of the cyclo-pentene ROMP reaction due to the release of cyclo-pentene ring strain. Intuition from these experimental results along with DFT simulation data in Chapter 2 will shape the simulation effort in subsequent chapters. The DFT simulation elucidates the reaction process and thereby the mechanical response evolution of the network with change in its degree of reaction. On the other hand a well known non-contact technique that can probe modulus behavior during the curing process is Brillion spectroscopy, which uses inelastic light scattering phenomena on acoustic phonons to probe the shear and loss modulus at high frequencies. The high frequency modulus behavior can then be extrapolated to low frequency for comparison with experiments and simulations. Such experiments have been performed for end-linked polydimethylsiloxane (PDMS) measuring a longitudinal loss modulus M [12]. The longitudinal modulus M is a combination of the bulk and shear modulus given below

$$M = K+4G/3 \tag{1.3}$$

where K is the bulk modulus and G is the shear modulus. These measurements show a linear dependence of M on the inverse of chain length as predicted by polymer theories discussed below.

1.4 Physics of Cross-linked Networks: Are they Polymers or Glasses?

There are fundamental questions that need clarification in the cross-linking reactions of DCPD with ROMP process. They involve a deeper investigation of how network formation affects mechanical properties.

Simulations of cross-linked networks are a nascent and exciting field that holds vast promise for materials design and processing. Today organic chemistry with its myriad of processes and catalytic techniques have broken new ground in creating new organic polymer macromolecules such as high-density polyethylene (HDPE), poly ethylene terepthalate (PET) and many other industrially significant molecules. This large palette of molecules exhibits widely differing properties and is subject to intense research. Fundamentally materials derive their mechanical response to deformation from 2 different mechanisms. 1) The enthalpic effects due to changes in molecular structure mainly characterized by deformation in bonds, angles and dihedrals that result in a change in the internal energy of the molecule and 2) entropy effects due to reduction in the macromolecular conformational space available resulting from deformation.

A large volume of theoretical and simulation efforts in the last fifty years focused on mechanical properties of rubbery networks fundamentally beginning with the assumption that the elastic properties of networks are a consequence of underlying molecular chains behaving as entropic springs [13] i.e. the mechanical properties solely arise from the fluctuation of chains that is expressed as a configuration entropy. These chain fluctuations are constrained after mechanical deformation leading to differences in entropy. At their very core such theories are based on the fact that polymer strands in their unstrained states exhibit a Gaussian distribution of the end-to-end vectors above the glass transition temperature given by

$$P(r,n) = 4\pi r^2 \left(\frac{2nb^2\pi}{3}\right)^{-3/2} \exp\left(\frac{-3r^2}{2nb^2}\right), \tag{1.4}$$

where $P(r,n)$ is the probability of finding the end-to-end distance of a chain of n segments equal to a distance r. Here b is the segment length, which can be thought of as a rigid bond connecting 2 backbone carbons. The entropy of the chain can then be represented as

$$S = k_B \ln \Omega \approx k_B \ln(P(r,n)). \tag{1.5}$$

The work done is equivalent to the change in the Helmholtz free energy,

$$fdr = d(U - TS). \tag{1.6}$$

Neglecting change in internal energy we therefore get

$$f = \frac{3k_B T}{nb^2} r \tag{1.7}$$

From classical theories ensembles of such chains at constant volume can be shown to have an elastic modulus at constant volume given by

$$Y = \frac{3\rho k_B T}{M_x}, \tag{1.8}$$

where ρ is the density of the polymer and M_x is the average molecular weight between cross-links. It must be noted that such theoretical formulations are generally applicable when the network is characterized by a low concentration of cross-links or equivalently large chain lengths between cross-links.

A large amount of literature in polymer science is devoted to the analysis of the entropic effects, starting with the seminal work of theoretical polymer physics by Wall [14] and Flory [13] that laid down the statistical mechanics and thermodynamic foundations of understanding polymer behavior. These theories explain the origins of mechanical properties such as the shear and Young's modulus, thermal properties such as heat capacity and conductivity, and other physical properties such as swelling behavior in the presence of solvents using statistical thermodynamic ideas.

Two of the earliest theoretical explanations of network mechanical behavior are the affine model [13] as suggested by Flory and Wall and the phantom model [15] by James and Guth. Both these theories assume that elastically active strands pass freely through their neighbors as if they did not exist. These two theories differ in their assumptions of the nature of cross-linking sites. In the small deformation limit the affine model assumes that the cross linkers are positioned at fixed locations on the polymer backbone and predicts a shear modulus according to

$$G^{affine} = vRT \tag{1.9}$$

where v is the number of polymer chains per unit volume. The phantom model on the other hand assumes that the crosslink's are free to move along the network backbone and therefore predicts a shear modulus of

$$G^{phantom} = (v - \mu)RT \tag{1.10}$$

where the number of cross-links per unit volume $\mu = 2v/\phi$, where ϕ is a constant called the network functionality. We note the quantity v increases linearly with the number of cross-links as each cross-link delineates the chains into 2 separate chains. The uncrossability of chains due to excluded volume effects of constituent atoms and entanglement effects is addressed by new theories such as the constrained junction model[16] where physical covalent crosslink impede the motion of the cross links in the phantom model. The constrained junction model predicts a shear modulus that lies in between the predictions of the affine and phantom models and has been shown to better predict behavior of some real networks [17]. Theories such as the reptation model [18] and the tube model [19] explain mechanical properties of non-cross-linked polymers that exceed a phenomenological entanglement length N_e by modeling polymers fluctuating in a constrained tube about their coarse grained backbones. The entanglement length N_e is hard to precisely measure in real linear polymers. The quantity can be estimated from the change in the self-diffusion coefficient D of the polymer as a function of chain length. For small chain length polymers follow a Rouse [20] like regime where $D \sim N^{1}$ and at long chain length enter a new regime where $D \sim N^{-2}$. The crossover between these 2 regimes is expected at the entanglement length N_e. The above theories are thought to be valid for cross-linked polymers such as rubbers that exhibit sparse population of physical cross-links and behave like linear chains between them.

In the special case where cross-links form a significant proportion of the bonds in a network system, such approximations of network behavior modeled after rubbery networks may no longer be valid. Thorpe [21] suggests that the elastic properties of random networks depend primarily on $\langle r \rangle$: the mean atomic coordination number. Thorpe's simulation efforts led to the introduction of the concept of rigidity percolation for network glass systems such as $Ge_xAs_ySe_{1-x-y}$. Mixtures of Ge, As, Se afford a wide range of glass forming compositions due to the large variability of the values of x and y as a result of the polyvalence of these elements particularly their ability to form π and σ bonds. Accordingly, $Ge_xAs_ySe_{1-x-y}$ glasses can be modeled as a continuous random network, where the number of bonds emanating from each node, i.e., the Ge, As, or Se atoms, can be two, three, or four depending on the covalent coordination of that node. These networks show abrupt monotonic increase in values of physical properties such as the bulk modulus after a mean coordination number of $\langle r \rangle = 2.4$, which defines the so-called rigidity percolation threshold.[22]

Polymer macromolecules such as highly cross-linked polymers, therefore, may not entirely follow the entropy driven elastic response to deformation as suggested by the theories mentioned. A deformation in highly cross-linked network polymer implicitly has large energy barriers to network conformational changes and therefore has no easily accessible relaxation pathway to relieve the stress caused by a deformation. It therefore plausible that its response is enthalpic, namely an increase in internal energy due to deformation in bonds lengths, angles and dihedrals. This effect is rarely studied in the literature due to difficulties in recreating network structure of highly cross-linked networks. Cross-linked covalent network polymers therefore could behave less like long chain polymers and more like network glasses. It is to be noted however that even linear polymers exhibit an enthalpic response to deformation at temperatures below T_G since macroscopic chain conformation changes are energetically inaccessible and therefore only the enthalpic response is available for deformations. Polymer properties are heavily dependent on processing conditions that affect the properties such as the degree of crystallanity. Amorphous polymers such as PE can also be created via catalytic processes in forms such as high density polyethylene (HDPE), which has a high degree of crystallinity and consequently exhibits remarkable properties such as high strength and modulus that are an order of magnitude higher than polyethylene (PE).

On the other hand, in glass theory the prevailing consensus suggests low or zero shear modulus below the percolation threshold defined by a critical coordination number. The shear modulus increases after the percolation threshold in a linearly and monotonic fashion. Figure 1.7 schematically explains the differences in opinion between the glassy theories and the polymer theories.

Network or cross-linked polymers form a special class of polymeric materials that over the years have delivered improvements in properties such as impact resistance, hardness, elastic properties and durability as compared to linear polymers. The term network polymers encompasses a variety of molecules ranging from sparsely cross linked rubbers where the relatively short cross links connecting two backbone strands may occur on the polymer backbone carbon chain at a frequency of the order of 1 in 10000 atoms as in natural rubber, to highly cross-linked epoxy resins where cross linking may occur every 5 or even fewer carbon atoms. In the latter case differentiating the underlying network into backbones and cross links becomes irrelevant since the size of the backbones become comparable to the size of the cross-links.

The deformation response of networks can be explained by 2 competing theories: a) polymer theories that assume no change in internal energy and b) glassy theories that predominantly (but not totally) work under the opposite assumption. We will delineate the state of the networks and deformation regimes to elucidate the factors that affect the applicability of the above theories. Even though there is sufficient evidence that glassy solids exhibit entropic or non affine response to deformation, in this work we will refer to networks that exhibit internal energy change in response to deformation as “glassy.”

This work focuses on the creation, characterization and mechanical properties of network polymers. Chapter 2 explores the chemistry of the ROMP of DCPD using DFT simulations, Chapter 3 is an excursion into coarse-grained models of networks. Chapter 4 explores the generation and mechanical properties of all atomistic networks of DCPD. Chapter 5 shows comparisons between coarse-grained networks, atomistic networks and experimental observations. Chapter 6 is a foray into characterization of networks using graph theory ideas and correlations to mechanical properties. Finally Chapter 7 summarizes the salient results and conclusions.

1.5 Figures

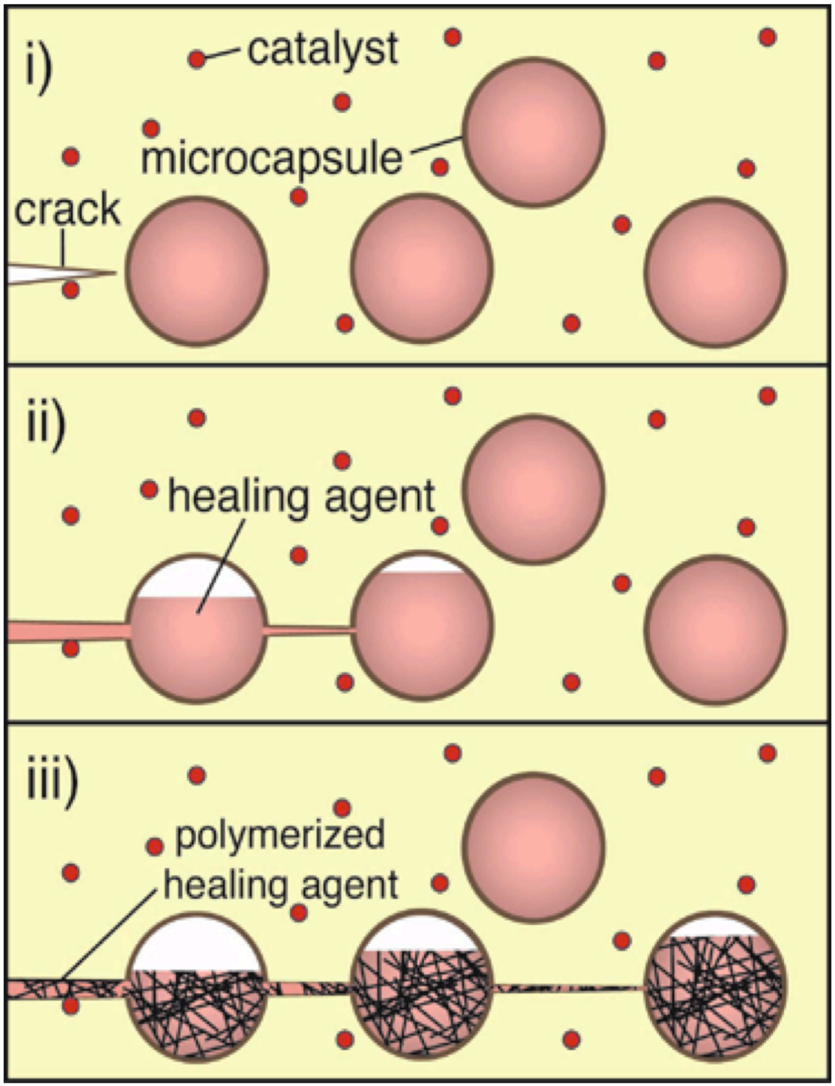

Figure 1.1: Self healing reaction mechanism i) Microcapsules act as stress concentrators. ii) Crack breaches capsule, monomer flows out due to capillarity. iii) Exposed catalyst on crack surface initiates polymerization and healing.

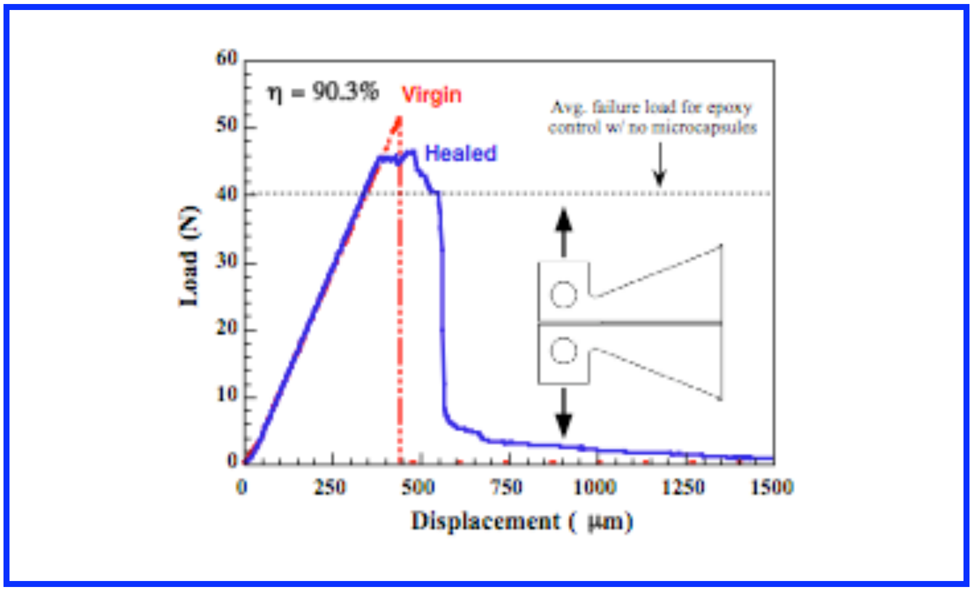

Figure 1.2: Load displacement data of self healing polymer matrix. Red dotted plot for virgin matrix with healing mirocapsules, Blue curve after failure and subsequent self healing via ROMP of DCPD. White et al[1]

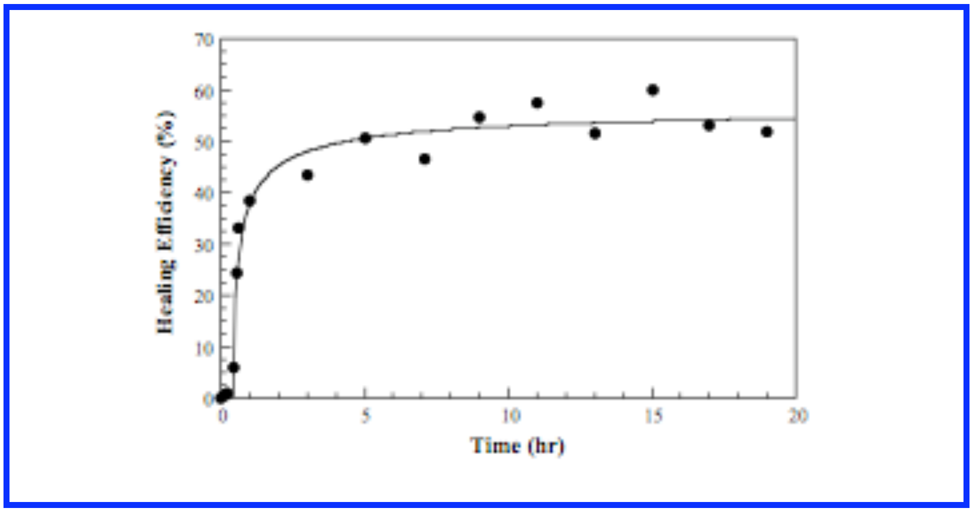

Figure 1.3: Healing efficiency development as a function of time. Curves is a guide to the eye. Healing efficiency or mechanical recovery increases rapidly as the healing time is increased and plateaus out after about 5-6 hours.White et al[1]

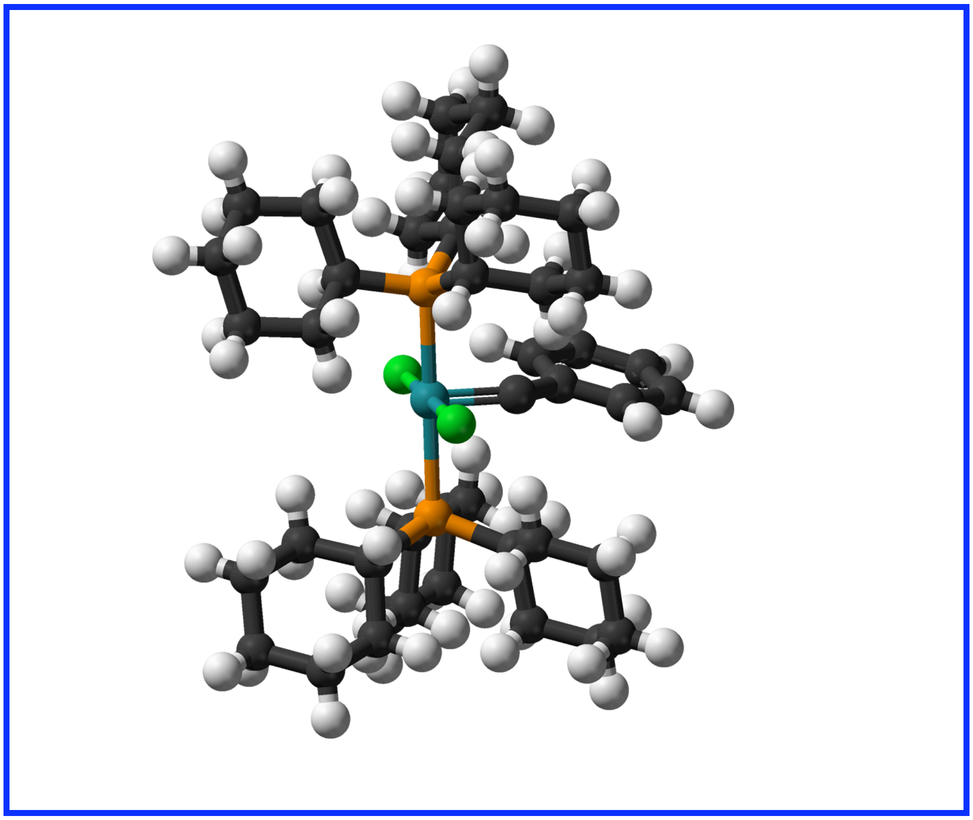

Figure 1.4: First generation ROMP catalyst structure: Green = Chlorine, White = H, Blue = Ruthenium, Black = Aromatic Carbon, Orange = Aliphatic Carbon. The Ruthenium atom is connected via a double bond to an aromatic carbon. This double bond is the ROMP active double bond. Source: http://upload.wikimedia.org/wikipedia/commons/a/aa/Grubbs-1G-3D-balls.png.

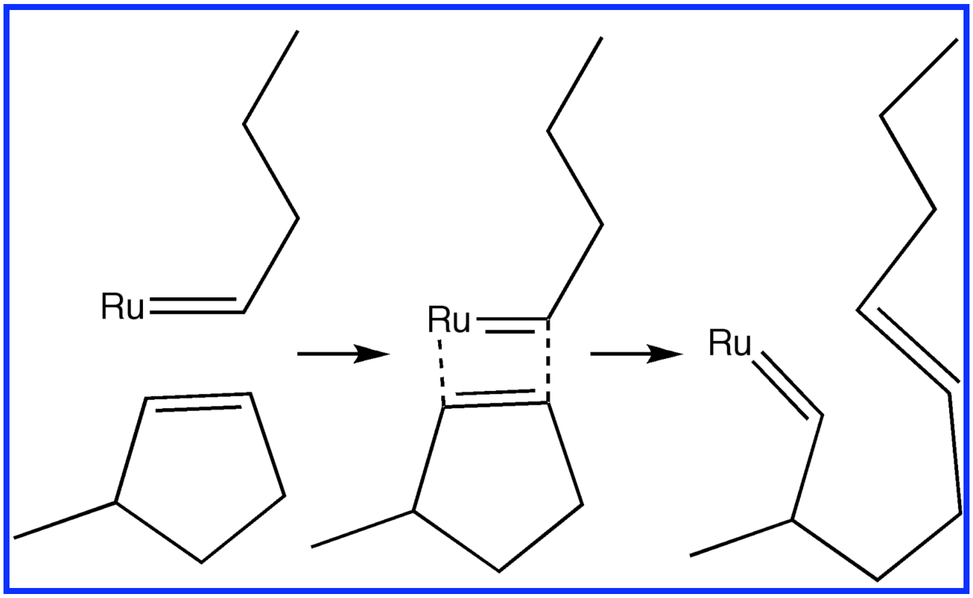

Figure 1.5: ROMP mechanism for strained rings. The Ruthenium catalyst as shown in Figure 1.4 exchanges the original double bond it is connected to with other double bonds, creating a living tip that continues the polymerization reaction. The exchange of double bonds releases ring strain, which is the driving force for ROMP reactions.

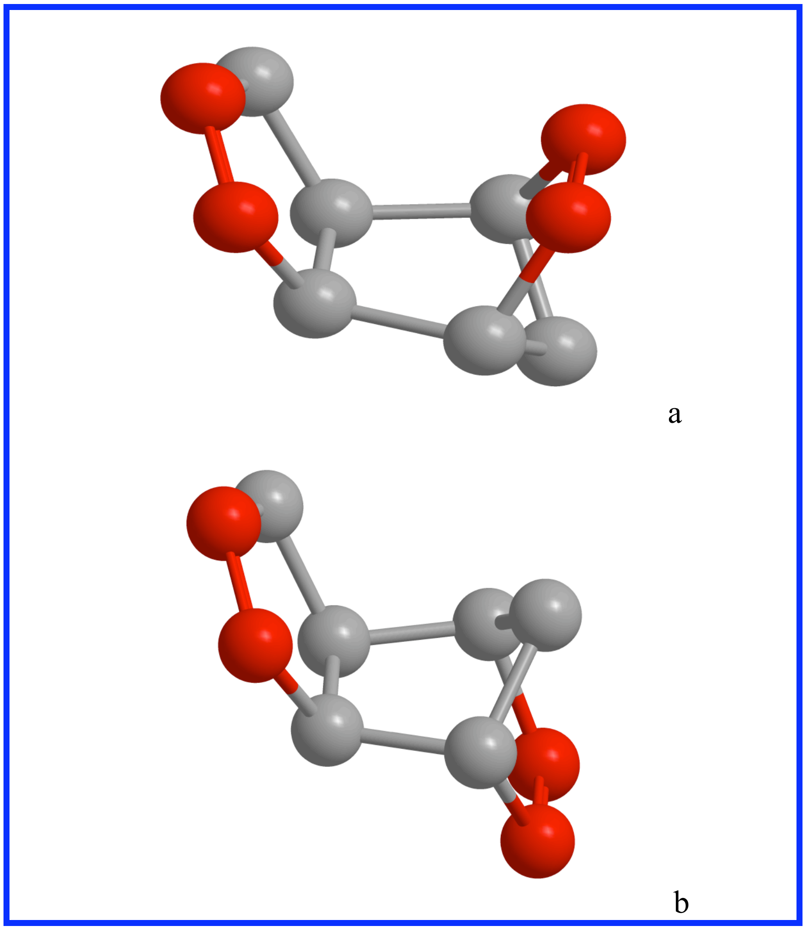

Figure 1.6: a) endo-DCPD and b) exo-DCPD. The red atoms are sp_2 hybridized carbons and the grey atoms are sp_3 hybridized carbons. Hydrogens are not shown for clarity. The exo DCPD is an armchair conformer, whereas the endo DCPD appears as a boat conformer.

Figure 1.7: Glass theories and polymer theories of modulus. The Glassy theories predict rigidity percolation at a degree of reaction ~0.6 and the Polymer theories show a modulus proportional to the crosslink density. Cross-ink density itself follows a increasing function with given degree of reaction. The curves are ad-hoc representations of expected modulus behavior.

1.6 References

1. White, S. R. et al. Autonomic healing of polymer composites. *Nature* **409**, 794-797 (2001).

2. Mauldin, T. C., Rule, J. D., Sottos, N. R., White, S. R. & Moore, J. S. Self-healing kinetics and the stereoisomers of dicyclopentadiene. *Journal of The Royal Society Interface* **4**, 389-393 (2007).

3. Herisson, P. J.-L. & Chauvin, Y. Catalyse de transformation des olÈfines par les complexes du tungstËne. II. TÈlomÈrisation des olÈfines cycliques en prÈsence d'olÈfines acycliques. *Die Makromolekulare Chemie* **141**, 161-176 (1971).

4. Schrock, R. R., Rocklage, S. M.,Wengrovius J. H.,Rupprecht G., Fellmann, J. Preparation and Characterization of Active Niobium, Tantalum, and Tungsten Metathesis

Catalysts. *J. Molec. Catal.* **8**, 73- (1980).

5. Grubbs, R. H. & Tumas, W. Polymer synthesis and organotransition metal chemistry. *Science* **243**, 907-915 (1989).

6. Mutch, A., Leconte, M., Lefebvre, F. & Basset, J.-M. Effect of alcohols and epoxides on the rate of ROMP of norbornene by a ruthenium trichloride catalyst. *Journal of Molecular Catalysis A: Chemical* **133**, 191-199 (1998).

7. Amir-Ebrahimi, V., Corry, D. A., Hamilton, J. G., Thompson, J. M. & Rooney, J. J. Characteristics of RuCl2(CHPh)(PCy3)2 as a Catalyst for Ring-Opening Metathesis Polymerization. *Macromolecules* **33**, 717-724 (2000).

8. Mol, J. C. Industrial applications of olefin metathesis. *Journal of Molecular Catalysis A: Chemical* **213**, 39-45 (2004).

9. Rule, J. D. & Moore, J. S. ROMP Reactivity of endo- and exo-Dicyclopentadiene. *Macromolecules* **35**, 7878-7882 (2002).

10. Mathew, J. P., Reinmuth, A., Melia, J., Swords, N. & Risse, W. (eta(3)-Allyl)palladium(II) and palladium(II) nitrile catalysts for the addition polymerization of norbornene derivatives with functional groups. *Macromolecules* **29**, 2755-2763 (1996).

11. Schaubroeck, D., Brughmans, S., Vercaemst, C., Schaubroeck, J. & Verpoort, F. Qualitative FT-Raman investigation of the ring opening metathesis polymerization of dicyclopentadiene. *Journal of Molecular Catalysis A: Chemical* **254**, 180-185 (2006).

12. Sinha, M., Mark, J. E., Jackson, H. E., Walton, D. & {, c. A Brillouin scattering study of end-linked poly(dimethylsiloxane) networks. *The Journal of Chemical Physics* **117**, 2968-2974 (2002).

13. P.J., F. *Principles of Polymer Chemistry* (Cornell University Press, 1953).

14. Wall, F. T. Statistical Thermodynamics of Rubber. III. *The Journal of Chemical Physics* **11**, 527-530 (1943).

15. James, H. M. & Guth, E. Theory of the Increase in Rigidity of Rubber during Cure. *The Journal of Chemical Physics* **15**, 669-683 (1947).

16. Flory, P. J. & Erman, B. Theory of elasticity of polymer networks. 3. *Macromolecules* **15**, 800-806 (1982).

17. Scherbakov, Y. M. & Grishin, B. S. The theory of the rubber elasticity of ideal networks with entanglements; Application of the theory to the calculation of stresses in real networks. *Rubber Chemistry and Technology* **79**, 94-119 (2006).
18. Gennes, P. G. d. Reptation of a Polymer Chain in the Presence of Fixed Obstacles. *The Journal of Chemical Physics* **55**, 572-579 (1971).
19. Edwards, S. F. The statistical mechanics of polymerized material. *Proceedings of the Physical Society* **92**, 9-16 (1967).
20. Rouse, P. E. A Theory of the Linear Viscoelastic Properties of Dilute Solutions of Coiling Polymers. *Journal of Chemical Physics* **21**, 1272-1280 (1953).
21. Thorpe, M. F. Continuous deformations in random networks. *Journal of Non-Crystalline Solids* **57**, 355-370 (1983).
22. Chubynsky, M. V. & Thorpe, M. F. Self-organization and rigidity in network glasses. *Current Opinion in Solid State and Materials Science* **5**, 525-532 (2001).

Chapter 2
The DCPD System and the ROMP Reaction

2.1 Introduction

Experimental investigations [1] suggest that the differences in reactivity between endo and exo DCPD, shown in Figure 2.1, arise from steric effects. However these assumptions need further scrutiny. It is very difficult to delineate whether a ROMP reaction on a given bond derives its reactivity from steric effects or energetic effects. In the case of steric effects it is assumed that reactivity differences arise due to differences in chemical structure and a given bond is available for ROMP reaction at different rates due to differences in approachability. Reaction enthalpies do not directly affect the reaction kinetics. However, exothermic reactions are more likely to provide the necessary thermal activation and self-acceleration than endothermic reactions do. Moreover, strongly exothermic reactions could be an indication of initial structural states characterized by high potential energies, i.e., they may be relatively unstable and already possess an activation gain. Based on these arguments we assume that reactivity differences between the two reactive sites of the DCPD molecule, in a first approximation, parallels the difference in reaction enthalpies. We note that the heat of reaction of ROMP on each site is due to the ring strain on these bonds. We therefore need to accurately find ring strain energies of the two reaction sites of DCPD.

2.2 DFT of ROMP reaction on DCPD

We use DFT calculations to gain the desired insights into the reaction energetics of the ROMP process for DCPD. These calculations were carried out in collaboration with another Kieffer group member, Changgua Zhen.

Figure 2.2 shows the reaction pathway for ROMP involving the two different reactive sites of DCPD with ethene ($H_2C = CH_2$) molecules. The initial configurations of the endo and the exo structures of the molecules *a, b, c,* and *d* were first generated using ChemDraw3D®, which included relaxation of the structures towards their local ground state energy using a combination of MD and energy minimization based on the inbuilt MM2 potential in ChemDraw3D®. The procedure involved creating a putative structure of the desired molecule and then using energy minimization to create the low energy configuration. We first anneal the molecule at 700 K for 5000 steps for a total time of 50 ps using 0.001 ps time-steps of MD. The annealing step is followed by an energy minimization quench run to generate minimum energy configurations terminated when $\Delta E / E < 10^{-4}$. If the energy of the quenched molecule is lower than the lowest energy configuration from previous annealing and quenching runs, we replace the previous low energy configuration with the new low energy configuration. After ten to fifteen cycles of the above process we can be sure that the low energy configuration chosen is indeed the lowest possible. The low energy configuration for each molecule is then used as the starting point for DFT calculations using the Gaussian 03 [2] package. We used the B3LYP/6-31G(d) energy functional for all DFT calculations. Computational time for frequency calculations based on optimized geometries for molecule *a, b, c, d,* and *ethene* in endo or exo forms took approximately 283, 263, 464, 213, and 5 minutes on a 2 GHz G5 Xserve processor, respectively.

2.3 Results

Table 2.1 shows the ground state energies from electronic structure calculations as well as the zero point energy (ZPE) corrections of the candidate molecules generated from endo and exo forms of DCPD. Calculations of reaction energies depicted in Figure 2.2 using the thermodynamic expression below

$$\Delta H_R = H_{products} - H_{reac\tan ts} \qquad (2.1)$$

is shown in Table 2.2 and Table 2.3. For example to calculate the heat of reaction of ROMP (which essentially amounts to the ring strain energy) of norborene ring in exo-DCPD, we subtract the sum of the DFT calculated internal energy (after ZPE corrections) of reactants (exo-DCPD and ethene) from the internal energy of the products (exo molecule *b*). Therefore $H_{nb(exo)}$ = -12696+2137.097+10559.067 = -0.539 eV as shown in Table 2.2.

We define H_{nb}, H_{cp} and H_R as the energy of reaction of the norborene, cyclo-pentene and both rings opening via ROMP, respectively. These energies are attributable to ring strain energy release. It is to be noted that H_{nb} and H_{cp} are reaction energies when the other site on constitutive DCPD molecule is unreacted.

Ring strain energies of these bonds are primary indicators of reactivity to ROMP reactions along with secondary factors such as reaction site approachability that is hard to quantify. There is no available literature that accurately quantifies ring strain in DCPD molecules apart from general heuristic arguments that note a higher angular strain of angles in the vicinity of the norborene ring as compared to that of angles near the cyclo-pentene ring. To our knowledge these simulations are first quantitative results for DCPD ring strains. The heats of reaction, or equivalently ring strains energies, are in shown in Table 2.2 and Table 2.3 for exo-DCPD and endo DCPD respectively

2.4 Discussion

If we compare the heat of reaction of various sites or equivalently strain energy of those site by looking at values after ZPE corrections in Table 2.2 and Table 2.3, a number of interesting features emerge. We find that in endo-DCPD the cyclo-pentene double bond is always endothermic to a ROMP reaction, whereas in exo DCPD case the cyclopentene ring is exothermic when the norborene ring is reacted. This implies that endo-DCPD is unlikely react its cyclo-pentene bond and will form generally linear DCPD. On the other hand exo-DCPD can undergo ROMP reaction at the cyclo-pentene site, giving rise to cross-linking. The combined ring strain energy (H_R) for ROMP reaction on both sites in endo-DCPD is less than the same quantity for exo-DCPD. This explains experimental observations of the higher exothermicity of exo-DCPD as compared to the endo-DCPD. We can also say that the cyclo-pentene site in the exo-DCPD is not likely to react before the norborene site on the same DCPD molecule has reacted due to a positive heat of reaction as can be seen in Table 2.2 if it reacts first. This therefore gives us a heuristic on the design of our reaction algorithm in later chapters.

All of the discussion above hinges on our assumption that it is the enthalpy change that accounts for the differences in reactivity of various sites in exo and endo-

DCPD and there is little or no role of the entropy change of the reaction. To justify this conjecture consider the free energy of reactions that is given below

$$\Delta G = \Delta H - T\Delta S \tag{2.2}$$

We know that entropy change ΔS of any linking process as is the case with the ROMP of DCPD is always negative since it reduces the degrees of freedom available to the system. Therefore the only driver of the reaction process remains the enthalpy change.

We therefore come to a conclusion that the second ROMP reaction on any endo-DCPD monomer can only be driven by harnessing the heat of reaction of the first ROMP reaction or neighboring reactions in the vicinity of a putative second reaction site. We suggest that the cross-linking process of endo-DCPD via ROMP is energetically unfavorable and since even the entropy change is negative implies that the free energy change of the cross-linking reaction is positive and therefore thermodynamics states that it is impossible.

However it is to be noted that endo-DCPD has been observed to have cross-linking. One way to explain this discrepancy is that cross-linking in endo-DCPD is not due to the reaction of the second double bond via the ROMP but due to a different reaction mechanism as proposed by Davidson et al. [3]. They suggest that the cross-links in DCPD are due to a thermally induced olefin addition as is shown in Figure 2.3a. We posit that the actual reaction is as shown in Figure 2.3b. This reaction is commonly known as olefin addition. Note that the residual C=C double bond after olefin addition is unstable and short-lived, such strained double bonds easily undergo addition reactions with small molecules like water to form alcohol transforming the double bond in to a single bond. This hypothesis needs more investigation, which is encumbered by the fact that relaxed

C-C bonds are generally not active in common experimental techniques such as Raman or IR spectra.

It can be seen that in our proposed reaction scheme two C=C on adjacent cyclo-pentene rings are replaced with one C=C cross-linking bond and two C-C bonds where the two original C=C used to exist. This reaction is exothermic because the two C-C have a combined bond energy of 2×348 KJ/mol which is greater than the $C = C$ bond energy of 614 KJ/mol. This olefin addition reaction is thus thermodynamically plausible. It is however limited by high activation energy barriers that make it feasible only at high temperature. Mauldin et. al [4] propose that such high temperatures could locally arise due to ROMP reactions.

From the DFT calculated heat of reaction data we can predict that the exo-DCPD is more likely to cross-link using ROMP mechanism as compared to the endo-DCPD. Also exo-DCPD, due to its greater exothermicity, could drive the olefin addition mechanism shown in Figure 2.3b. In essence the thermodynamics of the ROMP reaction dictates that the endo-DCPD system is likely to evolve into linear chains where as exo-DCPD is likely to have more cross-links. This unique feature can then be used to design polymerization systems that can be tailored for specific applications and reaction. An initial solution rich in endo-DCPD and low in exo-DCPD will have more rubbery properties due to the formation of linear chains, whereas an initial solution rich in exo-DCPD will be highly cross-linked and will behave on full cure as a thermoset with high modulus. A recent work by Mauldin et al. [4] on blends of endo- and exo-DCPD to tailor the final network structures to self-healing materials is salient. Their experimental results on ROMP of DCPD measured fracture toughness. They observe that exo-DCPD reacts faster than endo-DCPD and if carefully controlled for proper catalyst dissolution results in exo-DCPD networks that have equal or higher fracture toughness than those formed by endo-DCPD.

2.5 Reaction Model to be Implemented in Molecular Simulations

Based on our preliminary survey of the DCPD ROMP reaction landscape we find a rich variety of possibilities and need to narrow down our investigations. We first need to understand the broad details that are relevant in creating network polymers from reactive processes. The key assumptions we make for further MD studies of the evolving network system of DCPD ROMP are as follows.

1. Cross-linking reaction of norborene or cyclo-pentene sites occurs via ROMP regardless of the state of reaction of the other reaction site on a given DCPD. We also ignore any contributions made by olefin addition mechanism discussed above. This is contrary to our DFT calculations and experimental work by [3] but at the time at which the majority of this work was undertaken the two-site ROMP reaction was the accepted physical model [56] for cross-linking.
2. The probability of ROMP reaction is the same for both sites and occurs due to a steric criterion i.e. the reactions on both sites are diffusion limited. We explore this assumption in our coarse grained simulations by assuming a different probability of reaction for the second reaction based on the DFT data presented above. However we relax this condition for our all-atomistic simulations.
3. We simulate the ROMP of DCPD that is likely formed by the action of first generation Grubb's catalyst on exo DCPD with the important caveat that we will

ignore cis and trans conformer selectivity of the first generation catalyst and allow both conformations to occur in the reaction with equal probability.

We will use the above assumptions primarily in our investigation in Chapter 4 where we simulate reaction on atomistic systems. In Chapter 3 we allow ourselves more flexibility since there we model the DCPD molecule as a bead and attach additional criteria to the reaction mechanism to suit the constraints imposed by coarse graining.

2.6 Tables

Table 2.1: Internal energies and zero point corrections of candidate molecules.

Molecule	$E_o(eV)$	$ZPE(eV)$	$E = E_o + ZPE$
$ethene$	-2138.491	1.394	-2137.097
$a(exo)$	10564.353	5.286	-10559.067
$a\ (endo)$	-10564.306	5.285	-10559.021
$b(exo)$	-12703.455	6.752	-12696.703
$b(endo)$	-12703.383	6.761	-12696.622
$c(exo)$	-12702.897	6.755	-12696.142
$c(endo)$	-12702.802	6.762	-12696.040
$d(exo)$	-14842.205	8.216	-14833.989
$d(endo)$	-14841.902	8.224	-14833.678

Each candidate molecule was first created using ad-hoc procedure detailed in text and equilibrated using DFT simulations to calculate internal energies. The internal energy here can be thought of as the heat of formation of these molecules

Table 2.2: Heat of reactions of ROMP on exo-DCPD system.

Reaction # Figure 2.2	**Significance:**	**Value (eV) (w/ ZPE)**	**Value (eV) (w ZPE)**
1 (H_{nb})	Norborene ring opening	-0.611	-0.539
2 (H_{cp})	Cyclo-pentene ring opening	-0.053	+0.022
3	Cyclo-pentene ring opening after 1	-0.259	-0.189
4	Norborene ring opening after 2	-0.817	-0.75
1+ 3 OR 2 + 4 (H_R)	Opening of both rings	-0.870	-0.728

The heat of reaction of each reaction mentioned in Figure 2.2 is calculated for exo-DCPD ROMP reaction using the internal energies of exo-derivatives listed in Table 2.1. An example is given in text. Note exo-DCPD combined heat of reaction (H_R) is more exothermic than the same for endo-DCPD. This quantitatively explains experimental observations.

Table 2.3: Heat of reaction of ROMP on endo-DCPD system.

Reaction # Figure 2.2	**Significance:**	**Value (eV) (w/ ZPE)**	**Value (eV) (w ZPE)**
1 (H_{nb})	Norborene ring opening	-0.586	-0.504
2 (H_{cp})	Cyclo-pentene ring opening	-0.050	+0.078
3	Cyclo-pentene ring opening after 1	-0.028	+0.041
4	Norborene ring opening after 2	-0.568	-0.541
1+ 3 OR 2 + 4 (H_R)	Opening of both rings	-0.614	-0.463

The heat of reaction of each reaction mentioned in Figure 2.2 is calculated for exo-DCPD ROMP reaction using the internal energies of exo-derivatives listed in Table 2.1. Note endo-DCPD cyclopentene is endothermic in reaction 2 and 3 in contrast to the same in exo-DCPD. This implies endo-DCPD cyclopentene ring is unlikely to undergo ROMP

2.7 Figures

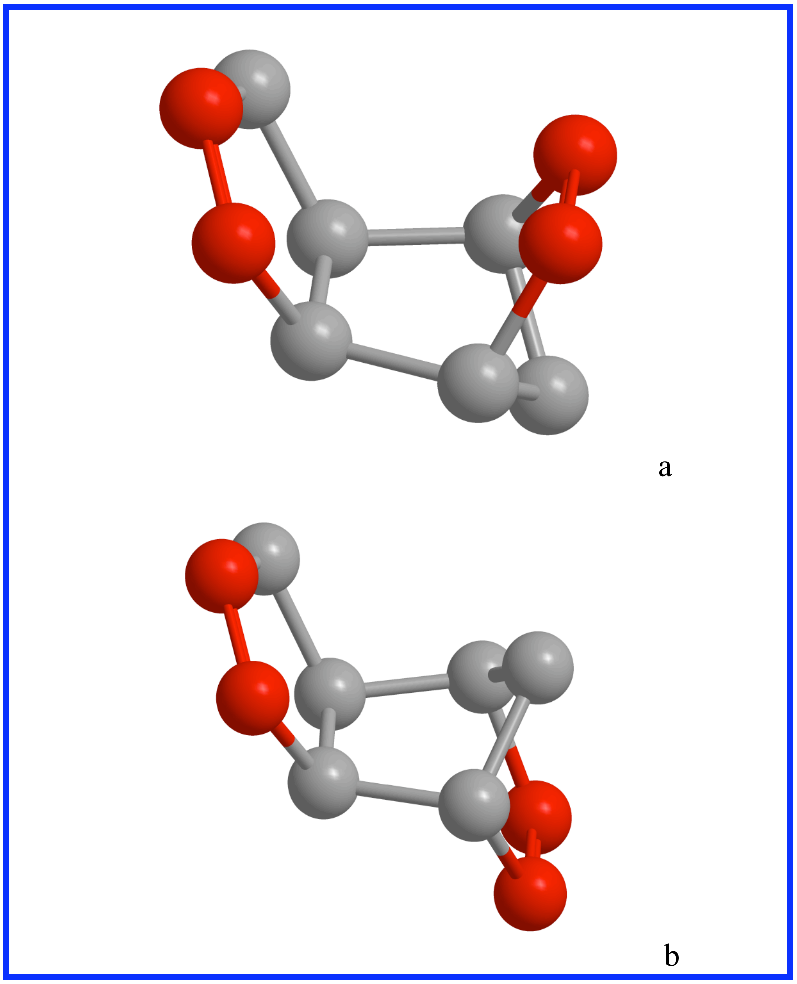

Figure 2.1: Molecular representation of a) endo-DCPD and b) exo-DCPD. In both figures double bonds represented by red atoms and bonds. Left side double bonds are the cyclo-pentene double bonds and double bonds to the right side of molecules are the norborene double bonds. These double bonds exhibit differing reactivity to ROMP reaction. These reactivity differences occur primarily due to differing ring strains and secondarily due to site accessibility.

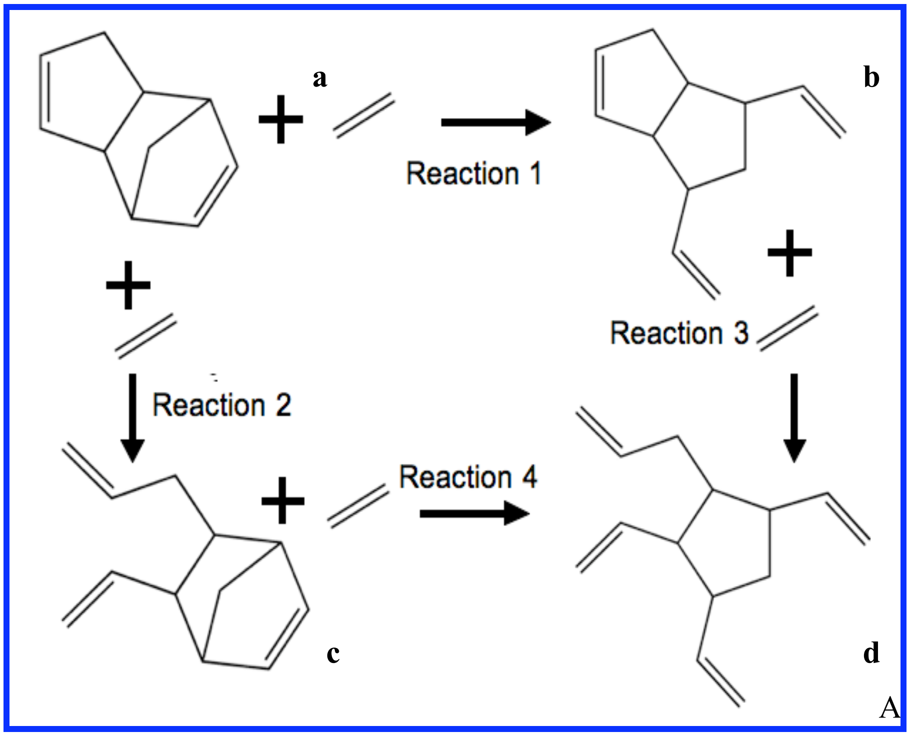

Figure 2.2: Reaction pathway for ROMP of DCPD with ethene. The reaction molecule are a) unreacted DCPD b) norborene after reaction with ethene c) cyclo-pentene after reaction with ethene d) both bonds after reaction with 2 ethenes

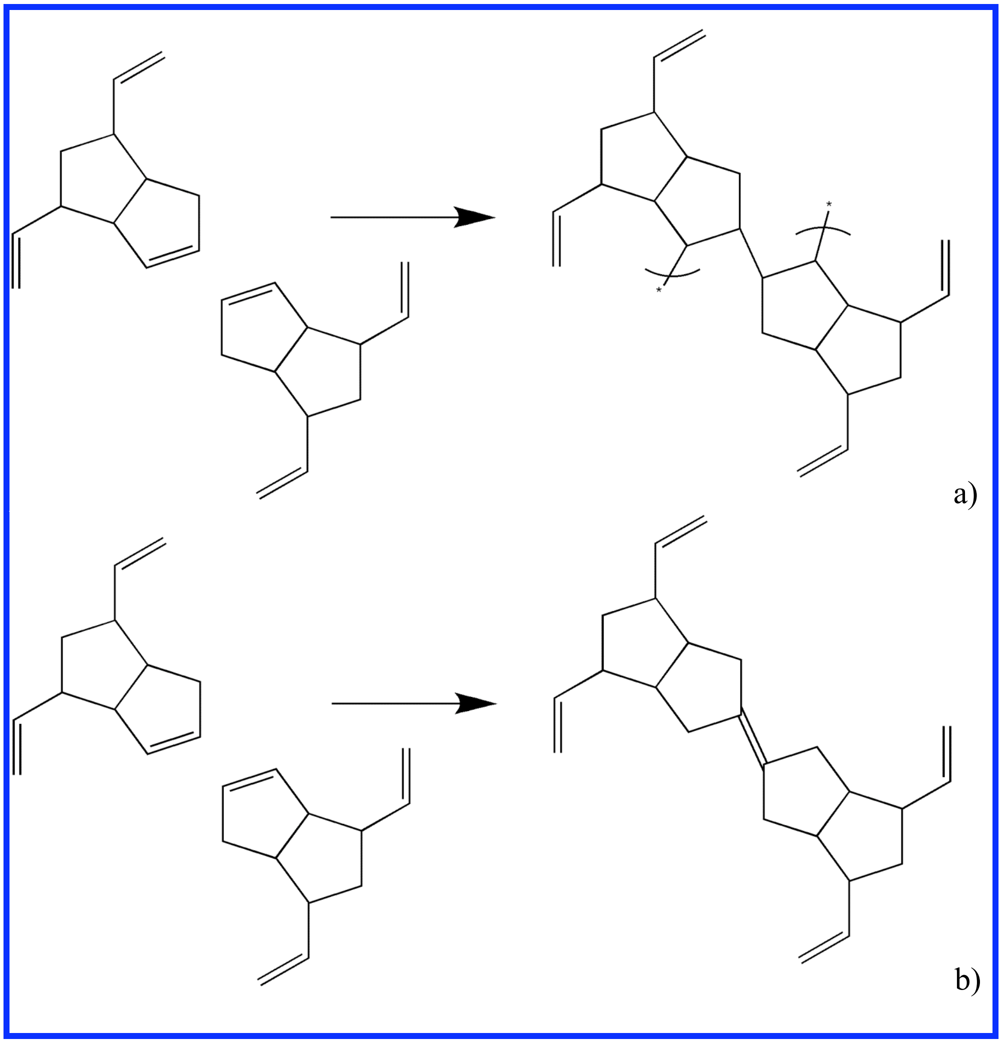

Figure 2.3: Alternative cross-linking mechanism by a) Davidson et al. [3] b) this work. The proposed double bond in b) is unstable due to connection of the central double bonded carbons to 3 other carbon atoms and therefore is short-lived. This double bond is likely to interact with small molecules such as water to form complex alcohols by an addition reaction (not shown). The resultant single bond after the addition reaction is IR and Raman inactive as suggested by DFT simulations not presented in this work.

2.8 References

1. Rule, J. D. & Moore, J. S. ROMP Reactivity of endo- and exo-Dicyclopentadiene. *Macromolecule* **35**, 7878-7882 (2002).

2. Frisch, M. J. et al. Gaussian 03 DFT code. *http://www.gaussian.com/citation_g03.htm*

3. Davidson, T. A., Wagener, K. B. & Priddy, D. B. Polymerization of Dicyclopentadiene: A Tale of Two Mechanisms. *Macromolecules* **29**, 786-788 (1996).

4. Mauldin, T. C., Rule, J. D., Sottos, N. R., White, S. R. & Moore, J. S. Self-healing kinetics and the stereoisomers of dicyclopentadiene. *Journal of The Royal Society Interface* **4**, 389-393 (2007).

5. Yeong-Show Yang, Eric Lafontaine, Bruno Mortaigne. NMR characterisation of dicyclopentadiene resins and polydicyclopentadienes. *Journal of Applied Polymer Science* **60**, 2419-2435 (1996).

6. Kessler, M., Larin, G. & Bernklau, N. Cure characterization and viscosity development of ring-opening metathesis polymerized resins. *Journal of Thermal Analysis and Calorimetry* **85**, 7-12 (2006).

Chapter 3
Coarse-Grained Simulations

3.1 Introduction

In this Chapter we further our understanding of the relationship between mechanical properties of a network structure and its topology. Our first goal is to assess whether the process by which a network forms, indeed creates unique structure and properties. We devised a coarse-grained (CG) simulation scheme mimicking the formation of networks from dicyclopentadiene (DCPD). The DCPD molecule is shown in Figure 3.1. The DCPD molecule undergoes a ring opening metathesis polymerization (ROMP) catalyzed by a ruthenium based Grubb's catalyst [1]. The reaction mechanisms for such a cross-linking process are shown in Figure 3.2. The highly cross-linked polymers formed by the ROMP reaction of DCPD monomers shares similar bonding characteristics with $Ge_xAs_ySe_{1-x-y}$ glasses [2]. The main difference being that they can only form bonds with 2 or 4 of their neighbors instead of 2, 3 and 4 neighbors as is the case with $Ge_xAs_ySe_{1-x-y}$ glasses. Another important difference is that ROMP is a catalyzed reaction and the sequence of network bonds marks the trail of the catalyst. Whereas in glasses bonds can break and form spontaneously at any moment while in the molten state, and the quench captures one particular bonding configuration.

ROMP of DCPD system is of enormous importance in applications such as autonomic self-healing of polymer composites [3] and it is not well studied insofar as the evolution of mechanical properties as a function of the degree of cure is concerned.

Multi-scale modeling efforts [4] for crack retardation as envisaged in self-healing materials require information about the kinetics of DCPD ROMP reactions to model the effects of the competition between the healing process and the fatigue crack propagation process in order to optimize the design of the self-healing material. Current investigations of ROMP reactions involving DCPD employ techniques such as ultrasonic spectroscopy [5], Raman spectroscopy [6,7], and differential scanning calorimetry (DSC) [8]. The key challenge in such techniques is the unambiguous interpretation of DCPD network formation. Post cure techniques such as x-ray diffraction pose special problems due to radiation damage during analysis, in addition DCPD networks being amorphous, do not lend themselves well to structural characterization using diffraction techniques.

In this Chapter we will address two critical issues in network generation: 1) does mechanical property depend on the mechanism of network formation and 2) what features does a CG simulation need to reproduce in order to accurately describe the real system. The former question will be answered in this Chapter and the latter will be answered in Chapter 5 by comparing the results of the mechanical properties predicted by CG simulations against our all atom simulations in Chapter 4.

3.2 Force Field Discussion

The 22 atoms of the DCPD monomer shown in Figure 3.1 are represented by a single bead in CG scheme. Each bead can have a maximum cross-link functionality of 4. Pair interactions between beads are modeled as a standard LJ (12-6) potential to model van der Waal's interactions between monomers as shown below.

$$U_{\alpha\beta}^{pair}(r < r_c) = 4\varepsilon\left[\left(\frac{\sigma}{r}\right)^{12} - \left(\frac{\sigma}{r}\right)^{6}\right] + C_p \tag{3.1}$$

Where $\varepsilon = 1.0$, $\sigma = 1.0$ and the cutoff distance $r_c = 2.5$. The constant C_P ensures the potential energy is 0 for $r > r_c$. The pair potential acts on all neighboring beads regardless of bonding. This is because the DCPD monomer center of mass does not change appreciably after bonding takes place and van der Waal forces by other atoms in a given DCPD monomer are still applicable to neighboring monomers. In the following sections the word beads will be synonymously used to refer to monomers in our coarse grained representation.

The bonded potential is a modified LJ potential given below that allows us to model bond breakage without force discontinuities at cutoff if needed.

$$U_{\alpha\beta}^{bond}(r < r_b) = 4\varepsilon_b \begin{bmatrix} \left(\frac{\sigma_b}{r}\right)^{12} - \left(\frac{\sigma_b}{r}\right)^{6} - 1.5\left(\frac{\sigma_b}{r}\right)^{8}\left(\frac{\sigma_b}{r_b}\right)^{4} \\ + 3\left(\frac{\sigma_b}{r}\right)^{2}\left(\frac{\sigma_b}{r_b}\right)^{4} \end{bmatrix} + C_b \qquad (3.2)$$

Here $\varepsilon_b = 200$, $\sigma_b = 1.1$, $r_b = 1.5$. The constant C_b ensures that the bond potential is 0 for ($r \geq r_b$). The distance r_b was chosen to ensure that bonds could not slip past each other without breaking during extension tests described in Section 3.4. We note that the density of fully cured DCPD is 1.05 g/cc and that of DCPD monomers is 1.03 g/cc. These real density observations in turn imply that there is very little contraction/expansion stress due to the ROMP reaction in DCPD. The key feature that controls the expansion or contraction stress accumulation, as reactions takes place is the parameter σ_b. In order to choose the best value of σ_b, sample runs of network generation were conducted on a small system (1000 beads) with different values $1.0 < \sigma_b < 1.5$. These simulations were compared amongst each other and the value of σ_b that caused the least contraction/expansion stress accumulation as the reaction processes introduce bonds into the system was chosen. This process resulted in σ_b = 1.1. This choice then ensures the simulation reproduces the small density changes upon polymerization observed experimentally.

In order to account for the energy gain associated with the unfolding of opened rings and the spreading of the newly created network bonds, we introduced angular constraints between adjacent pairs of bonds. Angular interaction potential given below were also integrated with an rRESPA time-step of 5×10^{-4} τ

$$E_{angle} = K(\theta - \theta_0)^2, \tag{3.3}$$

where $\theta_0 = 109.5^{\circ}$ and K = 30. The reaction coordinate or the degree of reaction in our systems is calculated as the average number of bonds per monomer denoted as Bonds/Monomer and it is a number between 0.0 and 4.0. Alternatively the reaction coordinate can also be understood as the fraction of bonds formed as compared to the maximum possible bonds. We call this fraction the degree of reaction α and it is a number between 0.0 and 1.0. In the sections and chapters hence we will refer to the degree of reaction (α) as our reaction coordinate.

3.3 ROMP and RANDOM Network Generation Methodology

In order to assess whether the process by which a polymer network is formed has an effect on its mechanical properties, we compare the behaviors of two systems: one in which the network has been created by simulating the ROMP process (henceforth referred to as ROMP network), and another one in which bonds between network nodes are assigned randomly (referred to as RANDOM network).

3.3.1 Network generation MD simulation details

All network generation MD simulations were carried out using a multiple time step second order sympletic integrator rRESPA[9,]. The pair interactions were integrated with a time step of 0.01τ and the bond interactions with a time step of 5×10^{-4} τ since the potential function for bonds has a sharp curvature near the energy minimum as compared to the pair potential. Simulations were performed on systems of 16000 beads each of mass m = 1.0 and at a reduced density of 0.75. These initial simulation ensembles were cooled from T = 1.9, to T = 0.9 using a Nose-Hoover NVT ensemble simulation using a temperature damping factor of 0.7τ in a total time of 20τ, where

$$\tau = \sqrt{\frac{m\sigma^2}{\varepsilon}} \tag{3.4}$$

This high temperature quench run ensures initial randomness of the simulation boxes before reactions for network formation begin. The initial condition of T = 0.9 and reduced density of 0.75 was carefully chosen so that the system lies in the molten phase of LJ 12-6 phase diagram and would not be affected by crystallization phenomena.

The ROMP network is formed as described by the catalytic process as shown in Figure 3.2. Essentially each catalyst can be thought of as an off-lattice non-self avoiding random walker. The trace of the walker’s path constitutes the network morphology. 2% of beads in any simulation (ROMP/RANDOM) are designated as catalytic beads that have maximum bond functionality of 3 bonds each. In ROMP reactions these beads serve as the starting points for network evolution but serve no functional purpose in RANDOM networks, apart from ensuring that the maximum possible number of bonds in any

(RANDOM or ROMP) simulation are the same. The coarse-grained ROMP and RANDOM networks were created using the procedure detailed below

3.3.2 Networks with no Angular Constraints

For the creation of RANDOM networks with no angular constraints the molecular dynamics simulation is interrupted every 1.0 τ to randomly choose 2% of beads. We call them initiator beads. Bond formation is attempted between the initiator beads and one of its randomly chosen neighbors. Bond formation is successful if the two beads occur at a distance r satisfying the criteria $0.9\ r_{cut} < r < 1.1\ r_{cut}$ and if both of the beads have less than their maximum bonding functionality of 4, where $r_{cut} = 1.2347$. In case the attempt fails no more reaction attempts are allowed on that particular initiator bead for the current reaction step. Additionally no bead is allowed to react twice in the same reaction step. If in case a bead is chosen twice or more times in the same reaction step then all but one randomly chosen reaction is disallowed.

On the other hand ROMP networks are created when bonds are formed between a catalytic bead (2% of the population) and a non-catalytic bead, satisfying the reaction criterion as described for the RANDOM case. In the case of ROMP networks a successful bond formation reaction leads to the non-catalytic bead converting to a catalytic bead and the previous catalyst bead reverts to a non-catalytic state, i.e., the catalyst always advances to the end of the chain. In the case of ROMP networks the catalytic beads are the initiator beads for reactions and are not chosen randomly once the simulation is started, they remain tethered to the evolving network initiating reactions.

In creating the ROMP networks there are 5 species in the reactions process. Adopting the nomenclature from the NMR community, DCPD with 0 bonds to neighbors termed as Q_0, monomers with 2 or 4 bonds termed Q_2 and Q_4 respectively. It becomes immediately obvious from the reaction equations below that the catalytic species have 1 bond and 3 bonds and therefore are termed Q_1 and Q_3 respectively

These species interact in 4 reaction processes as shown schematically as reaction (1) through reaction (4) below. The black bars indicate the number of bonds a particular species has, red beads are catalytic, blue are unreacted monomers, striped green beads are monomers that have reacted once, and solid green beads are monomers that have reacted twice. Each bead is also referred to as Q_x where x refers to the number of bonds attached to a bead.

$$Q_1 + Q_0 \xrightarrow{(1)} Q_2 + Q_1$$

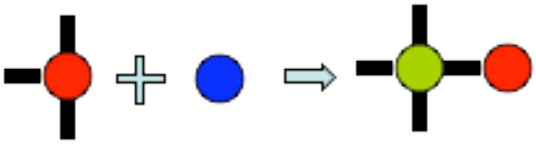

$$Q_3 + Q_0 \xrightarrow{(2)} Q_4 + Q_1$$

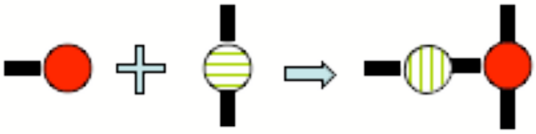

$$Q_1 + Q_2 \xrightarrow{(3)} Q_2 + Q_3$$

$$Q_3 + Q_2 \xrightarrow{(4)} Q_4 + Q_3$$

In ROMP simulations the reactions described by reaction (1) and (2) occur with unit probability if the proximity reaction criteria discussed above are met, reaction (3) occurs with a probability of 0.20 and reaction (4) occurs with a probability of 0.10. These reaction probabilities are so chosen since the norborene double bond of DCPD (bottom double bond in Figure 3.1 is more reactive than the cyclopentene double bond. Due to the lack of experimentally available kinetic models for these reaction processes in literature, we used ad hoc principles from our understanding of chemical reactivity of DCPD to assign reaction probabilities based on DFT calculations in Chapter 2. Reactions (1) and (2) are due to the attack on the norborene site of an un-reacted DCPD by a catalyst and were assigned a unit probability. Reaction (3) is the attack of a singly bonded catalyst (Q_1) on a cyclopentene site of DCPD and we assign a 0.2 probability to this reaction, reaction (4) is the attack of a 3 bonded catalyst (Q_3) on the cyclopentene site and we expected a lower reaction probability than reaction (3) due to steric reasons and therefore assigned it a value of 0.1.

All the network formation simulations were carried out under Nose-Hoover NVT ensemble with $T = 0.9$ at a reduced density of $\rho = 0.75$ with the temperature time damping factor of 0.7τ. Snapshots of these systems were saved at regular intervals during the progression of reactions for mechanical testing. Four independent samples of ROMP and RANDOM networks were created. Figure 3.3 shows a typical arrangement of a ROMP network at various degrees of reaction. Due to the random nature of the bond formation mechanism, creating simulation ensembles with exactly equal number of bonds at each degree of reaction was difficult and we therefore saved simulation snapshots within $\Delta\alpha = 0.1 \pm 0.004$ increments in α. Such differences in the degree of reaction do not significantly change behavior of networks.

ROMP networks with no angular constraints on 16000-bead systems were created in approximately two million time-steps using LAMMPS.[10,] These took 700 hours on both processors of a dual CPU Apple G5-Xserve node to achieve a maximum α of 0.85. Simulations of RANDOM networks with no angular constraint achieved a maximum α of 0.9 after 1.0 million time-steps in 500 hrs.

3.3.3 Networks with Angular Constraints

Networks with angular constraints are created using the same procedure as those without constraints, with some additional criteria. During the formation of the networks with angular constraints we ensure that the angle between a new bond and the last created old bond lies within $\pm 15^\circ$ of the angle θ_0 specified in eqn(3.3). This prevents excessive angular forces at the time of network formation from causing energetically unfavorable configurations to build up over long times. An addition of a bond in the system with angular constraints also results in the addition of an angular constraint between the 2 reacting beads and the previous beads they have reacted to if any. If the beads undergoing reaction had not previously reacted to any beads in previous reaction step then no angular constraint is added. In both ROMP and RANDOM cases angular constraints are attached to the angle between the newest bond and the bond that was created in previous reaction process

However, with these angular constraints we find that networks do not achieve as high degrees of reaction as without angular constraints, as seen by the maximum achieved degree of reaction in Figure 3.5b. Snapshots of these systems were saved at regular intervals in the progression of reactions for mechanical testing. Four independent samples of angularly constrained ROMP and RANDOM networks were created for mechanical testing, as is the case for networks without angular constraints.

In the simulation of a ROMP network with angular constraints we assigned unit probabilities to all reactions as mentioned in reaction 1 through 4 as noted above. This is justified since the angular constraints automatically restrict a large number of possible reactions and therefore implicitly change the reaction probabilities. We find that ROMP and RANDOM networks achieve a maximum degree of reaction of 0.7 and 0.85, respectively, after 5 million time-steps. These simulations required about 550 hours on 2 processors of the G5 Xserve cluster. The speciation, i.e., the distribution of Q_0, Q_1, Q_2, Q_3, and Q_4 species in networks with angular constraints is similar to that obtained from simulations without angular constraints as shown in Figure 3.4 c and d .

3.3.4 Reaction Kinetics.

A first order kinetic model effectively explains the reaction kinetics as is expected from the reaction model that is used to generate the networks. The rate equation for the concentration of the monomer species for both mechanisms is fit to the expression given by eqn(3.5) and the degree of reaction (α) is fit to the expression given by eqn(3.6)

$$[Q_0] = 0.98 \times \exp(-t/\tau_0) \qquad (3.5)$$

$$\alpha = 1 - \psi \exp(-t/\tau_1) - \zeta \exp(-t/\tau_2) \tag{3.6}$$

The results of the fit are shown in Table 3.1 and plotted along with data in Figure 3.5. The two exponential terms in the expression can be thought of as rate expressions of a fast first order reaction added to a rate expression of a second slower first order reaction. The fast reaction can be thought of as the initial conversion of norborene and cyclopentene double bonds via ROMP and the second reaction the subsequent slow-down of reactions due to cross-linking, lesser availability and lower diffusion of reactive species as the network gels disallowing free movement. From the plot the fit for ROMP networks is not good at large α. This is due to the fact that the ROMP network tethers the catalyst particles and therefore inhibits the encounters of catalyst and monomers with free reaction sites. RANDOM reactions do not place this constraint on their reactions and therefore the probability that reactions follow first order kinetics regardless of the state of the network.

These results are consistent with experimental studies in ROMP polymerization of DCPD[5] that also suggest first order reaction kinetics. It is interesting to note that both ROMP and RANDOM networks with angular constraints, along with the ROMP network without angular constraints, seem to have two distinct reaction time constants that differ considerably in magnitude as evidenced by τ_1 and τ_2. These widely different time constants explain network evolution behavior at initial times and at longer times. The larger time constant is a slowdown effect that occurs due to the unavailability of reactants after the initial reactions have consumed all non-reacted and partially reacted monomers in the vicinity of the catalyst. Thereafter, due to limited access, further network development slows in ROMP networks generated with and without angular constraints, as well as in RANDOM networks with angular constraints. The RANDOM network without angular constraints is unaffected since it has less rigid criteria to satisfy for reactions since we allow reactions on randomly chosen beads in the simulation with only the proximity constraint that is independent of diffusion of species.

The long-time network behavior of our reaction scheme is highly important as it allows the evolving network to relax into more stable configurations while the reaction progresses, and thereby reduces the probability of high-energy configurations developing. The ROMP network with angular constraints does not follow the first order kinetics proposed by eqn(3.5) for the monomer concentrations at high degrees of reaction, because after some time the catalyst beads that facilitate further bond formations are locally trapped into highly reacted networks with no avenues to access un-reacted sites. This catalyst sequestration by the network does not affect the RANDOM networks since the reaction sites are randomly chosen throughout the simulation box.

We therefore observe RANDOM networks reaching higher degrees of reaction than catalytically reacted ROMP networks. We believe this feature should hold true even in real systems and therefore especially significant to the design of self-healing systems. This is useful because higher α indicates better mechanical cohesion. The ramifications of the differences in the extent of reaction between catalytic and non-catalytic networks is discussed in Section 3.5

3.4 Calculation of Mechanical Properties

Figure 3.4a/b shows the speciation of a ROMP and a RANDOM network at different degrees of reaction (α) for networks with no angular constraints and Figures 3.4 c and d show the same for networks with angular constraints. We can see significant differences between the fractions of various species in the configurations these two systems. It is to be noted that the sum of the fractions of Q_1 and Q_3 species is the fraction of catalyst particles in the simulation. As is seen from Figure 3.4 the ROMP networks is made up of predominantly Q_2 and Q_4 nodes where as the RANDOM networks have significant amounts of Q_1, Q_2, Q_3 and Q_4 nodes at comparable α. The evolution of mechanical properties is dependent on the network morphology and we show that conventional theories of network percolation insufficiently explain differences in mechanical properties. In these network percolation theories the onset of rubber elasticity is not considered. This is mainly due to the fact that the mechanical properties are reported at absolute zero temperature where the rubbery elastic modulus is zero, a fact that is well known in classical polymer physics of rubbers, since modulus is directly proportional to absolute temperature. Secondly generating networks using lattices is not ideal since it imposes symmetry. On example of such a method is the bond dilution paradigm of network creation[2], where a perfect diamond cubic (DC) lattice is created and bonds deleted at random to create networks at different average coordination from 0 to 1. In this case 1 signifies a perfect lattice where each lattice bead is connected to 4 other beads in a DC lattice. Such symmetric networks are likely to respond to strain like crystals rather than as polymer rubbers. Therefore to show how topology matters, we test the mechanical properties of ROMP and RANDOM networks created by non lattice mechanisms in the next section and show significant differences in their behavior.

3.4.1 Toughness

As an initial investigation into network properties a large deformation uniaxial test is carried out before we probe the network for modulus properties at small strains in Section 3.4.2 and Section 3.4.3 where we measure the Young's modulus and Poisson's ratio respectively. In the uniaxial tension tests, the networks are uniformly extended in one direction at a constant strain rate. Observing the behavior of networks during this deformation provides valuable insight. We describe these uniaxial tests in the following and discuss the salient results and conclusions.

3.4.1.1 Networks with no Angular Constraints

An important mechanical property of materials is their toughness. One measure of toughness of solids can be calculated from the area under the stress strain curve until complete failure. In MD simulations this is difficult to measure since the area under the curve is strongly strain rate dependent due to hydrodynamic and viscous effects. At the large strain rates that MD simulation probes it is hard to directly correlate the MD calculated toughness with real values. Nevertheless we report the results of systems of non-angular constrained networks without angular constraints strained uniformly to a maximum of 100%. This is possible since our bond potentials are designed to smoothly tail off without discontinuities in force or energy, enabling bond breaking.

The toughness of each system is measured by the following procedure. The simulation snapshots obtained from the network formation process are allowed to relax for 100 τ using a Nose-Hoover barostat (NPT) at (T = 0.9) with a temperature damping factor of 1.0 τ and the stresses in the x and z directions are controlled concurrently to a pressure of 0.02 (ε/σ^3) with a pressure damping factor of 50 τ, the y dimension is held constant. These relaxed network configurations are then extended in the y dimension at a constant strain rate of $10^{-3}\ \tau^{-1}$ for 1000 τ until a strain is of 100% is reached. As a result of holding the y dimension static the initial stress in the y direction (σ_{yy}) is not fully relaxed and contains some residual stress especially at high degrees of reaction.

It is important to note the behavior of the networks below 20% extension since we use that limit in our Young's modulus and Poisson's ratio calculation in Section 3.4.2.1 and Section 3.4.3 respectively.

Figure 3.6 and shows typical behavior of a ROMP network at 3 different degrees of reaction and Figure 3.7 shows the same for a RANDOM network at 3 different degrees of reaction. We report toughness by integrating the stresses σ_{yy} with strain until 100% extension. Figure 3.8 shows the toughness of both ROMP and RAND networks.

3.4.1.2 Network with Angular Constraints

A toughness test is not possible with the angularly constrained networks since a bond break during extension will result in the physically unrealistic state where the angular constraints still remain in the system. Even though we do not report the toughness of network with angular constraints, we performed a similar uniaxial stress test as above but limited to 20% strain to ensure that no bonds are broken instead of 100% extension as is the case with toughness test of networks with no angular constraints. Figure 3.9 and Figure 3.10 shows the network behavior of ROMP and RANDOM networks with angular constraints networks to applied strain in our 20% extension uniaxial test described above.

The most important feature we see from these extension experiments is the behavior of the internal energy of the networks up to 5% strain which is the limit used for our Young's modulus and Poisson's ratio calculation in Section 3.4.2.2 and Section 3.4.3 respectively.

3.4.2 Young's Modulus

3.4.2.1 Networks without Angular Constraints

The Young's modulus of each system is measured by subjecting the networks to a uniaxial tension test using the following 3-step process. Step 1: The simulation snapshots at different degrees of reaction obtained from the network formation simulations are allowed to relax for 1000 τ using a Nose-Hoover barostat (NPT) at (T = 0.9) with a temperature-damping factor of 1.0 τ. The x and z dimensions are coupled to control the pressure $(\sigma_{xx}+\sigma_{zz})/2$ to $0.02\cdot(\varepsilon/\sigma^3)$, with a pressure-damping factor of 50 τ, the y dimension is held constant. Step 2: These relaxed network configurations are then extended in the y dimension at a constant strain rate of $10^{-3}(1/\tau^{-})$ for 200 τ until the strain reaches 20%. Step 3: This strained simulation box is relaxed for 1000 τ using the same NPT conditions as in step 1. Average stresses are obtained by averaging σ_{yy} over the last 200τ of the 1000τ relaxation. The Young's modulus is calculated by comparing the average stresses, of the strained $<\sigma_{yy}>_{ext}$ and unstrained $<\sigma_{yy}>_0$ configurations

$$E = \frac{\Delta\sigma_{yy}}{\Delta\varepsilon_y} \tag{3.7}$$

which can be written in our case as.

$$E = \frac{\langle\sigma_{yy}\rangle_{ext} - \langle\sigma_{yy}\rangle_0}{0.2} \tag{3.8}$$

We also calculated the Young's modulus for these systems at 1% strain by modifying step 2 keeping all other steps the same as described above. The results of the

Young's modulus for the ROMP and RANDOM networks without angular constraints at 1% strain and 20% strain are shown in Figure 3.11 a and b respectively. As can be seen, at low strain (1%) is difficult to discern differences in the Young's modulus for ROMP and RANDOM networks, but they become apparent at high strains such as 20%. Equilibrium methods such as Green-Kubo formulations can also be used for the same measurement and yields a shear viscosity measure. However, we chose not to use this method based on the poor signal to noise ratio it yields[11,12]. Furthermore, the tensile test approach also provides an easy measurement of the Poisson's ratio from the simulation box dimensions.

We note that in all our simulations none of networks have more than 10 monomers in a linear chain and we therefore expected these networks to behave more like glasses, since the chain lengths of our systems are less than that in the work of Barsky et al. and Kremer et al.[13,14]. In their work the entanglement length is estimated to be $N_e \approx 35$, and since our mean length between cross-links is lower than the entanglement length, we expect mechanical effects of entanglements to be insignificant.

We see from Figure 3.11b that for both ROMP and RANDOM systems $\alpha < 0.6$ behave plastically. This plastic or flow like behavior is further supported by data from our large strain uniaxial experiments in Section 3.4.1. In these experiments we find that both ROMP and RANDOM networks without angular constraints do not offer resistance to strain until large extensions particularly at low degrees of reaction. These results can be seen in Figure 3.6a and Figure 3.7a and is consistent with network rigidity percolation theories proposed by Thorpe et al.[15] where the rigidity percolation threshold is approximately at $\alpha = 0.6$ for RANDOM networks.

3.4.2.2 Networks with Angular Constraints

Tensile tests for ROMP and RANDOM networks with angular constraints were similarly achieved with final extension of 5%, while for networks without angular constraints the final extension was 20% as mentioned in Section 3.4.2.1. The 5% strain limit was chosen after examination of the network behavior with angular constraints to a maximum extension of 20% as discussed previously in Section 3.4.1.2

We note that none of the networks with angular constraints experienced bond breaking during the uniaxial mechanical test even up to an extension of 20%. The Young's modulus was calculated using the same three-step process that was used in Section 3.4.2.1 with the relaxation time of 200τ instead of the 1000τ that was used in networks in no angular constraints. Secondly the average stress required for the Young's modulus calculation was obtained from the last 50τ of the relaxation period of 200τ. The reason for choosing a shorter relaxation time in angular constraint systems was because the introduction of angular constraints resulted in faster relaxation times of the systems. Figure 3.12 shows the Young's modulus obtained for RANDOM and ROMP networks with angular constraints.

3.4.3 Poisson's Ratio

Poisson's ratio was calculated from the Young's modulus simulations at 20% strain for networks with no angular constraints and from 5% strain experiments in the networks with angular constraints. The Poisson's ratio is given by

$$\nu = -\frac{\Delta\varepsilon_T}{\Delta\varepsilon_y} \tag{3.9}$$

where the strain ε_y can be related to the simulation box extension ratio λ_y as below.

$$\varepsilon_i = \lambda_i - 1 \qquad (3.10)$$

Where the subscript *i* refers to the coordinate direction *x, y,* or *z*. Using eqn(3.10), now eqn(3.9) can reframed in our case as the following equation

$$\upsilon = -\frac{\left(\lambda_T - 1\right)}{\left(\lambda_y - 1\right)}, \qquad (3.11)$$

where $\lambda_T = \frac{(L_x^{ext} + L_z^{ext})}{(L_x^0 + L_z^0)}$ and $\lambda_y - 1 = 0.2$ and 0.05 for networks without angular and with angular constraints, respectively. L_x^{ext} and L_z^{ext} are the equilibrium values of the simulation box after strain in *y* direction. L_x^0 and L_z^0 are the equilibrium values in the no-strained state

The Poisson's ratios for networks without angular and with angular constraints are shown in Figure 3.13 and Figure 3.14, respectively. As we can see the behavior of the Poisson's ratio and Young's modulus are inversely related. Networks without angular constraints of the ROMP and RANDOM systems closely follow the percolation threshold phenomena described by Thorpe et al[15]. However the imposition of angular constraints in the bonding between network nodes shifts the percolation threshold to a lower degree of reaction.

3.4.4 Bulk Modulus

The bulk modulus of all networks ROMP/ RANDOM with and without angular constraints is calculated by using the following procedure. We first equilibrate each simulation box for 200 τ using a Nose-Hoover barostat (NPT) at (T = 0.9) with a temperature damping factor of 1.0 τ. All the dimensions of the box are coupled to control the hydrodynamic pressure to $0.02(\varepsilon/\sigma^3)$ with a pressure damping factor of 5.0 τ. After the initial equilibration the box is then compressed isotropically by ±0.5% in each dimension thereby changing the volume and then relaxed for 200 τ for both the extension and compression runs. The hydrodynamic pressure is calculated as the average of the last 50 τ of each of the compression, extension and initial relaxation. The bulk modulus is calculated as

$$K = -V\frac{dP}{dV} \tag{3.12}$$

eqn(3.12) can be reframed as shown below.

$$K = -\frac{P^+ - P^-}{\left(V^+ - V^-\right)/\left(\left(V^+ + V^-\right)/2\right)}, \tag{3.13}$$

where P^+ is the average hydrostatic pressure after expansion from equilibrium volume (V^+) and P^- is the pressure after compression from equilibrium volume (V^-).

The results of the bulk modulus calculations for networks without angular constraints are shown in Figure 3.15 and for networks with angular constraints are shown in Figure 3.16. The values of the bulk modulus along with the values of the Poisson's ratio and the Young's modulus can be used to calculate other elastic modulus values using standard transformations.

3.5 Results and Discussion

The behavior of Young's modulus in Figure 3.11, Figure 3.12 and Poisson's ratio in Figure 3.13, Figure 3.14 as a function of the degree of reaction is relevant. In particular we note from the Poisson's ratio behavior of all networks (with and without angular constraints, for ROMP/RAND networks) shown in Figure 3.13 and Figure 3.14 that the Poisson's ratio show two linear regions with differing slopes. The degree of reaction where these overlap or change over appears to be the point at which the network response to deformation switches from a predominantly entropic mode to a predominantly enthalpic mode. This is well supported by our uniaxial deformation results shown in Figure 3.6 and Figure 3.7 for networks with no angular constraints and in Figure 3.9 and Figure 3.10.

We first consider networks without angular constraints. Figure 3.6 shows salient network properties for ROMP networks with no angular constraints. We can see from the stress response that at a degree of reaction $\alpha = 0.4$ there is no restoring stress σ_{yy} at any strain. This implies there is no network in the simulation box that can resist the flow and the system therefore behaves as a fluid. We could have expected to see a viscous response to this rather fast deformation however the high temperature (T = 0.9) ensures a low viscosity and practically zero viscous response. A similar behavior is seen for RANDOM networks in Figure 3.7 at similar degree of reaction at $\alpha = 0.42$. At a slightly higher degree of reaction at $\alpha = 0.6$ there is a definite stress response, curiously however the internal energy seen by pair interaction energy and the total potential energy shows little or no change at lower strains and only seems to increase at large strains approaching almost 100%. The features seen in ROMP networks are mirrored by the response of RANDOM networks at similar degrees of reaction as can be seen in the curves for $\alpha = 0.62$ in Figure 3.7. At high α such as that shown by curves at $\alpha = 0.9$ in Figure 3.6 and Figure 3.7 we see that the stress response is accompanied by a change in internal energy and density.

Similar phenomena can be observed in networks with angular constraints. In Figure 3.9 we show again at low degrees of reaction such as seen by the curves of $\alpha = 0.20$ for ROMP networks there is no stress response apart from barostat oscillations. The same behavior can be seen in RANDOM networks at $\alpha = 0.15$ in Figure 3.10. However at $\alpha = 0.4$, shown in Figure 3.9 for ROMP networks, we see the characteristic stress response without tangible internal energy or density changes. Interestingly RANDOM networks with angular constraints seem to show such a behavior above a different threshold value of α than ROMP networks. We show an example of stress response with no density or internal energy response to deformation for RANDOM networks at $\alpha = 0.5$ in Figure 3.10. This is a departure of from the behavior of networks without angular constraints where both ROMP and RANDOM networks seem to have the same threshold at which such a response is seen. At still higher degree of reaction things are a little more complicated. Our simulation algorithm for generating networks with angular constraints is unable to create stress free networks as can be seen by non monotonic nature of the equilibrium total energy in Figure 3.9d and Figure 3.10d with the increase of α. We expect a network at a higher degree of reaction to have a lower potential energy. However this becomes increasingly difficult as addition of angular constraints to newly added bonds creates angles at non-equilibrium values. In spite of our efforts as described in the generation of networks with angular constraints to mitigate formation of non-equilibrium angles, they could not be avoided as we increased the degree of reaction. These non-equilibrium angles are energetically penalized by the stiff angular constraint term. For ROMP networks we find at an $\alpha = 0.685$ as shown in Figure 3.9 the stress response is accompanied by decrease in density along with an increase in pair energy as is expected. However total energy decreases contrary to expectations as can be seen in Figure 3.9d. This is because the deformation process relaxes the angles that are not at equilibrium and thereby reducing the internal energy. The same increase in total energy phenomena with deformation can be seen in RANDOM networks in the curves at $\alpha = 0.8$ for RANDOM networks in Figure 3.10d.

There are interesting implications of these observations. If the deformation response is entropic then interaction potentials have no effect on elastic properties, whereas if the response is enthalpic then the pair, bond and other backbone interactions become important. An internal energy change with concurrent density change due to deformation is indicative of enthalpic response. Absence of internal energy change or density change to applied strain indicates entropic response.

Glasses that deform in strain bands do so in a non-affine (inhomogeneous) manner where a certain fraction of atoms in the network deform more than the rest of the matrix. This observation can be further nuanced for polymeric materials where this non-affine deformation can be further subdivided into a entropic or enthalpic response. Cross-linked polymers initially transition from a viscous liquid state to a rubbery state where Poisson's ratio ~ 0.5 and then as the number of cross-links increases, the rubbery regions in the matrix become more and more rigid and finally form glassy matrix that show an internal energy change to deformation along with a Poisson's ratio less than 0.5. An elastic deformation can be expected to yield a change in internal energy as shown below.

$$-\Delta \mathrm{E}_{deform} = \int_0^{\varepsilon_x} \frac{\sigma_{xx} d\varepsilon_x}{\rho_N} + \int_0^{\varepsilon_y} \frac{\sigma_{yy} d\varepsilon_y}{\rho_N} + \int_0^{\varepsilon_z} \frac{\sigma_{zz} d\varepsilon_z}{\rho_N} \qquad (3.14)$$

We can arrive at an approximate value of the potential energy change with deformation if we assume that 1) the stress σ_{yy} is a linear function of ε_y 2) stress σ_{xx} and

σ_{zz} is maintained at 0.02 by our barostat and 3) neglect number density (ρ_N) changes during deformation. We can then rewrite eqn(3.14) as

$$\Delta \mathrm{E}_{deform} = -\frac{(\sigma^{o}_{xx} + \sigma^{o}_{zz})\varepsilon_t + (\sigma^{o}_{yy} + \sigma^{f}_{yy})\varepsilon_y /2}{\rho_N} \tag{3.15}$$

Where $\varepsilon_y = 5\%$ is the applied maximum y strain, ε_t is the resultant transverse strain. σ_x^o σ_y^o σ_z^o is the initial stress in x y and z direction respectively and σ_y^f is the final y stress after strain. For example in our Young's modulus tests if we apply eqn(3.15) for networks where $\alpha_Y<\alpha<\alpha_P$ and observe the time evolution of stress (σ_{yy}), number density and internal energy before and after deformation some interesting features emerge. We show these plots in Figure 3.18 for a ROMP network with angular constraints at $\alpha = 0.35$. For this network the calculated $\Delta E_{deform} \sim 0.002\varepsilon$ (using $\sigma_y^f = -0.1$ and $\rho_N = 0.75$ from Figure 3.18) is difficult to discern from the thermal noise. However the change in density upon deformation is negligible. This observation can be explained in two ways a) the deformation response is viscous or b) it is entropic in nature. In both cases the Poisson's ratio is close to incompressible liquid value of 0.5. We show in Figure 3.19 for a candidate ROMP network with angular constraints ($\alpha = 0.40$) recovery to initial configuration after release from a strained state. This supports an entropic restoration argument, whereas a viscous liquid would retain its final strained state.

The entropic argument can also be intuitively understood from the realization that a predominantly entropic response necessarily means that the average separation of beads or atoms along with bond lengths and angles and other constraints cannot change significantly upon deformation, since such a change would be reflected in both density and internal energy. However the internal energy change is more difficult to measure than a density change.

Based in this we posit two thresholds that are of relevance in explaining the behavior of any network. 1) Threshold at which the Young's modulus changes slope (α_Y). 2) Threshold at which the Poisson's ratio changes slope. (α_P) In general these two thresholds differ with the threshold for the Poisson's ratio occurring at higher degrees of reaction than the Young's modulus threshold for the same system. These thresholds are tabulated in Table 3.2 based on observations of the Young's modulus behavior in Figure 3.11 and Figure 3.13 and Poisson's ratio behavior in Figure 3.12 and Figure 3.14. Based on these thresholds we can classify a network into one of 3 regions depending on its degree of reaction α. In region 1) for $\alpha < \alpha_Y$ the networks have no elastic restoring capacity and behave as fluids with negligible Young's modulus specially for small deformations. In region 2) for $\alpha_Y<\alpha<\alpha_P$ the network elastic response is entropic and there is very little change in internal energy or in the density of the system during deformation. This region can be thought of as a rubbery elastic region since the Poisson's ratio is ~0.5. In region 3) for $\alpha>\alpha_P$ the response is enthalpic. Region 1 is where fluid mechanical theories apply, as the response is viscous, in region 2 polymer theories explain observed phenomena and the networks behave as rubbers, and in region 3 deformations cause change in internal energy and glass theory explanations hold.

Our results for the Bulk modulus in Figure 3.15 and Figure 3.16 are shown for completeness sake and together with our results for Young's modulus and Poisson's ratio allow us to calculate any other modulus using standard transformations for comparison with experimental results should they become available in the future.

We show that the network morphology differences between ROMP and RANDOM network, as evidenced by the distribution of species with different number of bonds in Figure 3.4, plays a significant role in the mechanical properties of networks. We observe that the ROMP network forms a stronger network than the RANDOM system at the same degree of reaction after rigidity percolation. This can be attributed to the larger fraction of over-constrained quadruple-bonded monomers, Q_4, in ROMP systems whereas in the RANDOM system the fraction of quadruple-bonded monomers Q_4 is smaller, as can be seen in Figure 3.4. However according to polymer theories the Young's modulus behavior is correlated with the fraction of cross-linked species (Q_3+Q_4). This network characteristic among others will be examined in Chapter 6 where we characterize the networks generated using graph theory concepts and correlate these characteristics with Young's modulus behavior.

We also note that RANDOM systems go farther towards complete conversion as compared to ROMP networks since they do not need a tethered catalyst to facilitate a reaction, as in the case of the ROMP network This is a useful design heuristic that can enable designers of self-healing materials to tailor healing systems to get better mechanical properties. Recently self-healing materials have used a RANDOM reaction mechanism using two-component epoxies [16] instead of a catalytic system such as ROMP of DCPD. We believe that the RANDOM reaction processes of epoxy cross-linked networks could potentially offer superior performance as compared to a ROMP of DCPD reaction process. However there are other factors such as healing reservoir fraction in the matrix, density mismatches after reaction, and mixing efficiency that are critical to the self-healing process. We cannot predict these effects with our current simulations but under ideal conditions of complete mixing, equal reservoir volumes per healing effect needed, and further assuming that the healing process does not create internal stresses due to density mismatches the RANDOM reaction process though less mechanically strong at smaller degrees of reaction, reaches a given degree of reaction faster than a catalyst driven process and ultimately reaches a higher degree of reaction. All these factors lead us to conclude that a RANDOM reaction system would better serve a self-healing material.

Based on our observations of these polymer networks we believe that the evolving network transitions from a fluid state to a rubber composite state, where rigid sections networks are held together by predominantly rubbery section of the matrix. As the reaction continues, the rubbery portions coalesce leaving a highly cross-linked material that behave in a non-affine manner to deformation albeit exhibiting an enthalpic response.

Finally though we expected significantly different toughness values between ROMP and RANDOM networks (Figure 3.8) we find that results of the simulations do not support our hypothesis. This is an area that needs further study since toughness is strain rate dependent. We show in Chapter 6 expected toughness behavior based on the energy required to cleave the network using graph theory ideas.

3.6 Methodology for Converting LJ Units to Real Units

In Chapter 5 comparison of coarse-grained and atomistic simulation is shown and therefore transformations of LJ units to real units is essential. The σ parameter represent the size of the molecule and can be obtained after mapping the pair correlation functions

(PCF) of the coarse-grained LJ system onto the all-atomistic DCPD center of mass PCF, as shown in Figure 3.17.

The energy unit can be obtained by equating the heat of vaporization of an LJ liquid to that of the real DCPD system. The heat of vaporization of a LJ liquid was obtained by the application of the Clausius-Clapeyron equation as shown below to the LJ vapor liquid equilibrium (VLE) curves obtained from literature [17].

$$\frac{\Delta H_{vap}}{R}\left[\frac{1}{T_1}-\frac{1}{T_2}\right]=\ln\left(\frac{P_2}{P_1}\right) \tag{3.16}$$

From this the heat of vaporization for LJ (12-6) liquids is calculated as below

$$\Delta H_{vap}\approx 6.774\varepsilon \tag{3.17}$$

Comparing the LJ value of the heat of vaporization to real DCPD ΔH_{vap} = 50 KJ/mol[18], we get a value for the energy term ε = 738 J/mol

For the distance term, one method of calculating the σ is apparent in Figure 3.17, a second limit for the σ using real density of DCPD at 300K : 1.05 g/cm^3, and using eqn(3.18) gives a value of 5.37Å. The value of 5.85 Å is obtained by comparing PCFs of atomistic and coarse grained systems is a direct consequence of the lower simulated density of the atomistic system from Chapter 4 due to the presence of a small fraction of catalyst molecules.

$$\rho_{LJ}=\frac{N_A\rho_{real}}{M_{DCPD}}\left(\frac{\sigma_{LJ}}{\sigma_{real}}\right)^3 \tag{3.18}$$

$$P_{LJ}\frac{\sigma_{LJ}^3}{\varepsilon_{LJ}}=P_{real}\frac{\sigma_{real}^3}{\varepsilon_{real}} \tag{3.19}$$

From eqn(3.18) and (3.17) and experimentally obtained data give us σ_{real}=5.37Å, ε_{real}=738 J/mol respectively. Substitution of the scale factors for energy and distance in eqn(3.19) then gives us a pressure/stress conversion factor of 78 MPa. Assuming the value of σ_{real} = 5.85Å will give us a pressure conversion factor of 60 MPa. We therefore make an ad-hoc choice of 71 MPa for our pressure conversion factor.

It is to be noted that the PCFs do not fully match up because of the selection of the operating temperature and density of the LJ system. A LJ (T = 0.9) implies a real temperature of ~ 798K. However it is to be noted that the parameters of the LJ system were carefully chosen so as to prevent local crystallization during the network formation stage necessitating the choice of the high temperature. Crystallization of the LJ particles manifests itself when the same simulations were conducted at (T = 0.35) corresponding to room temperature.

These conversion factors are only valid for entropic deformations i.e. until a degree of reaction less the Poisson's threshold (α_P) since we neglect the contribution of bond deformations in these calculations. Accounting for bond deformation is complicated by the fact that in real systems generally a change in distance between two bonded monomer units is a complex interaction of angle deformation, dihedral deformation along with bond deformation. Our choice of the bond energy interaction parameter and angle interaction parameters in our simulations that envelops all these effects may be an extreme simplification however is justified by the observed entropic response. It is therefore instructive to understanding elastic response differences arising solely from topological changes in network structure.

As a result in subsequent Chapters all LJ pressures will be converted to real units using a pressure conversion factor of 71 MPa if the response is primarily entropic and choose a conversion factor of 142 MPa if there is enthalpic or internal energy changes on deformation. The choice of the conversion factor does not change the characteristics of the percolation phenomena we observe.

3.7 Synopsis

In practical terms cure of network polymers is a challenging area that involves explanation of various phenomena ranging from fluid mechanics to rubbery elasticity and glass theory concepts such as rigidity percolation. Any theory that attempts to realize real world behavior of such systems in-silico is constrained by time dependant phenomena and system size. In this Chapter we have shown some ideas that help classify the behavior of networks according to the degree of reaction.

There also is the question on how to extrapolate coarse-grained simulation results obtained to real values. We show a simple procedure for these transformations in Section 3.6. We will use this scaling factor to compare CG results with all atomistic modulus results from Chapter 4 in Chapter 5.

In conclusion this Chapter provides a coarse-grained framework for exploring highly cross-linked networks for their mechanical properties. We can explore elastic phenomena and along with failure due to the specially developed bonding interactions that allow bonds to break smoothly unlike other potentials such as harmonic bonds.

3.8 Tables

Table 3.1: Kinetic parameters fit values for eqn(3.5) and eqn(3.6) for coarse grained networks with angular constraints and without angular constraints

Type	τ_0	τ_1	τ_2	ψ	ζ
ROMP (no angles)	709(5.1)	1061.8(42)	13370(1378)	0.67	0.31
RAND (no angles)	325(2.3)	1078.7(16)	NA	1.0	NA
ROMP (with angles)	2870(107)	3155.2(64)	153660(11605)	0.58	0.41
RAND (with angles)	780(14)	2936.8(202)	31745(6281)	0.68	0.30

RANDOM networks with no angular constrains do not exhibit a second time constant in the fit. This points to the fact that the reaction is unaffected by network formation. All other network forming systems are in some way affected by the evolving network.

Table 3.2 Degree of reaction thresholds for Young's modulus and Poisson's ratio for various networks.

System	α_Y	α_P
ROMP(no angles)	0.4 (at 20% strain) or 0.8 (at 1% strain)	0.8(at 20% strain)
RANDOM (no angles)	0.4(at 20% strain) or 0.8 (at 1%s train)	0.8 (at 20% strain)
ROMP (with angles)	0.3	0.4
RANDOM (with angles)	0.4	0.55

Simulated networks behave as 1) fluids $\alpha < \alpha_Y$ and 2) as rubbers $\alpha_Y < \alpha < \alpha_p$ and finally as 3) glassy solids $\alpha > \alpha_p$. We find the introduction of angular constraints changes the threshold values α_Y and α_p significantly. It is not known experimentally if any real polymer network formers reach the Poisson's threshold α_p. This is an unanswered question and needs further experimental investigation. In case 2) elastic properties are entropic in origin, in case 3) the elastic properties are enthalpic in origin, and involve change in internal energy in response to deformation.

3.9 Figures

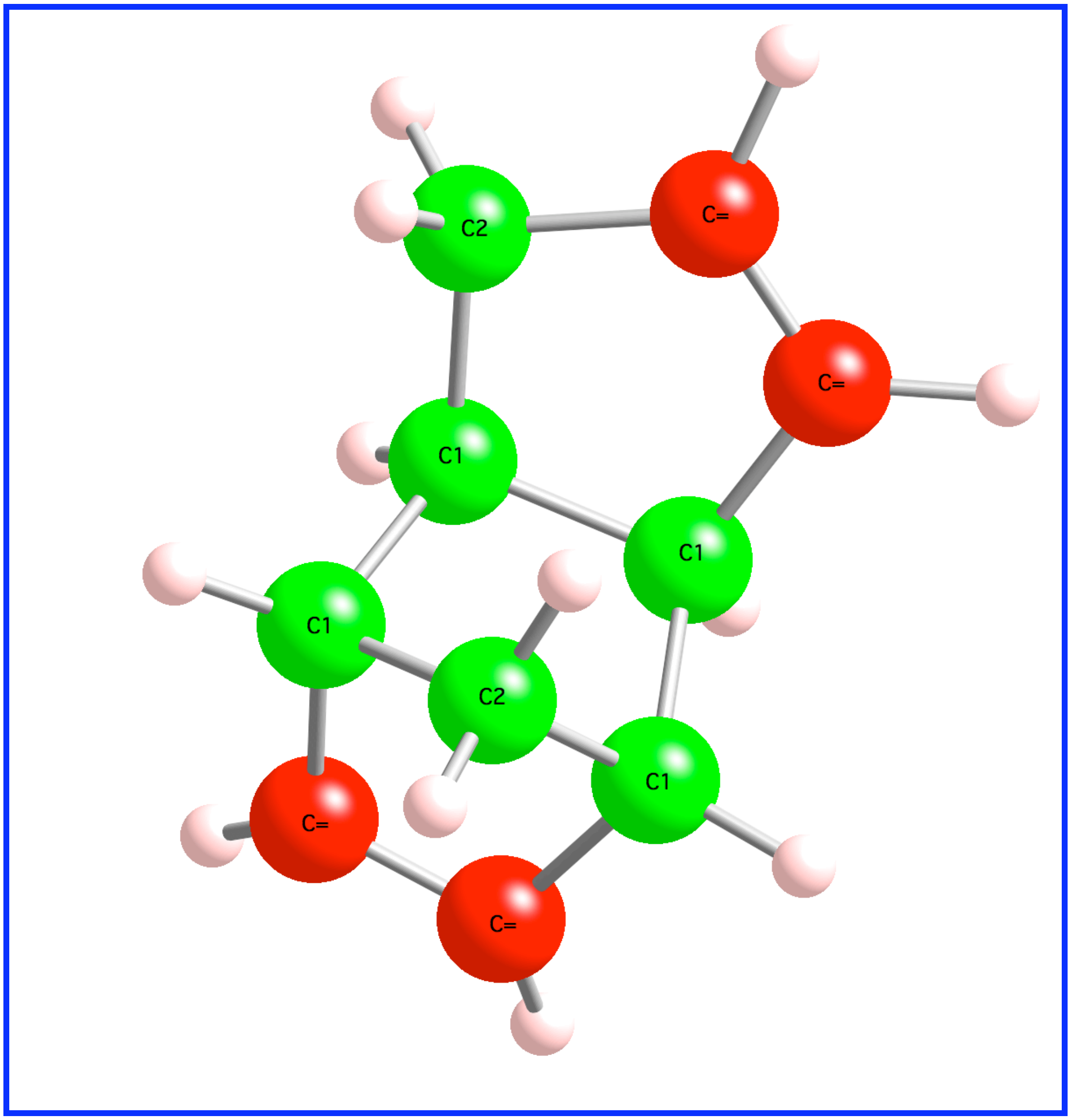

Figure 3.1: Molecular Structure of DCPD: red-sp_2Carbon, green-sp_3Carbon , C1-Carbon attached to 1 Hydrogen, C2 Carbon attached to 2 Hydrogen. The bottom double bond is termed the norborene double bond and the top double bond is termed the cyclopentene double bond.

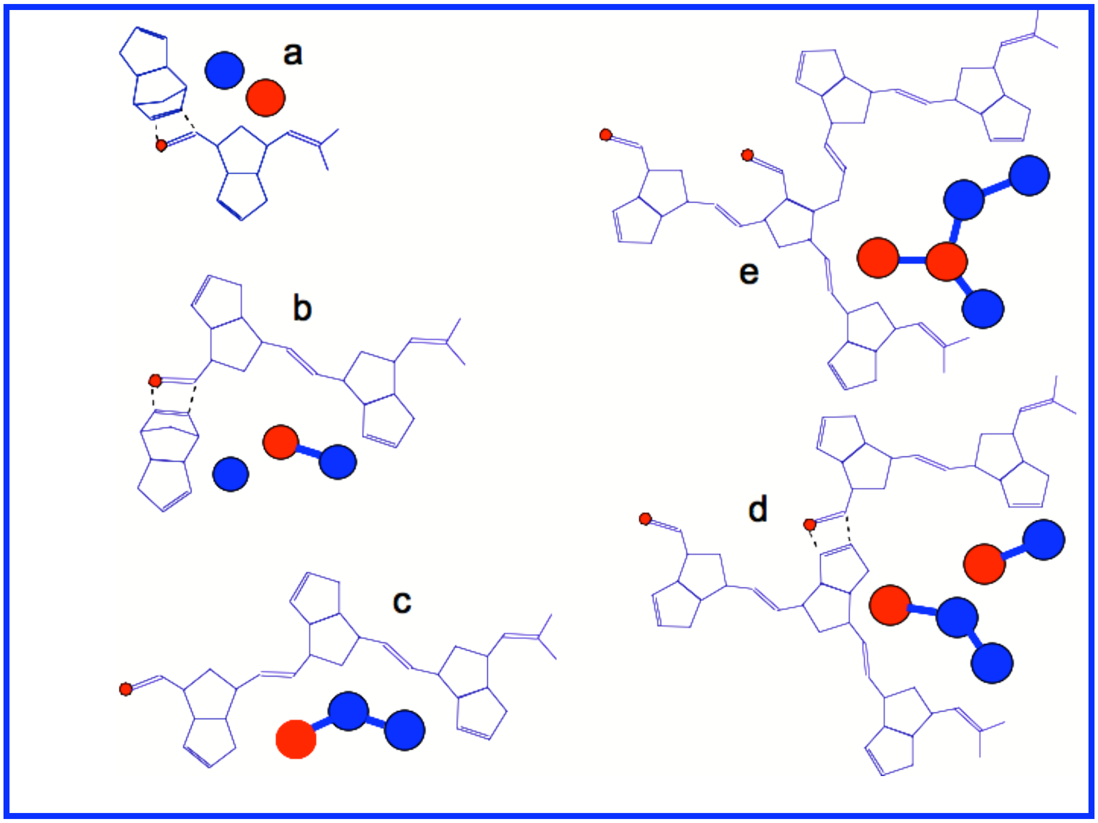

Figure 3.2: Schematic of the ROMP process for DCPD polymerization in atomistic and coarse grained detail. a) catalyst initiation b) propagation initiation c) propagation reaction completed d) cross-link initiation e) cross-link completed. Pursuant to a proximity criteria reaction (b) occurs with unit probability, reaction (d) takes place with probability 0.2. Refer text

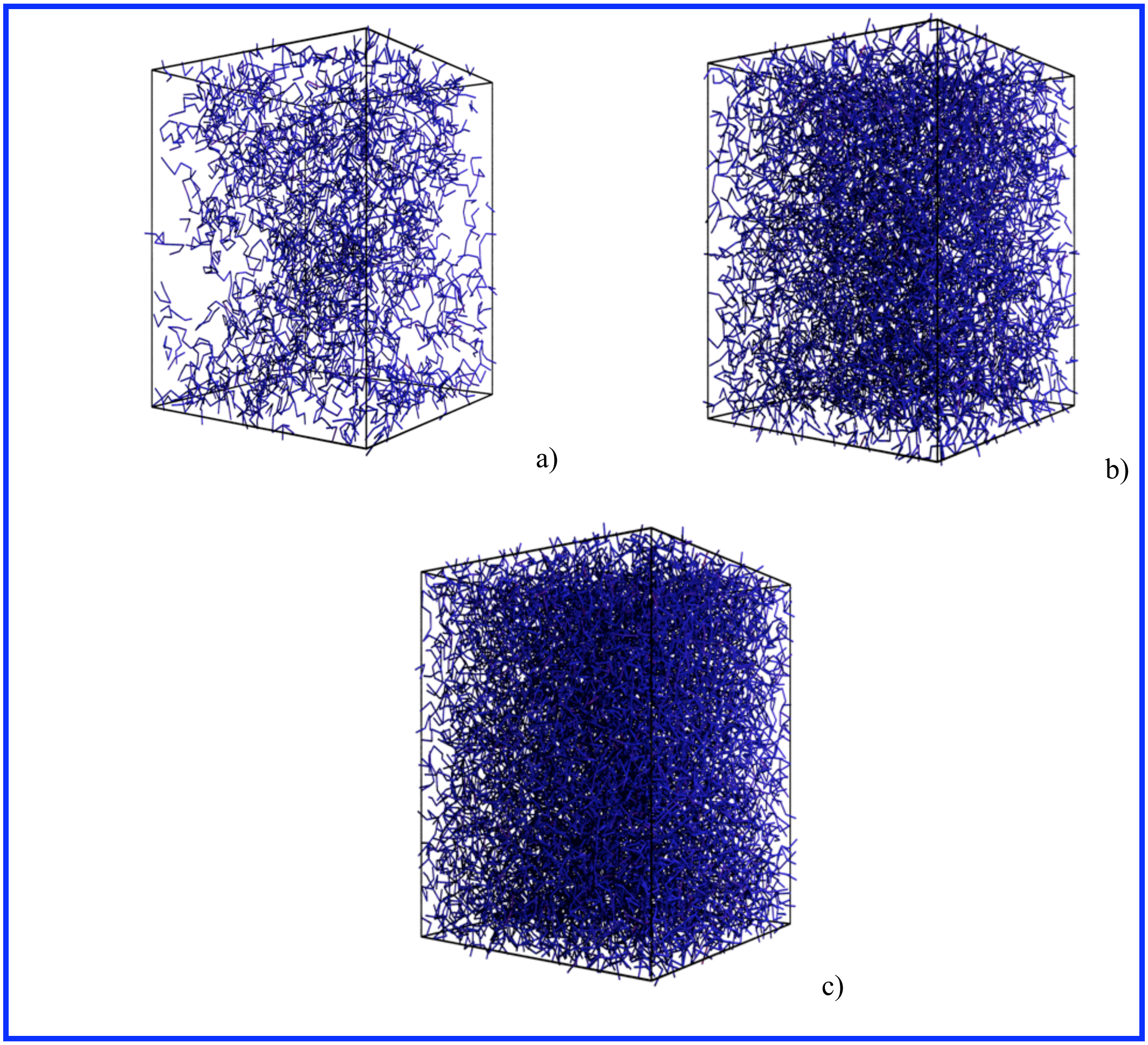

Figure 3.3: Coarse grained simulation viewgraphs at 14%, 35% and 58% degree of reaction. Only the bonded network is shown for clarity

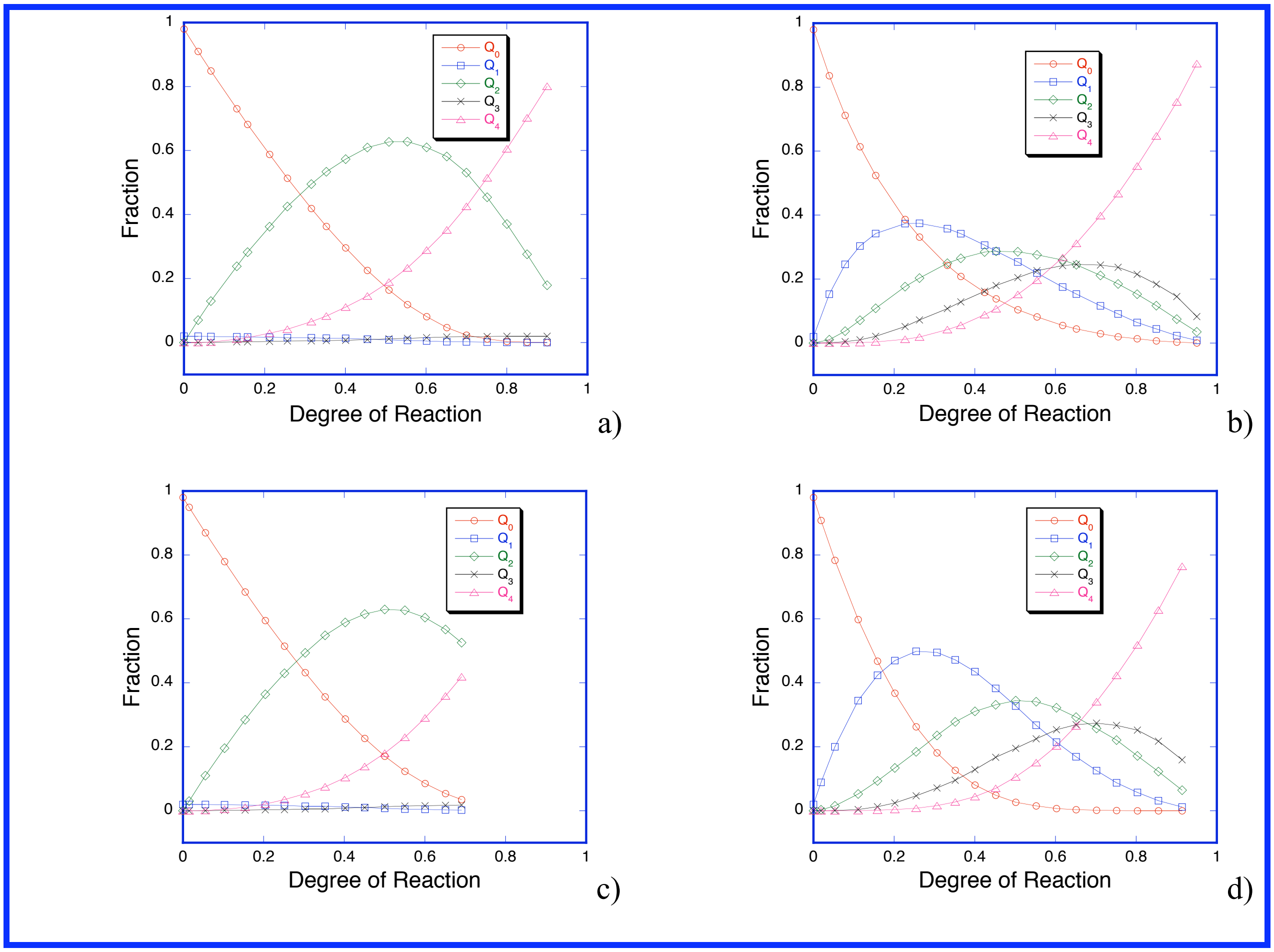

Figure 3.4: Morphology of Networks: plots of fraction of nodes with x number of bonds denoted as Q_x versus degree of reaction a) ROMP networks without angular constraints b) RANDOM networks without angular constraints c) ROMP network with angular constraint and d) RANDOM network with angular constraint. The species Q_0 Q_1 Q_2 Q_3 Q_4 are beads with 0,1,2,3,4 bonds attached respectively. Additionally the Q_1 and Q_3 species in ROMP networks are catalysts.

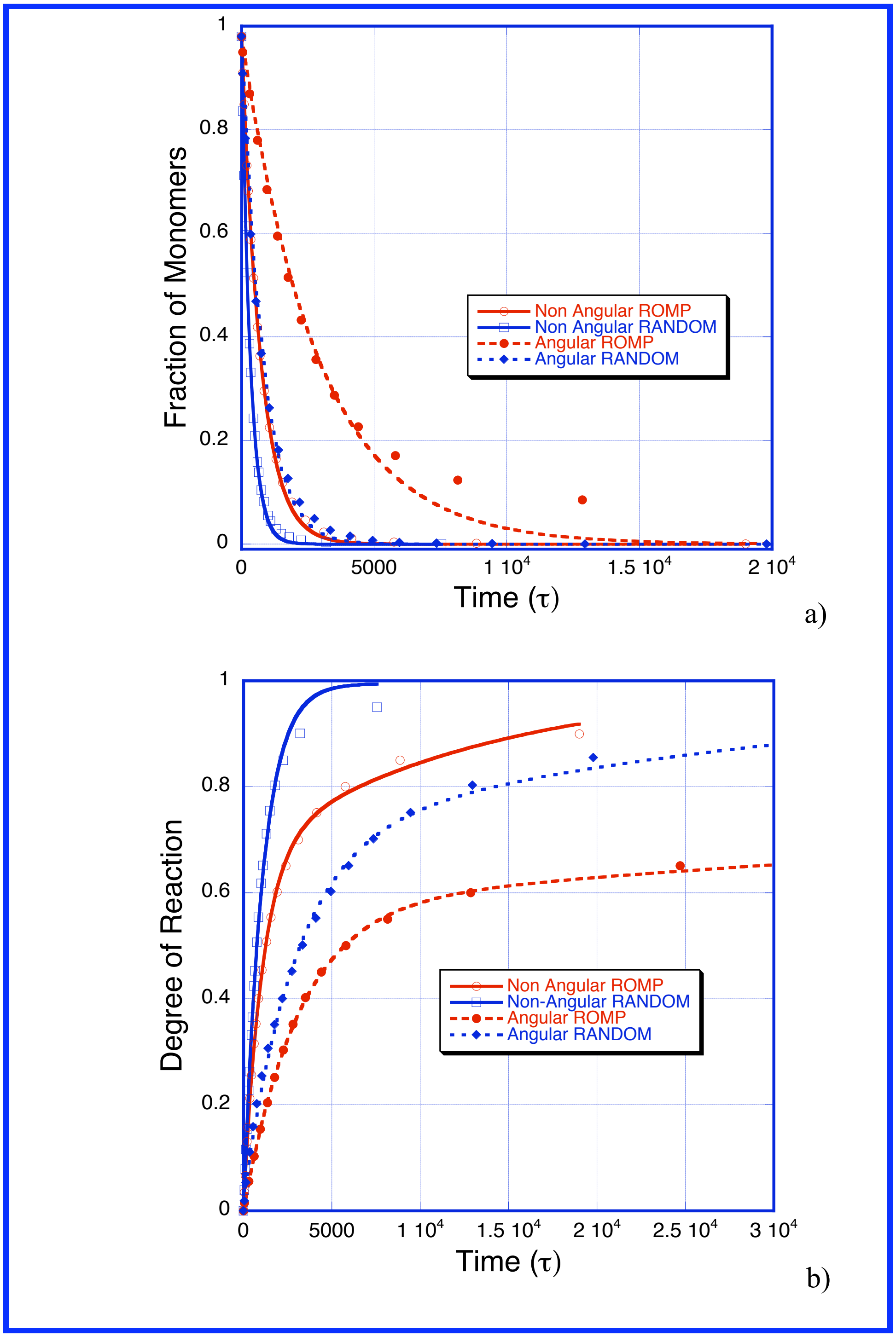

Figure 3.5: Kinetics for ROMP/RANDOM of networks generated using interaction models with and without angular constraints: a) Concentration of monomers versus time (LJ units), line is the curve fit to eqn(3.5) b) degree of reaction versus time (LJ units), lines are the curve fits to eqn(3.6). The fit parameters are tabulated in Table 3.1.

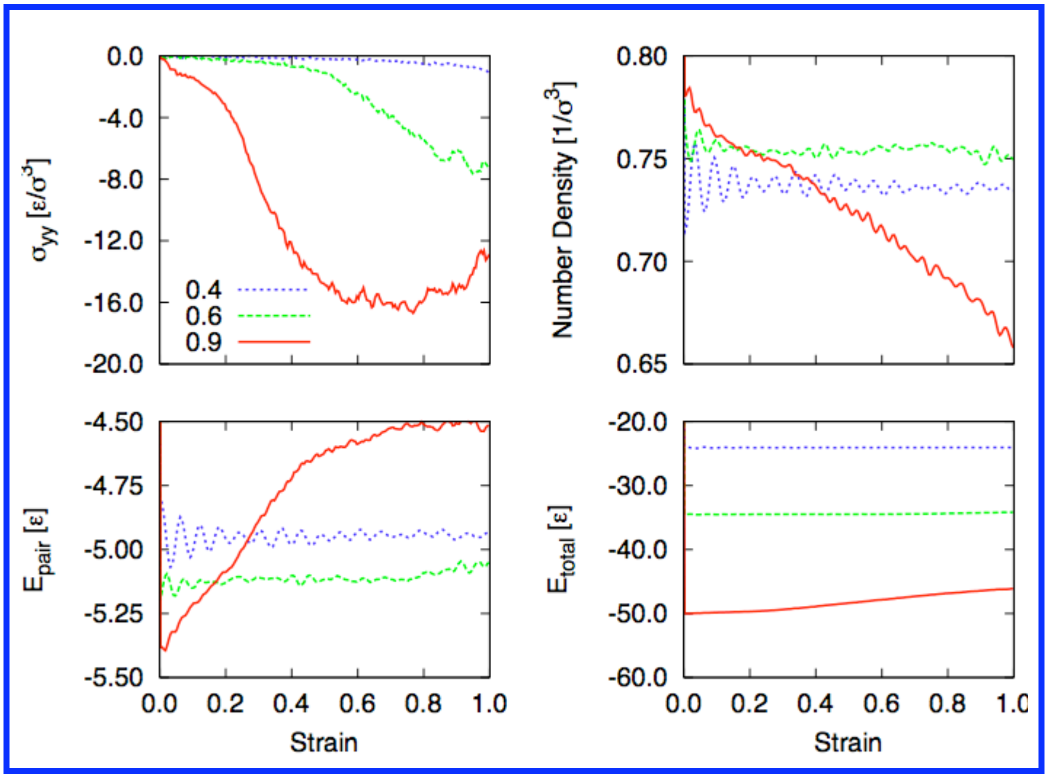

Figure 3.6: Behavior of ROMP network without angular constraints at (α = 0.4,0.6,0.9) versus strain a) stress σ_{yy} b) number density c) pair interaction energy d) total energy. Note that the oscillations of pair energy and number density are artifacts of the barostat. The number density, pair and the total energies do not change significantly with deformation for $\alpha<\alpha_Y$ (α_Y~0.6). Only at $\alpha>\alpha_P$ (α_P~0.8) do we see significant changes in number density, pair or total energies, however there is still a stress response without internal energy or density changes at $\alpha_P>\alpha>\alpha_Y$ an example of which can be seen in the curves at α = 0.6

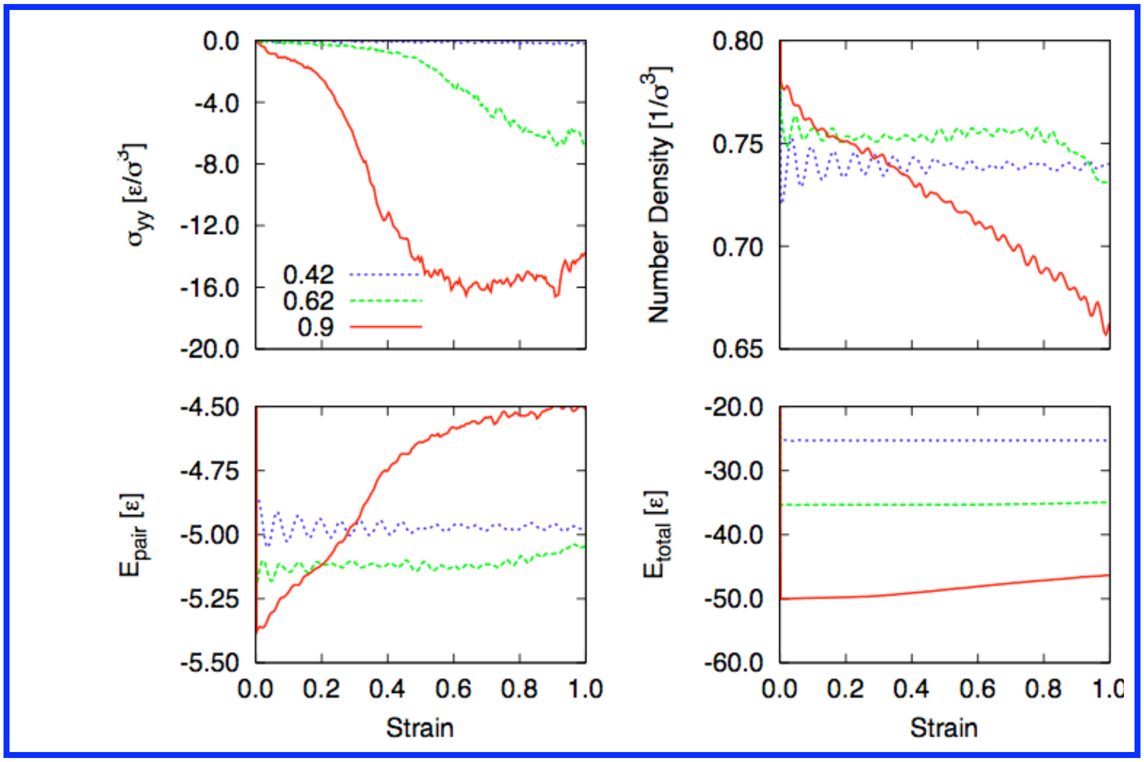

Figure 3.7: Behavior of RANDOM network without angular constraints at (α = 0.42,0.62,0.9) versus strain a) stress σ_{yy} b) number density c) pair interaction energy d) total energy. The oscillations of pair energy and number density are artifacts of the barostat. The number density, pair and the total energies do not change significantly with deformation for $\alpha<\alpha_Y$ (α_Y~0.6). Only at $\alpha>\alpha_P$ (α_P~0.8) do we see significant changes in number density, pair or total energies, however there is still a stress response without internal energy or density changes at $\alpha_P>\alpha>\alpha_Y$ an example of which can be seen in the curves at α = 0.62

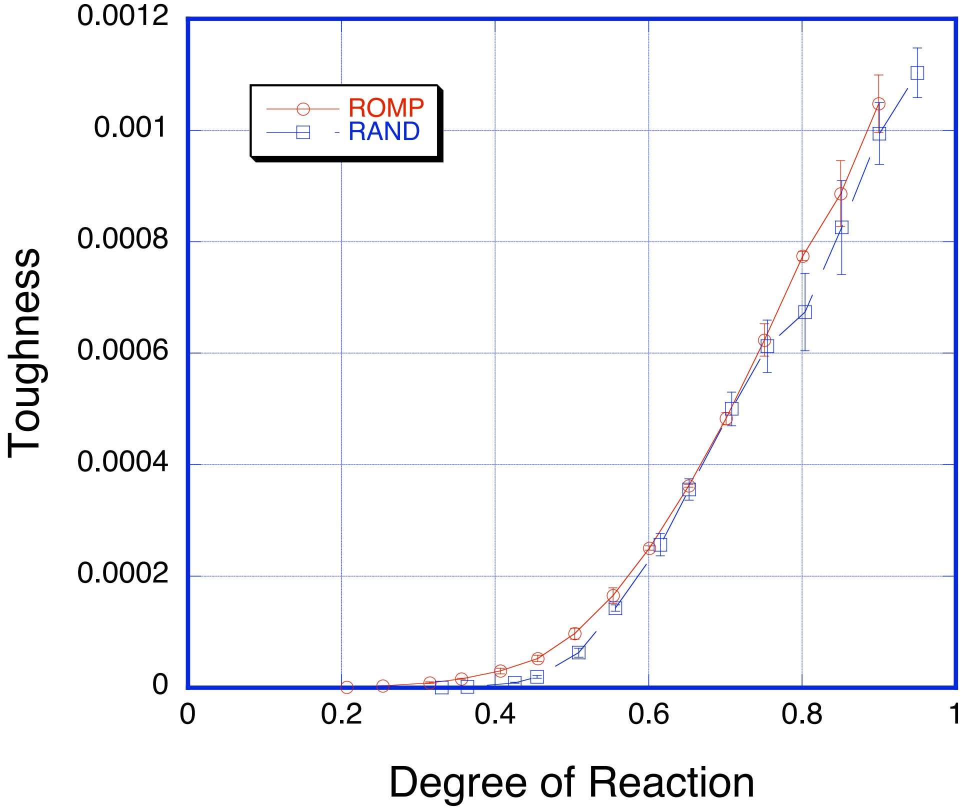

Figure 3.8: Toughness of networks without angular constraints. Both ROMP and RANDOM network seem to show a toughness percolation starting at a degree of reaction ~0.4.

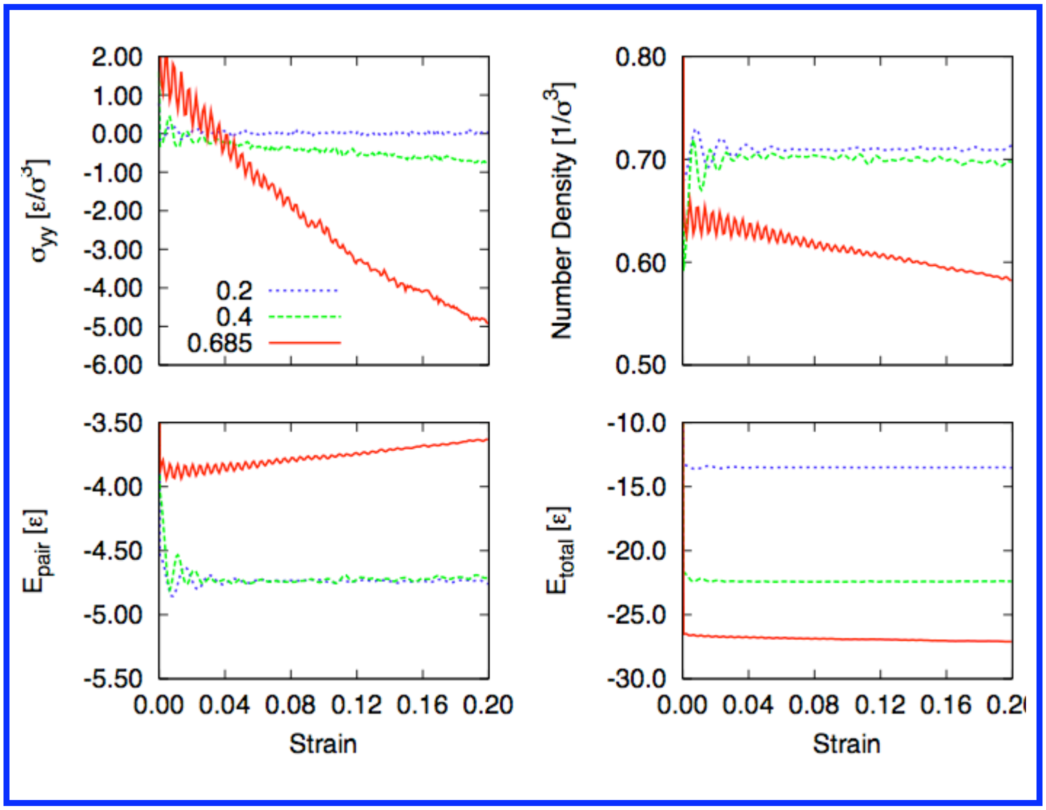

Figure 3.9: Behavior of ROMP network with angular constraints at (α = 0.2,0.4,0.685) versus strain a) stress σ_{yy} b) number density c) pair interaction energy d) total energy. Note that the oscillations of pair energy and number density are artifacts of the barostat. The number density, pair and the total energies do not change significantly with deformation for $\alpha<\alpha_Y$ (α_Y~0.3). Only at $\alpha>\alpha_P$ (α_P~0.4) do we see significant changes in number density, pair or total energies, however there is still a stress response without internal energy or density changes at $\alpha_P>\alpha>\alpha_Y$ an example of which can be seen in the curves at α = 0.4. The initial 0 strain σ_{yy} at high α is not zero since relaxation of x and z box dimension does not relax σ_{yy}.

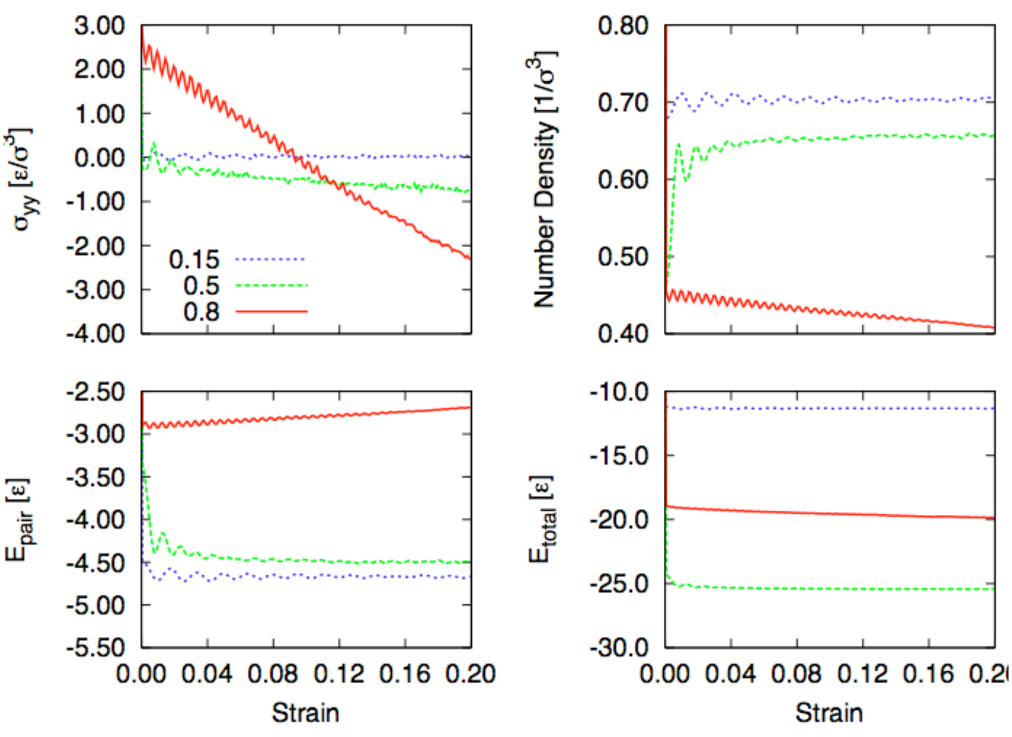

Figure 3.10: Behavior of RANDOM network with angular constraints at (α = 0.15,0.5,0.8) versus strain a) stress σ_{yy} b) number density c) pair interaction energy d) total energy. Note that the oscillations of pair energy and number density are artifacts of the barostat. The number density, pair and the total energies do not change significantly with deformation for $\alpha<\alpha_Y$ (α_Y~0.4). Only at $\alpha>\alpha_P$ (α_P~0.55) do we see significant changes in number density, pair or total energies, however there is still a stress response without internal energy or density changes at $\alpha_P>\alpha>\alpha_Y$ an example of which can be seen in the curves at α = 0.5. The initial 0 strain σ_{yy} at high α is not zero since relaxation of x and z box dimension does not relax σ_{yy}.

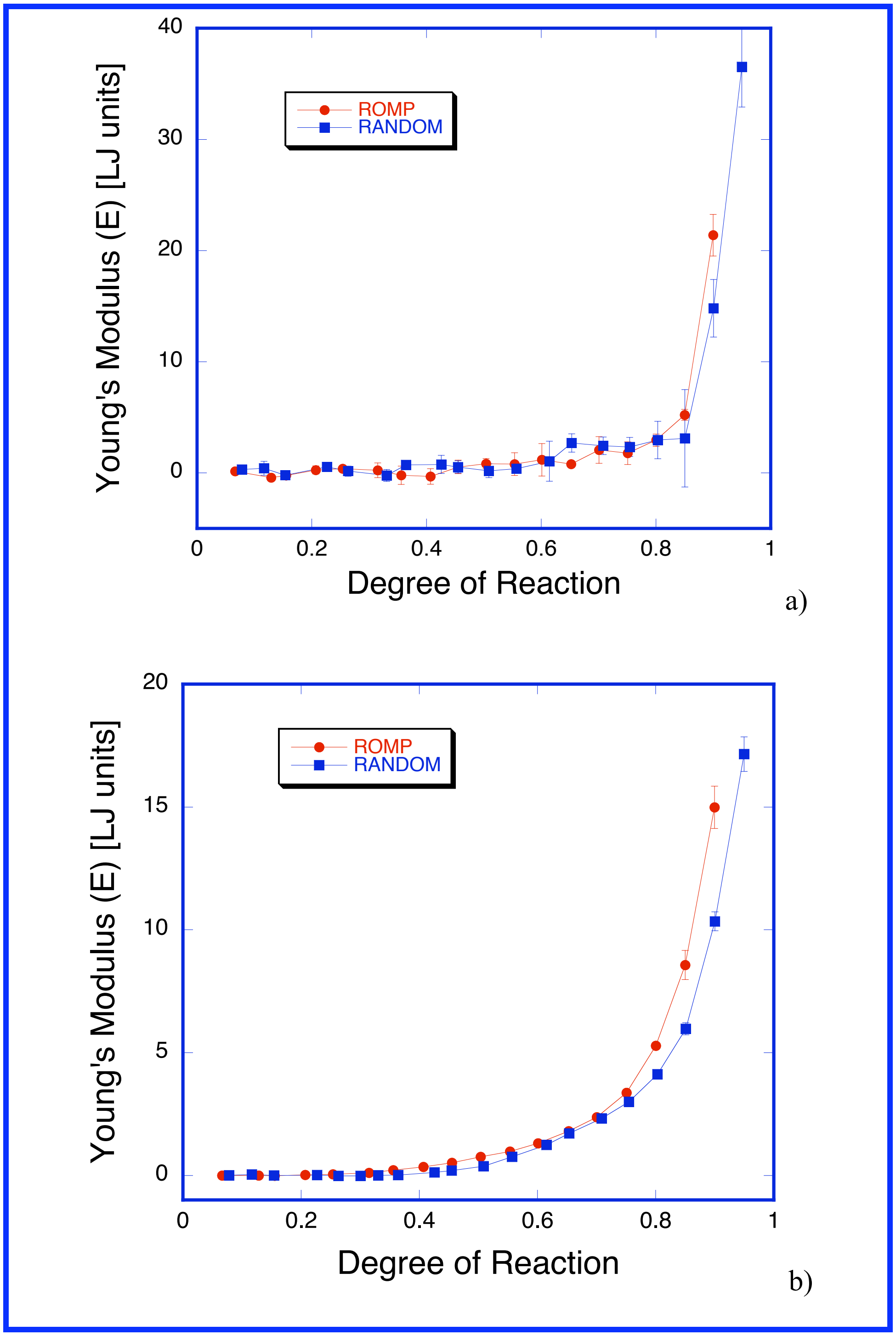

Figure 3.11: Young’s modulus of networks without angular constraints at a) 1% strain b) 20% strain. The threshold for drastic change in modulus behavior is strain dependant. However the 1% extension seems to closely mirror Poisson’s ratio behavior in Figure 3.13.

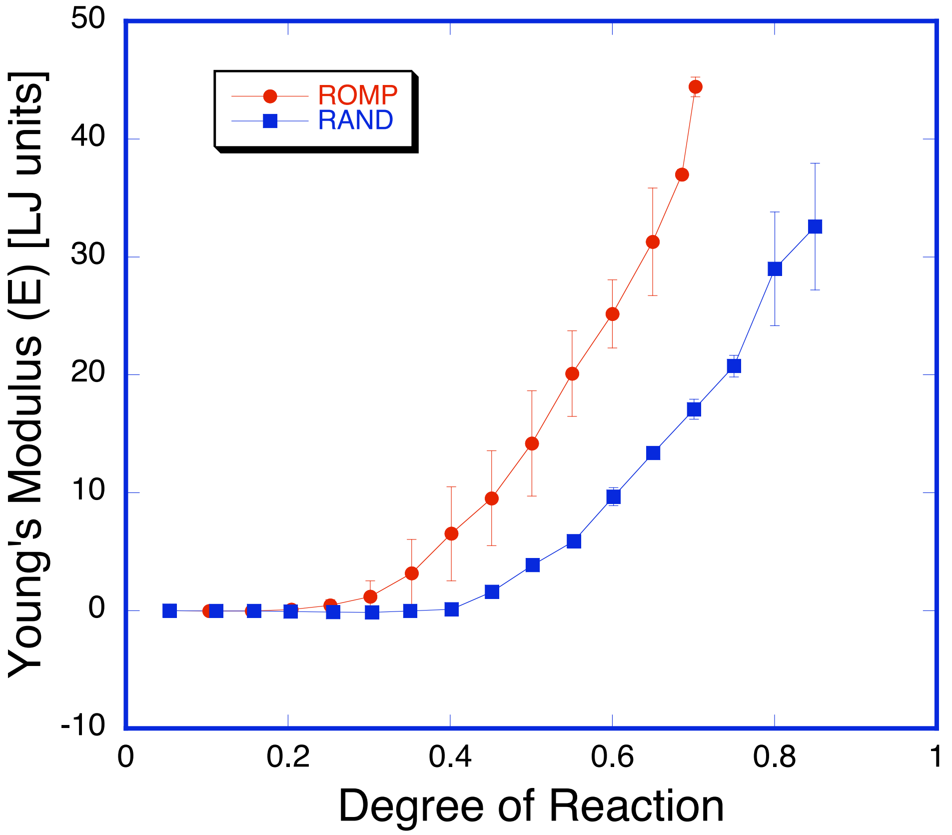

Figure 3.12: Young's modulus of networks with angular constraints. The ROMP network appears to show a threshold (α_Y) starting at degree of reaction ~0.3, the RANDOM network shows threshold (α_Y) starting around 0.4.

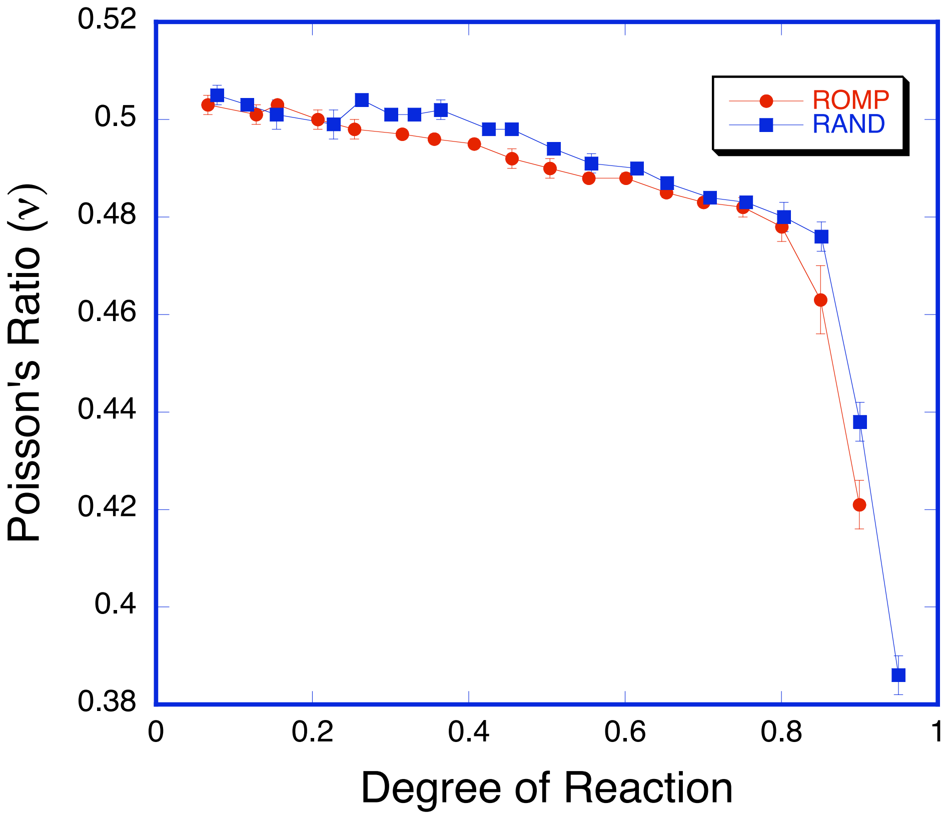

Figure 3.13: Poisson's ratio for networks without angular constraints. There appears to be 2 regions separated at degree of reaction ~0.8. The first linear regime below a threshold (α_P) = 0.8 suggests the response to deformation is predominantly entropic. However the response after the 0.8 limit is predominantly enthalpic since the box is not able to retain a Poisson's ratio of ~0.5

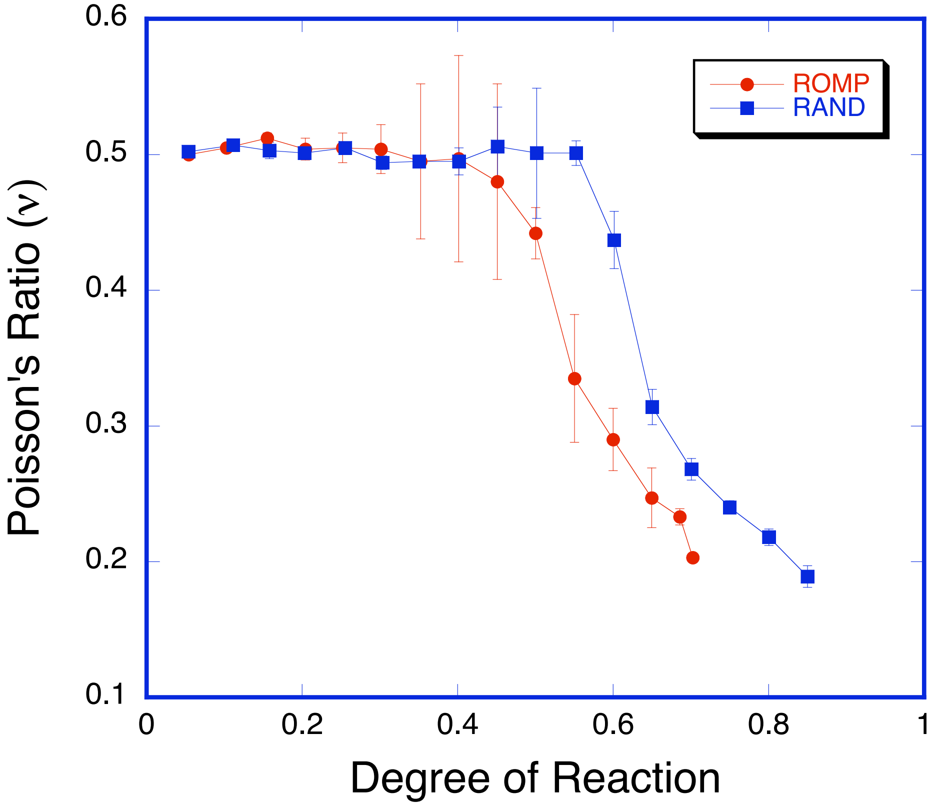

Figure 3.14: Poisson's ratio for network with angular constraints. The ROMP network appears to show a threshold α_P around degree of reaction ~0.4. The RANDOM network shows a threshold around 0.6. These thresholds are different from the threshold exhibit by the Young's modulus curves.

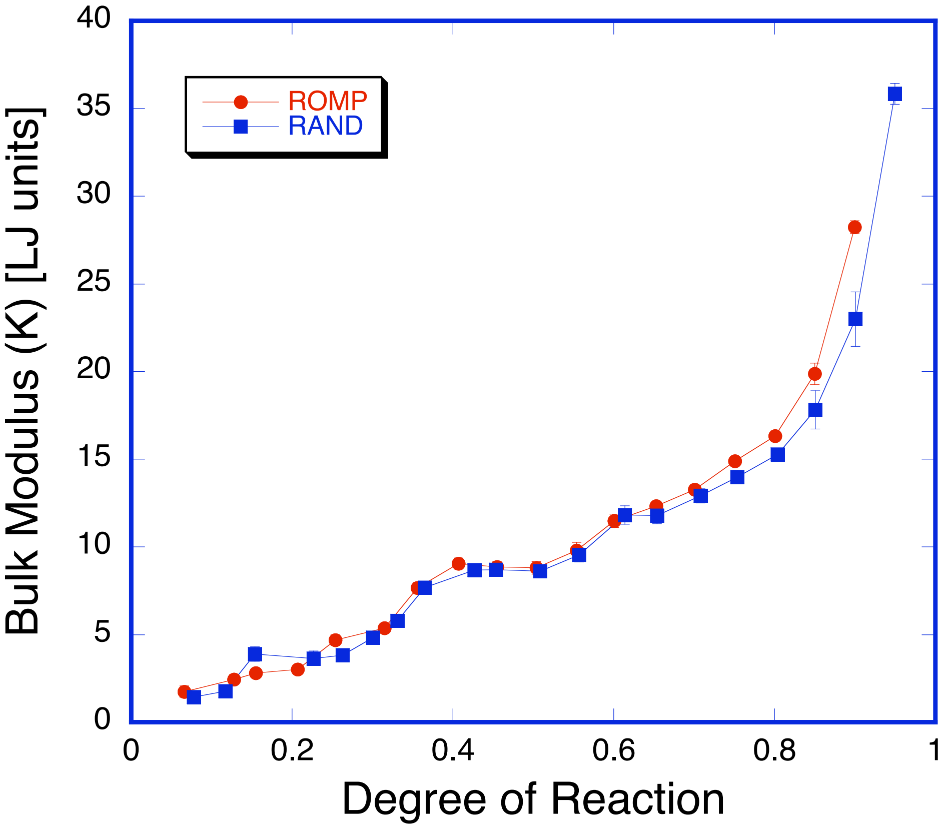

Figure 3.15: Bulk modulus of ROMP and RANDOM networks without angular constraints. We find 2 linear regimes separated at degree of reaction ~0.8. This tends to correlate with the behavior of the Young' modulus at low strain in Figure 3.11 and the Poisson's ratio behavior in Figure 3.13.

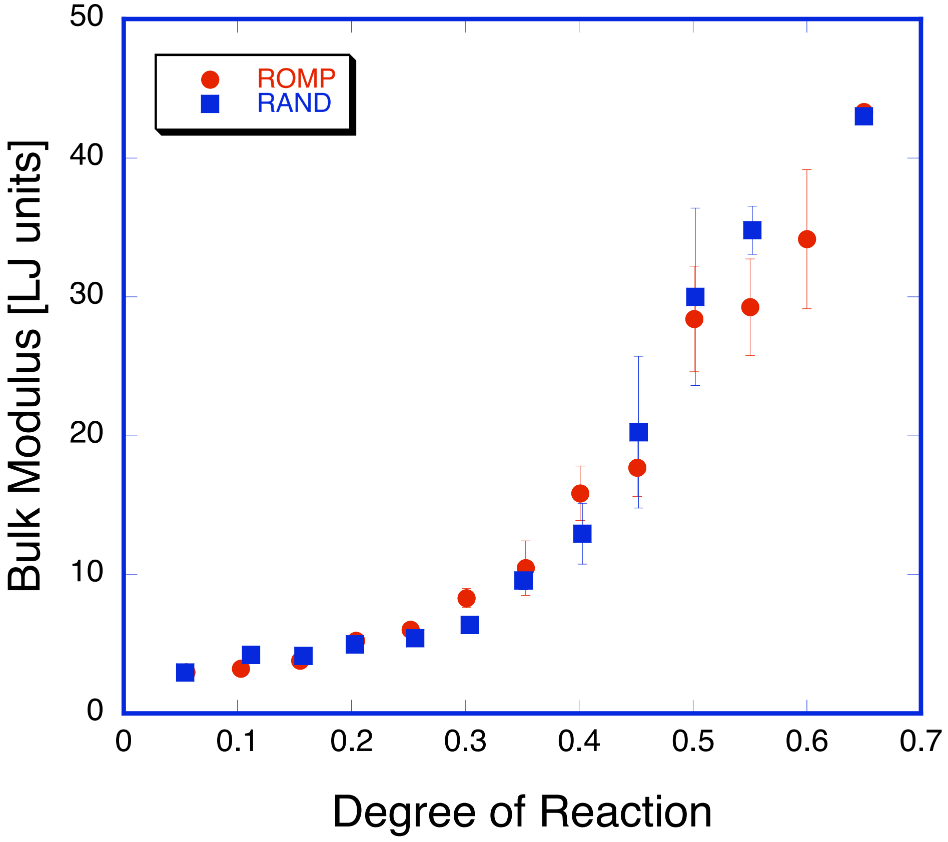

Figure 3.16: Bulk modulus for ROMP and RANDOM networks with angular constraints. There are 2 linear regimes separated at a degree of reaction ~0.3 in both ROMP and RANDOM cases. These 2 regions appears to be separated at a threshold α_Y

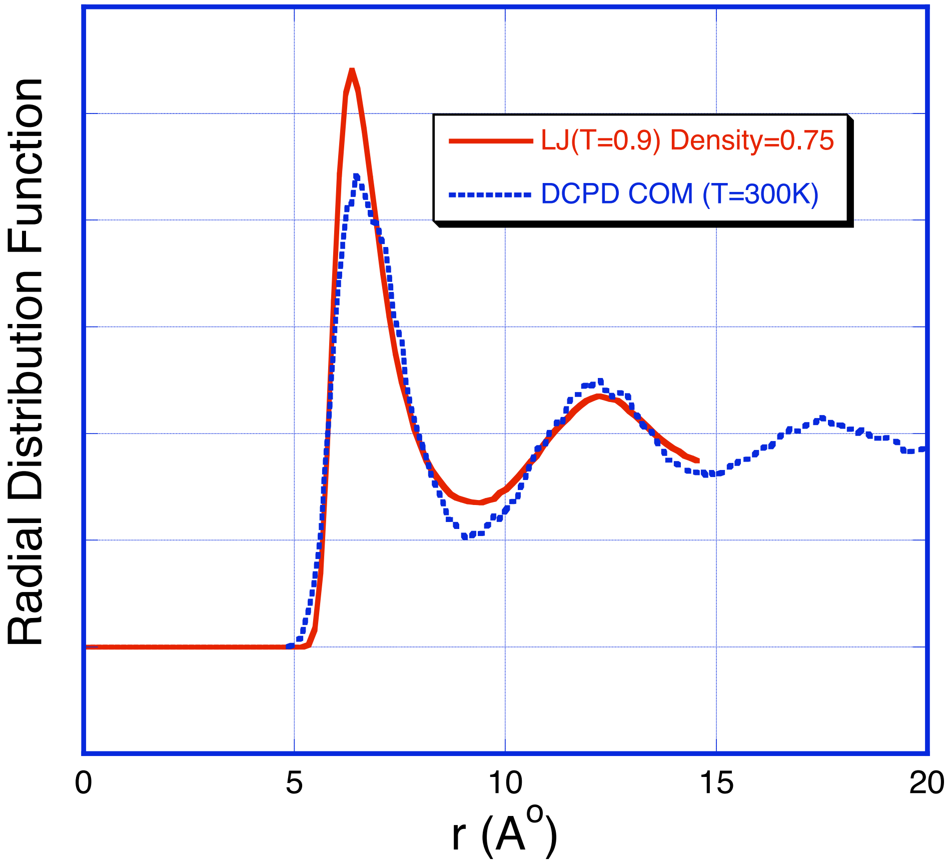

Figure 3.17: DCPD center of mass pair correlation functions calculated using COMPASS potential using all atom representation of DCPD molecules equilibrated at 300K and 1 atmosphere pressure (details in Chapter 4) and LJ system: σ of the LJ scaled by 5.85 A^o

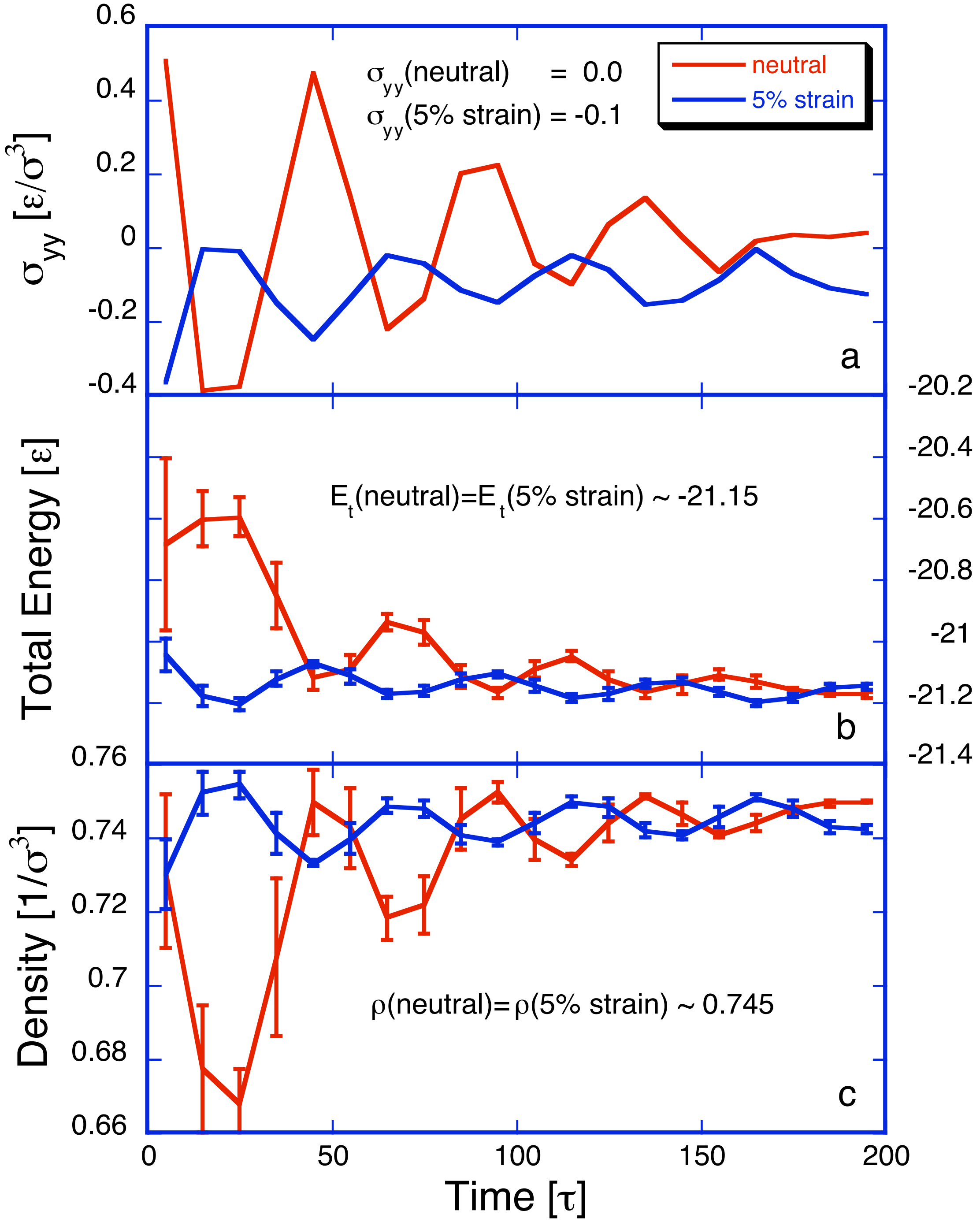σ_yy [ε/σ³]
0.6
0.4
0.2
0
-0.2
-0.4
σ_yy(neutral) = 0.0
σ_yy(5% strain) = -0.1
neutral
5% strain
a
Total Energy [ε]
-20.2
-20.4
-20.6
-20.8
-21
-21.2
-21.4
E_t(neutral)=E_t(5% strain) ~ -21.15
b
Density [1/σ³]
0.76
0.74
0.72
0.7
0.68
0.66
ρ(neutral)=ρ(5% strain) ~ 0.745
c
0
50
100
150
200
Time [τ]

Figure 3.18: Behavior of a ROMP network with angular constraints at α = 0.35 at neutral strain and 5% tensile strain versus equilibration time showing a) stress b) internal energy c) number density response. From eqn(3.15) the expected change in internal energy is 0.002 at 5% strain is difficult to discern from thermal noise. Density difference after deformation is negligible indicative of rubbery elasticity

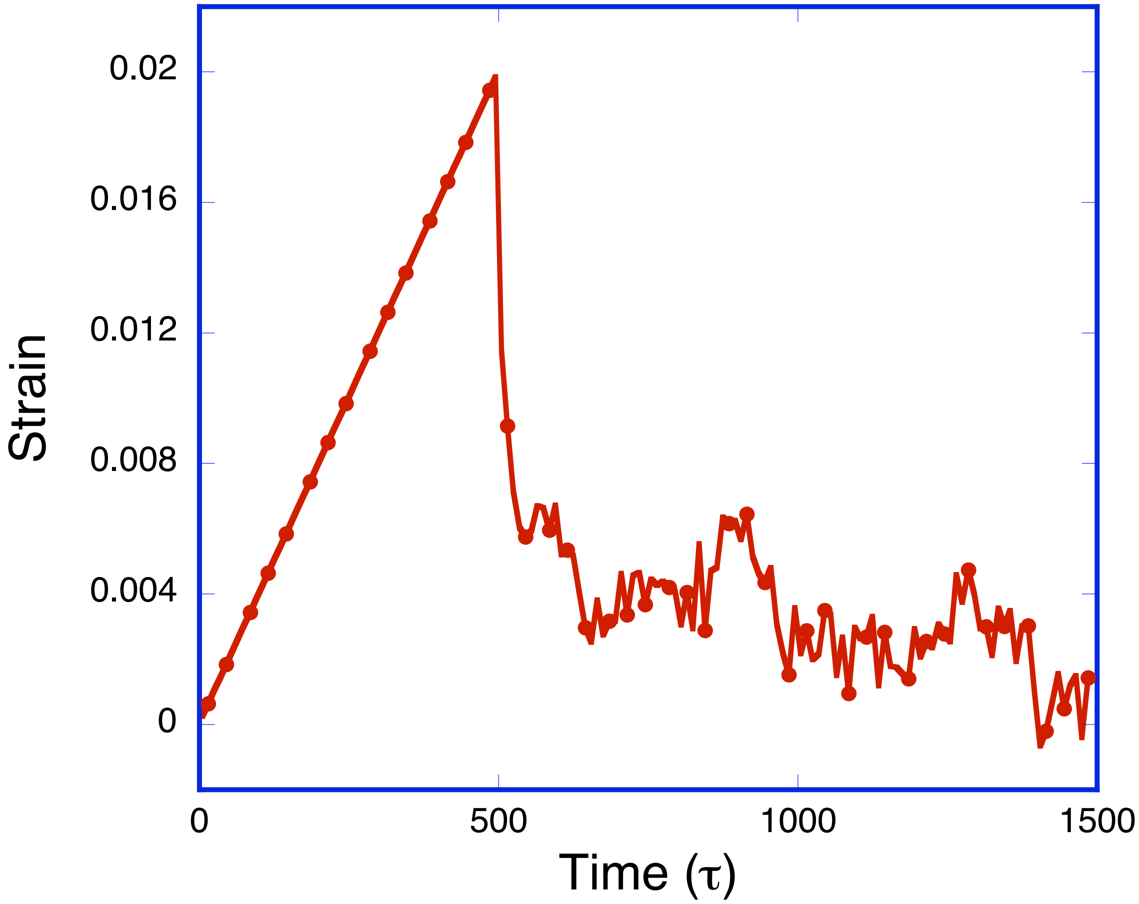

Figure 3.19: ROMP network with angular constraints (α = 0.40) uniformly extended in the y dimension to a final strain of 2%. The subsequent recovery to regain zero strain is indicative of entropic response since a viscous liquid would retain strained state.

3.10 References

1. Nguyen, S. T., Johnson, L. K., Grubbs, R. H. & Ziller, J. W. Ring-opening metathesis polymerization (ROMP) of norborene by a Group VIII carbene complex in protic media. *Journal of the American Chemical Society* **114**, 3974-3975 (1992).
2. Chubynsky, M. V. & Thorpe, M. F. Self-organization and rigidity in network glasses. *Current Opinion in Solid State and Materials Science* **5**, 525-532 (2001).
3. White, S. R. et al. Autonomic healing of polymer composites. *Nature* **409**, 794-797 (2001).
4. Maiti, S., Shankar, C., Geubelle, P. H. & Kieffer, J. Continuum and molecular-level modeling of fatigue crack retardation in self-healing polymers. *Journal of Engineering Materials and Technology-Transactions of the ASME* **128**, 595-602 (2006).
5. Constable, G., Lesser, A. & Coughlin, B. Ultrasonic Spectroscopic Evaluation of the Ring-Opening Metathesis Polymerization of Dicyclopentadiene. *Journal of Polymer Science: Part B: Polymer Physics* **41**, 1323-1333 (2003).
6. Barnes, S. E. et al. Raman spectroscopic studies of the cure of dicyclopentadiene (DCPD). *Spectrochimica Acta Part A-Molecular and Biomolecular Spectroscopy* **61**, 2946-2952 (2005).
7. Schaubroeck, D., Brughmans, S., Vercaemst, C., Schaubroeck, J. & Verpoort, F. Qualitative FT-Raman investigation of the ring opening metathesis polymerization

of dicyclopentadiene. *Journal of Molecular Catalysis A: Chemical* **254**, 180-185 (2006).

8. Kessler, M. R. & White, S. R. Cure kinetics of the ring-opening metathesis polymerization of dicyclopentadiene. *Journal of Polymer Science Part A-Polymer Chemistry* **40**, 2373-2383 (2002).
9. Tuckerman, M. E., Martyna, G. J. & Berne, B. J. Molecular dynamics algorithm for condensed systems with multiple time scales. *The Journal of Chemical Physics* **93**, 1287-1291 (1990).
10. Plimpton, S. Fast Parallel Algorithms for Short-Range Molecular Dynamics. *Journal of Computational Physics* **117**, 1-19 (1995).
11. Heine, D. R., Grest, G. S., Lorenz, C. D., Tsige, M. & Stevens, M. J. Atomistic simulations of end-linked poly(dimethylsiloxane) networks: Structure and relaxation. *Macromolecules* **37**, 3857-3864 (2004).
12. Svaneborg, C., Grest, G. S. & Everaers, R. Disorder effects on the strain response of model polymer networks. *Polymer* **46**, 4283-4295 (2005).
13. Barsky, S. J. et al. Elastic properties of randomly cross-linked polymers. *Physical Review E. Statistical Physics, Plasmas, Fluids, and Related Interdisciplinary Topics* **54**, 5370-5376 (1996).
14. Kremer, K. & Grest, G. S. Dynamics of entangled linear polymer melts: A molecular-dynamics simulation. *The Journal of Chemical Physics* **92**, 5057-5086 (1990).
15. Thorpe, M. F. Continuous deformations in random networks. *Journal of Non-Crystalline Solids* **57**, 355-370 (1983).

16. Yin, T., Rong, M. Z., Zhang, M. Q. & Yang, G. C. Self-healing epoxy composites–Preparation and effect of the healant consisting of microencapsulated epoxy and latent curing agent. *Composites Science and Technology* **67**, 201-212 (2007).
17. A., M., F., C. & A., F. C. Vapour,ÄìLiquid Equilibrium Properties for Two- and Three-dimensional Lennard-Jones Fluids from Equations of State. *Australian Journal of Physics* **52**, 101-115 (1999).
18. Chickos, J. S., Hillesheim, D., Nichols, G. & Zehe, M. J. The enthalpies of vaporization and sublimation of exo- and endo-tetrahydrodicyclopentadienes at T=298.15 K. *The Journal of Chemical Thermodynamics* **34**, 1647-1658 (2002).

Chapter 4
All Atomistic ROMP Catalyzed DCPD Networks

4.1 Introduction

In Chapter 3 we explored the formation of two different types of cross-linked networks and came to the conclusion that it is necessary to create fully atomistic representation of the molecular networks. The DCPD ROMP system has not been studied using simulations due to its complex chemistry and a myriad of possible reaction pathways. The plethora of ROMP catalysts now commercially available with different activities and selectivities make it even more challenging to study. Different ROMP catalysts lead to different network topologies and therefore different mechanical properties. Even more challenging is the extreme difficulty of experimentally characterizing the degree of reaction and correlating the degree of reaction with the mechanical properties. Recently some experimental studies of DCPD undergoing ROMP reactions looking at reaction extent by Raman scattering with concurrent mechanical property characterization by Brillouin scattering is being conducted at our research group. It is expected that these results in conjunction with this simulation effort will be able to characterize the DCPD ROMP system in new and more accurate ways. Chapter 5 discusses some of these details.

Generation of realistic molecular networks of cross-linked polymers remains a difficult proposition. Most simulation works in this area have so far been limited to topologically defined networks created to exact specifications so as to test current theories of cross linked polymer behavior, particularly the rubbery characteristics of sparsely cross linked chains. Ring opening metathesis polymerization (ROMP) of dicyclopentadiene (DCPD) on the other hand results in highly cross-linked networks. Physical details about the topology remain extremely difficult to evaluate due to the stochastic nature of the reaction process and the inability of conventional techniques such as XRD to reveal anything more than nearest neighbor distances between individual species in the amorphous polymer matrix. Experimental methods of exploring the network structure include FTIR and Raman spectroscopy[1,2]. Schaubroeck et al[2] found unusual features in the in-situ FTIR spectra of poly-DCPD while undergoing reactions, making it difficult to determine the degree of cross-linking unambiguously. The Raman spectra for linear poly-DCPD show an atrophy of the peak associated with the cyclopentene double bond of DCPD, even though only the norborene ring was selectively reacting using a special ROMP catalyst. Hence, when the norborene ring undergoes ROMP it causes shifts in FTIR/Raman peaks that coincide with those that would occur if the cyclopentene ring reacted. However Raman spectra investigations of DCPD undergoing ROMP reactions by Schaubroeck show experimental evidence for the maximum degree of reaction attainable by the system to be around 0.6-0.7. Our simulations of ROMP networks with angular constraints closely approximate the experimentally achieved extent of reaction, where a maximum degree of reaction of 0.7 was attained. Beyond the aforementioned studies, no further experimental evidence for the actual extent of cross-linking could be found in the literature. The actual mechanism by which the reaction of the norborene site affects the unreacted cyclopentene site and vice versa is unknown. Our modeling approach for recreating DCPD network structures is based on the knowledge concerning reaction mechanisms that is currently available in the literature. However, simulation easily allows us to explore possible scenarios and deduce the most likely mechanism based on how well experimental results are reproduced.

To the best of our knowledge only recently have a few groups successfully implemented atomistic or united atom models of network polymers. Wu and Xu[3] constructed an all-atomistic model of epoxy network. Heine et al [4] have developed a coarse-grained model of end-linked polydimethylsiloxane networks using a recently developed united atom force field. Komarov et al[5] used a coarse-grained approach for constructing epoxy networks using a hybrid Monte Carlo (MC) and molecular dynamics procedure. Their work is especially interesting in their attempt recast the coarse grained networks to an all atom representation.

This chapter is arranged as follows. Section 4.2 discusses the force field details of the system, Section 4.3 explains the reaction procedure for forming networks, Section 4.4 articulates the structural characteristics of the evolving network and mechanical testing procedure and results thereof is discussed in section 4.5. The stress, internal energy, and density response behavior of networks to applied strain is shown in Section 4.6. Section 4.7 outlines some general conclusions.

4.2 Force-field Discussion

The all-atomistic force field for species in our simulation is the widely used class-II *COMPASS* potential.[6] This potential is widely used in simulation research in commercial software such as Material Studio distributed by Accelrys Inc. The *COMPASS* force field was chosen due to the ability to describe the unique features of complex organic molecules that responds to applied forces with a complex combination of bond, angular and dihedral deformations. Some of these features are currently unavailable in potentials such as Stillinger Weber (SW) or our in-house reactive FLX potential. Both these potentials are superior to the class-II *COMPASS* force field since they allow multiple coordination capability based on neighboring criteria. Even though such reactive potentials are invaluable for identifying the correct reaction mechanisms, as our initial studies showed, letting the ROMP process happen naturally would take a prohibitively long time to achieve any significant degrees of cure for DCPD in any reasonable time frame. We therefore developed a simulation scheme described below, and based it on a simpler potential for which the correct angular, dihedral, bonding and improper interaction parameters for DCPD already existed. We note that as the network evolution of DCPD takes place there is a net conservation of double bonds and no atomic species actually changes its coordination number or species type, though the double bonded carbons on DCPD did change their bonded neighbors upon reaction. Effectively it means that there is no need to develop a potential that physically maps the transition from one coordination profile to its final reacted form. This is a major advantage since the molecular species remain the same. Therefore pair, bond, dihedral and improper parameters do not change before and after a reaction in the DCPD ROMP system. With this intuition we designed a reaction code that updates the connectivity of the molecules in order to create the cross linked networks that were necessary for investigating the mechanical behavior of the network behavior at hand.

The functional form of the COMPASS potential is shown in eqn(4.1) through eqn(4.18). This potential has been implemented in the LAMMPS molecular dynamics engine [7].

$$E_{total} = E_{pair} + E_{bond} + E_{coul} + E_{angle} + E_{dihed} + E_{improper} \quad (4.1)$$

$$E_{pair} = \varepsilon\left(2\frac{\sigma^9}{r^9} - 3\frac{\sigma^6}{r^6}\right) \quad r < r_c \quad (4.2)$$

$$E_{bond} = k_2(r - r_o)^2 + k_3(r - r_o)^3 + k_4(r - r_o)^4 \quad (4.3)$$

$$E_{coul} = \frac{Kq_1q_2}{r^2} \quad (4.4)$$

For angle: $(i - j - k)$

$$E_{angle} = E_a + E_{bb} + E_{ab} \quad (4.5)$$

Where E_a is the angular term, E_{bb} is the bond-bond term, E_{ab} is the angle-bond term

$$E_a = K_2(\theta - \theta_o)^2 + K_3(\theta - \theta_o)^3 + K_4(\theta - \theta_o)^4 \quad (4.6)$$

$$E_{bb} = M(r_1 - r_{ij})(r_2 - r_{jk}) \quad (4.7)$$

$$E_{ab} = -[N_1(r_1 - r_{ij}) + N_2(r_2 - r_{jk})](\theta - \theta_o) \quad (4.8)$$

Where θ_0 is the equilibrium angle in radians and r_1 and r_2 are equilibrium bond lengths of $i - j$ and $j - k$ respectively. For dihedral $(i - j - k - l)$

$$E_{dihed} = E_d + E_{mbt} + E_{ebt} + E_{at} + E_{aat} + E_{bb13} \quad (4.9)$$

Where E_d is the dihedral term, E_{mbt} is the middle bond torsion term, E_{ebt} is the end bond torsion term, E_{at} is an angle torsion term, E_{aat} is an angle angle torsion term, E_{bb13} is a $i - j$ and $j - k$ bond-bond term.

$$E_d = \sum_{n=1}^{3} D_j\left[1 - \cos(n\phi - \phi_n)\right] \quad (4.10)$$

$$E_{mbt} = (r_{jk} - r_2)\left[A_1\cos(\phi) + A_2\cos(2\phi) + A_3\cos(3\phi)\right] \tag{4.11}$$

$$E_{ebt} = \begin{bmatrix} (r_{ij} - r_1)\left[B_1\cos(\phi) + B_2\cos(2\phi) + B_3\cos(3\phi)\right] + \\ (r_{kl} - r_3)\left[C_1\cos(\phi) + C_2\cos(2\phi) + C_3\cos(3\phi)\right] \end{bmatrix} \tag{4.12}$$

$$E_{at} = \begin{bmatrix} (\theta_{jk} - \theta_1)\left[D_1\cos(\phi) + D_2\cos(2\phi) + D_3\cos(3\phi)\right] + \\ (\theta_{ij} - \theta_2)\left[E_1\cos(\phi) + E_2\cos(2\phi) + E_3\cos(3\phi)\right] \end{bmatrix} \tag{4.13}$$

$$E_{aat} = M(\theta_{ijk} - \theta_1)(\theta_{jkl} - \theta_2)\cos(\phi) \tag{4.14}$$

$$E_{bb13} = N(r_{ij} - r_1)(r_{kl} - r_3) \tag{4.15}$$

Where ϕ is the dihedral angle, r_1 r_2 r_3 are equilibrium bond distances between $i-j$, $j-k$ and $k-l$.

For the improper or out of plane interactions for a quadruplet $ijkl$.

$$E_{improper} = E_i + E_{aa} \tag{4.16}$$

$$E_i = K\left[\frac{\chi_{ijkl} + \chi_{kjli} + \chi_{ljik}}{3} - \chi_o\right]^2 \tag{4.17}$$

$$E_{aa} = \begin{bmatrix} M_1(\theta_{ijk} - \theta_1)(\theta_{kjl} - \theta_3) + \\ M_2(\theta_{ijk} - \theta_1)(\theta_{ijl} - \theta_2) + \\ M_3(\theta_{ijl} - \theta_2)(\theta_{kjl} - \theta_3) \end{bmatrix} \tag{4.18}$$

Where E_i is the improper term and χ_{ijkl} refers to the angle between the plane ijk and jkl. Where χ_o is the out of plane angle set by parameters in the COMPASS forcefield. Atom j is the central atom of the quadruplet and the E_{aa} term takes the same coefficients as the E_{aat} in the dihedral interactions. The parameters used for each interaction are listed in Appendix A.

4.3 Network Generation Methodology

In this chapter a new method to create DCPD networks using a stochastic process following the ROMP mechanism shown in Figure 4.1 is explored. There are two major reactions that define the network, a) the ROMP exchange on the norborene ring and b) the ROMP exchange on the cyclopentene group. Noting that there is a tremendous variety of configurations that can result from simple modifications of parameters, catalysts and other features of the DCPD ROMP system, a wide variety of network configurations can be created. Some of the elements of the model implemented in our stochastic MD network generation scheme were chosen based on the best estimates of quantities that characterize the reacting molecular system. Some of the assumptions may need further fine-tuning to come up with a better model of the final network structure. However the absence of exact kinetic or structural data of the DCPD system during reaction, we believe that our method is a reasonable way of creating probable network configurations. Our approach uses a process that realistically recreates the random walk type reaction processes that the ROMP catalyst traces in space to create a putative polymer backbone. The key feature of the DCPD ROMP polymerization is the coupling between the double bonds in the rings of DCPD and the double bond carrying the Ruthenium catalyst, which results in opening of the ring and the transfer of Ruthenium to the newly attached DCPD entity, as shown in Figure 4.1. At the end of each reaction step the strained double bonds in the DCPD rings are able to achieve energetically more favorable/relaxed positions. We therefore work under the assumption that provided adequate spatial proximity between DCPD and catalyst all ROMP reactions are thermodynamically favorable and would occur given enough time. However we do note that this assumption need not always hold true. Even though a ring opening releases strain on a particular molecule, it is possible that the new bond formed causes more strain on the backbone the molecule is connected to.

To achieve thermodynamically valid network structures, we combine a Monte Carlo (MC) scheme stochastically scrutinizing the likelihood of double bond reconfiguration mechanisms to occur with MD simulations for post reaction relaxation, as described below. This algorithm allows us to achieve a large degree of reaction in reasonable time. We validate the approach by comparing the structural features of the networks so created and their properties with known experimental quantities.

The initial structure of the DCPD monomer was created using the Accelrys Discover software. The charge equilibration method [8] was used for a single molecule to determine the charge distribution. This was followed by energy minimization to get correct single molecule coordinates.

The Grubb's catalyst [9] is a complex molecule with large pendant ligands and a ruthenium center, as shown in the inset in Figure 4.1. An accurate representation of this molecule is computationally expensive along with the added requirement of procuring interaction potentials for ruthenium within the *COMPASS* force field. We therefore approximate the catalyst molecule by replacing the actual pendant group with a CH_2 group. This reduces the number of atoms in the simulation and parameters for the atoms in the ethene molecule are readily availability in the *COMPASS* force field. This simplification of the catalyst is justifiable given the steric search criteria we implemented in our MC scheme.

The first ROMP reaction between the ethene and a DCPD molecule creates two reaction centers that can independently propagate, effectively each CH_2 in the ethene molecule behaves like a full molecule of Grubb's catalyst. The reactions in our code solely depend on a steric factor and therefore our choice of an ethene molecule, though not completely realistic, still recreates the ROMP mechanism. 390 DCPD molecules along with 10 ethene molecules were tiled into a cubic box on a simple cubic lattice randomly to get a density of 0.7 g/cc. Each sample was then equilibrated for 25ps under isotropic NPT conditions P = 10 atm, T = 300 K and the time step is 2.0fs. Time step integration was done using a 4th order rRESPA algorithm [10] where the bond and dihedral interactions were integrated eight times, improper interactions four times, pair interactions two times, and the long range coulomb interactions integrated once per time-step. Simulations were done using a Nose-Hoover barostat with pressure relaxation time of 1ps and Langevin thermostat with temperature relaxation time of 0.1ps to obtain the initial simulation box to begin the ROMP reaction process. The equilibrium density of the DCPD and ethene mixture is 0.92 g/cc which is close to the pure DCPD density at ambient conditions ~1.0 g/cc. Simulations with pure DCPD show density of 0.97 g/cc. After the above equilibration of the DCPD and ethene mixture to generate the initial randomized simulation box we loop through a series of 3 steps to achieve network formation as follows.

1. A 1.0ps MD simulation under NPT conditions P = 1.0 Atm, T = 300 K with a time step of 1.0fs integrated using the same 4th order rRESPA algorithm as the equilibration of the ethene and DCPD mixture as described above. The simulation

is run with Nose-Hoover barostat with pressure relaxation time of 1.0ps and Langevin thermostat with temperature relaxation time of 0.1ps simulations

2. Each 1.0ps MD simulation is followed by an offline reaction step. The reaction step consists of checking distance of each unreacted DCPD double bond with all the dangling Ruthenium attached via double bonds to the extremities of polymeric chains. In the reaction process all pairs of double bonds are swapped if the reaction steric criterion as shown in Figure 4.2 is met where $R_c = 6.0$ Å. The bond-swapping algorithm chooses randomly 10% of possible swap sites that meet the steric criteria to implement the reaction step. We only allow up to a maximum of 10 bond exchanges per reaction step to cap excessive reactions occurring in the initial stages of the network evolution. After the bonds are swapped all angular, dihedral and improper interactions are updated to reflect the change in topology. And the new updated topology is then submitted to the energy minimization in step 3
3. The highly non-equilibrium state of the bond, angular, dihedral and improper interactions is ameliorated using conjugate gradient energy minimization, which is terminated when $\Delta E/E < 10^{-5}$ to ensure stabilization of the structure. The new energy minimized structure is then subjected to step 1 for further annealing to get better global structures and facilitate new encounters of reactive sites.

We continue with steps 1, 2 and 3 until reactions plateau off. This procedure requires exponentially larger amounts of time for same number of reactions as the reaction progresses. During this process we capture ensembles at differing degrees of reaction and subject them to mechanical test as discussed in Section 4. The reaction proximity criterion was chosen based on the inter-molecular peak in the RDF that corresponds to sp_2 carbon-carbon distance in pure DCPD, which is at 4.0 Å. We therefore chose the cutoff of 6.0 Å for reaction that corresponds to an average distance of 4.2 Å between double bonded carbons on adjacent molecules undergoing reactions (details in caption of Figure 4.2). This value is calculated by assuming the sp_2 carbons undergoing ROMP on the separate molecules are equidistant from their counterparts in the other molecule as is explained graphically in Figure 4.2.

With the reaction criteria described above, we obtained a maximum degree of reaction of 60%, as defined by the percentage of DCPD double bonds that underwent ROMP reaction. Changing the reaction cut-off to R_c = 6.5Å a maximum degree of reaction of 76% could be achieved in 2 of our 4 independent samples. Since there is no biasing of ROMP reaction on the two DCPD double bonds, therefore both norborene and cyclopentene sites react with equal probably. Four independent samples at each degree of reaction were created. A typical reaction run needed about 4.5 million MD time steps and took 400 hours on 4 CPUs of the dual CPU Apple G5 Xserve cluster at CAC.

4.3.1 Reaction Kinetics

Figure 4.3a shows the degree of reaction (α) with time of a typical simulation. The line is the best fit to eqn(4.19).

$$\alpha = 1 - \psi \exp(-t/\tau_1) - \zeta \exp(-t/\tau_2) \qquad (4.19)$$

Where $\psi = 0.477$, $\zeta = 0.481$, $\tau_1 = 17.065$ ns and $\tau_2 = 0.374$ ns. Two superimposed first-order processes seem to fit the overall reaction behavior. It reflects of a fast initial reaction when the diffusion of catalysts to the reaction sites is unhindered by the presence of the backbone networks. At large reaction times the availability of the catalyst and reactive double bond sites is more rare and is manifest in the large time constant τ_1.

Figure 4.3b shows the fraction of different species that exist at any given degree of reaction. The monomers are shown as the Q_0 i.e. monomers with no bonds, the Q_1 and Q_3 are monomers that are connected to catalysts and Q_2 are molecules that have two bonds to other monomers and Q_4 are molecules that are cross-linked. As can be seen the concentration of the Q_2 species goes through a maximum at a degree of reaction of about 0.5 and the concentration of monomers is monotonically decreasing as they are consumed by reactions. The concentration of Q_4 monotonically increases due to the consumption of Q_2 monomers. As is implicit from the ROMP mechanism the sum of the fraction of Q_1 monomers and Q_3 monomers is a constant equal to the fraction of catalyst particles in the simulation.

4.4 Structural Characterization of DCPD Network

In this section we explore the structural evolution of the DCPD network due to the ROMP reaction. In Section 4.4.1 the radial distributions of the center of mass of the DCPD molecule at different degrees of reaction, in Section 4.4.2 the bond angle distributions, and in Section 4.4.3 the changes in the dihedral angle distributions with reaction are discussed.

4.4.1 Pair Correlation Functions of DCPD Centers of Mass

Figure 4.4 shows the pair correlation functions (PCF) of the center of mass of DCPD as a function of the degree of reaction. As can be seen in the figure the peak positions do not shift significantly as the degree of reaction varies. This is a manifestation of the fact that the density of the evolving network is more or less constant at about 1.00 g/cc. This implies that conventional powder XRD studies to investigate the structure of DCPD networks will not be sensitive enough to discern the reaction signature.

4.4.2 Bond Angle Distribution Functions

Figure 4.5 shows the bond angle distribution functions associated with some relevant bonding configurations at 3 different degrees of reaction, 1%, 30%, and 70%. $C1_{sp3}$ is the sp_3 hybridized carbon with one hydrogen attached, $C2_{sp3}$ is the sp_3 hybridized carbon with two hydrogen attached and C_{sp2} is the double bonded carbon. For example in Figure 4.5a the bond angle distribution function is for the angle between atom types $C1_{sp3}$-C_{sp2}=C_{sp2}, with C_{sp2} in the center, which is expected to be 120^o according to its hybridization state. As we can see, the distribution shows at 1% degree of reaction a) one peak at 108^o and b) a shoulder at 115^o. The former is due to the strain in the norborene ring and the latter is indicative of the lesser strain of the cyclopentene ring. On the other hand we can see in Figure 4.5b that $C2_{sp3}$-C_{sp2}-C_{sp2} does not show two peaks because the molecule only contains one such angle on the cyclopentene ring and the peak is at 113^o at 1% degree of reaction. Therefore comparing Figure 4.5a and Figure 4.5b confirms that the norborene ring is more strained than the cyclopentene ring. After reaction, however, both $C1_{sp3}$-C_{sp2}-C_{sp2} and $C2_{sp3}$-C_{sp2}-C_{sp2} relax to their equilibrium values of 125^o which the set C=C-C equilibrium angle value of $\sim 125^o$ in our simulations as can be seen in COMPASS potential parameters in Appendix A. Other bond angle distribution functions also provide clues, based on how they evolve at different degrees of reaction. For example, changes in the distribution of angles centered on the double bonded carbons are indicative of the ring strain relaxation due to the ROMP reaction.

4.4.3 Dihedral Angle Distribution Function

Figure 4.6 shows the dihedral angle distribution of selected configurations around the C=C double bond. The DCPD molecules consists of only *cis* configurations around its double bonds since the dihedral angles are all centered around 0^{o}. However as the ROMP reaction takes place the resultant C=C configurations that appears are *cis* and *trans* with equal probability. This feature can be easily seen from Figure 4.6 a, b, and c. The appearance of the peaks around 180^{o} is the signature of the trans conformation. The area under each curve around a particular angle yields the fraction of structural units in the corresponding conformation. Accordingly, for a degree of reaction of 0.7, half of the reacted C=C groups are found in *trans* and the other half in *cis* conformation. This effect is a consequence of the fact that the reaction algorithm does not discriminate between the *cis* and *trans* conformations. The effect of selecting only *trans* configurations as is the case with ROMP catalysis with first generation catalyst is an area that needs further investigation. We believe that the mechanical properties of networks do not significantly depend on the proportions of *cis* and *trans*, as both configurations are likely to respond similarly to applied stresses.

4.5 Mechanical Properties

In this section we discuss the mechanical testing procedure to calculate the Young's modulus, Poisson's ratio and Bulk modulus of the networks generated above.

4.5.1 Calculation of the Young's Modulus and Poisson's Ratio

Measurement of Young's modulus (E) was done using the following procedure. Each simulation box was equilibrated for 1000ps anisotropically i.e. box dimensions in the x,y,z direction are independently controlled to modulate pressure. Simulations were carried out with a time step of 1.0fs integrated using the 4th order rRESPA algorithm, as described in section 4.3 during network generation. The Nose-Hoover barostat with a pressure relaxation time of 1.0ps combined with the Langevin thermostat with a temperature relaxation time of 0.1ps were used for creating NPT conditions $P_{xx} = P_{zz} = 10$ Atm, $P_{yy} = 10$ Atm and T = 300K . At the end of this equilibration the NPT conditions were switched to $P_{xx} = P_{zz} = 10$ Atm, T = 300K and the y-axis pressure control was switched off. The y-axis was then linearly strained by ±5% in two separate runs of 10ps each. The two resultant strained boxes were equilibrated for 1000ps at the final strained state. The Young's modulus was calculated by the ratio of differences in stresses $\sigma_{yy}(-5\%)$, $\sigma_{yy}(+5\%)$ and strain according to

$$E = \frac{\Delta\sigma_{yy}}{\Delta\varepsilon_y}, \tag{4.20}$$

where $\Delta\varepsilon_y$ is the change in tensile strain.

$$\varepsilon_y = \lambda_y - 1 \tag{4.21}$$

Using eqn(4.21), we can reframe eqn(4.20) as

$$E = \frac{\sigma_{yy}^{+} - \sigma_{yy}^{-}}{\left(\lambda_y^{+} - \lambda_y^{-}\right)}, \tag{4.22}$$

where σ_{yy}^{+} is the equilibrium normal stress in y-direction after tension (+5% strain), σ_{yy}^{-} is the one after compression (-5% strain) and λ_y^{+}, λ_y^{-} are the *y* dimension extension ratios of the simulation box under tension and compression respectively. The equilibrium stress σ_{yy}^{+} and σ_{yy}^{-} is calculated as the average over the final 100ps of 1000ps equilibration runs. The extension and compression stress in *y*-direction can be obtained from the average values of the dashed and dotted lines in Figure 4.10 respectively for various degrees of reaction.

The Poisson's ratio, *v*, is also calculated by using equilibrium values of the other box dimensions that are relaxing due to the applied *y* direction strains. We note that at low degrees of reaction the box is quite fluid and fluctuations in extension ratios of the other box dimensions sometimes lead to spurious results in the Poisson's ratio. When this occurs we check the volume of the simulation box to see if there is any significant density change during the process of tension and compression. A negligible density change implies a Poisson's ratio of 0.5 and this value is then used instead of the value calculated by

$$\upsilon = -\frac{\Delta\varepsilon_T}{\Delta\varepsilon_y}, \tag{4.23}$$

Where ε_T is the transverse strain for the tensile strain ε_Y. Using eqn(4.21) we can then reframe Poisson's ratio as

$$\upsilon = -\frac{\left(\lambda_T^{+} - \lambda_T^{-}\right)}{\left(\lambda_y^{+} - \lambda_y^{-}\right)} \tag{4.24}$$

Where $\lambda_T^{+} = \sqrt{A_{xz}^{+}/A_{xz}^{o}}$, $\lambda_T^{-} = \sqrt{A_{xz}^{-}/A_{xz}^{o}}$, where $A_{xz}^{o}, A_{xz}^{-}, A_{xz}^{+}$ are the area's of the zx plane of simulation box at neutral, tensile and compressive strains respectively. The equilibrium extension ratios λ_T^{+} and λ_T^{-} are calculated from the average values of the areas calculated over the final 10 ps of 1000 ps equilibration runs at extension and compression respectively, which can be obtained from the dashed and dotted lines plotted in Figure 4.13 respectively for various α.

4.5.1.1 Young's Modulus

Figure 4.7 shows the Young's modulus with respect to the degree of reaction. We can see that the mechanical percolation of the system occurs at a degree of reaction around 0.24-0.3. After this percolation threshold we find a monotonic increase in the Young's modulus.

4.5.1.2 Poisson's Ratio

Figure 4.8 shows the evolution of the Poisson's ratio as a function of the degree of reaction. As can seen the Poisson's ratio is approximately equal to 0.5 until percolation occurs at degree of reaction ~0.3 and then starts decreasing monotonically.

4.5.2 Calculation of Bulk modulus

The bulk modulus (***K***) is calculated using the following procedure. We first equilibrate a simulation box by subjecting it to the Nose Hoover NPT ensemble with one degree of freedom, i.e., the dimensions of the box in the x, y and z dimensions are coupled to modulate hydrostatic pressure such that a compressive pressure of 10 atmospheres and a temperature of 300 K is maintained. We allow equilibration for 100 *ps* using a time-step of 1.0fs using the same 4th order rRESPA integrator as described in the preceding Section 4.5.1 for the Young's modulus. A pressure relaxation time of 100 fs and a temperature relaxation time of 10 fs were used.

After this equilibration step the box was then subjected to a NVT ensemble with T = 300K and further relaxed for 50 ps to get the initial box using a temperature relaxation time of 10 fs. The box was then linearly strained in all 3 dimensions by 1% in expansion and compression in 1 ps the strained simulation box is then allowed to equilibrate for 50ps under NVT conditions. The equilibrium values for pressure and volume are recorded by averaging the pressure and volume of the strained simulation box in the final 10ps of the 50ps equilibration run. The bulk modulus can then be calculated from eqn(4.25)

$$K = -V\frac{dP}{dV} \tag{4.25}$$

this can be reframed as shown below.

$$K = -\frac{P^{+} - P^{-}}{\left(V^{+} - V^{-}\right)/\left(\left(V^{+} + V^{-}\right)/2\right)} \tag{4.26}$$

Where P^{+} and P^{-} are the equilibrium hydrodynamic pressures at extension and compression and V^{+} and V^{-} are the equilibrium volume at extension and compression respectively.

4.5.2.1 Bulk modulus

Figure 4.9 shows the evolution of the bulk modulus of the system as a function of the degree of reaction. As expected, the bulk modulus increases monotonically with the degree of reaction as the network gains the connections. However, there is no distinct threshold as is seen in the Young's modulus data.

4.6 Network Behavior with Applied Strain

In this section we compare the behavior of the relaxed network against its behavior after applied compression and tension during mechanical tests. Please note that all solid lines represent the behavior of the unstrained configuration, dashed lines that at a positive strain of +5% (extension in the y dimension) and dotted lines that at a negative strain of 5% (compression in the y dimension).

4.6.1 Stress

In Figure 4.11 we plot for various degrees of reaction the evolution of the normal stress in y-direction (σ_{yy}) as a function of time in response to applied strains, i.e., after the simulation box was abruptly lengthened or shortened in the y-direction. We find that a noticeable stress response is only observed above a threshold of about 30% degree of cure. We use the stress response of the simulation boxes at different degrees of reaction in our calculation of the Young's modulus as is explained in section 4.5.1

4.6.2 Internal Energy

Figure 4.11 shows the equilibrium values of internal energy change due to applied strain. We can see that there is only a small internal energy shift due to deformation for degrees of reaction of less than 40%. This implies that observed modulus is dominated by entropic effects and internal energy change only plays a role at high degrees of reaction. A simple calculation of expected internal energy change due to strain can be calculated by

$$\Delta \mathrm{E}_{deform} = \int_0^{\varepsilon_x} \frac{\sigma_{xx} d\varepsilon_x}{\rho_N} + \int_0^{\varepsilon_y} \frac{\sigma_{yy} d\varepsilon_y}{\rho_N} + \int_0^{\varepsilon_z} \frac{\sigma_{zz} d\varepsilon_z}{\rho_N} \tag{4.27}$$

We can arrive at an approximate value of the potential energy change with deformation if we assume that 1) the stress σ_{yy} is a linear function of ε_y 2) stress σ_{xx} and σ_{zz} is maintained at 10 atm and 3) neglect atomic number density (ρ_N) changes during deformation. We can then rewrite eqn(4.27) as

$$\Delta \mathrm{E}_{deform} = \frac{(\sigma^o_{xx} + \sigma^o_{zz})\varepsilon_t + (\sigma^o_{yy} + \sigma^f_{yy})\varepsilon_y /2}{\rho_N} \tag{4.28}$$

Where ε_y is the applied maximum y strain, ε_t is the resultant transverse strain. σ_x^o σ_y^o σ_z^o is the initial stress in x y and z direction respectively and σ_y^f is the final y stress after strain.

Consider the case of DCPD at a degree of reaction $\alpha = 0.4$. We can see from Figure 4.10 that the final stress after 5% tensile strain is σ_y^f ~250 Atm. Using this value in eqn(4.28) gives us a ΔE_{deform} ~ 1 cal/mol. This energy difference is difficult to delineate from the thermal noise. Despite careful averaging of our data we could show no such systematic increase in comparison to values from the unstrained state. This however is inadequate proof of entropic effects we therefore based our conclusions by observing the change in density on deformation in the section below. This is analogous to our argument in Chapter 3 Section 3.5 where we show proof of entropic restoration from a strained state.

4.6.3 Density

Figure 4.12 shows the density evolution with time of equilibration at neutral, 5% tensile strain and 5% compression strain in the last 0.4 ns of the 1 ns equilibration. The average density of networks with degree of reaction of less than 40% is generally constant within thermal fluctuations upon deformation. This implies that the Poisson's ratio is equal to 0.5 for ensembles with low degree of reaction < 40 % since the volume does not change. The threshold is significant since it marks the end of rubbery elasticity. Unlike the difficulty in discerning change in energy during deformation the density change is much easier to see. We can intuitively understand that a density change is necessarily indicative of potential energy change since it means that relative position of atoms changes which causes a change in potential energy or in our case where the temperature is controlled, a change in total energy.

4.6.4 Simulation Box Behavior

Figure 4.13 shows how the other two dimension of simulation box behave after the applied strain as evidenced by the cross section area A_{xz}. We use the cross sectional area behavior in our calculation of the Poisson's ratio as is mentioned in section 4.5.1

4.7 Conclusions

We describe a novel reactive MD simulation method capable of creating amorphous networks. Using this methodology we were capable of generating organic molecular networks in which the chemistry of the constituent reactions is known and can be applied to systems such as epoxies and other condensation polymers that crosslink. The all-atomistic DCPD networks can now be used for a variety of tests such as diffusion of small molecules, heat transfer coefficients and other transport properties.

The ROMP reaction of DCPD is capped at a degree of reaction of about 0.7. In our reaction process the reaction of DCPD via ROMP causes rearrangement of double bonds and associated dihedrals and after reaction, we show the formation of *trans* compounds around double bonds when initially only *cis* configuration exist in pure DCPD. First order kinetics explain the reaction process and is broadly similar to results obtained from experiment.

As discussed in Chapter 3 there are 3 distinct stages of cure delimited by two thresholds the Young's modulus threshold α_Y occurs at degree of reaction ~0.3 and the

Poisson's ratio threshold α_P occurs at degree of reaction ~0.4, based on our best estimates. These values compare very well with the same thresholds for ROMP networks with angular constraints where these values are 0.3 and 0.4 respectively. Based on these thresholds we can then state that the networks are fluid like at degrees of reaction < 0.3 and rubber like at degrees of reaction between 0.3-0.4 and glass like at degrees of reaction > 0.4.

Fundamentally there needs to be an effort to calculate the values of these thresholds in a general case. The values of the Young's or Shear modulus between α_Y and α_P is proportional to temperature, whereas above α_P these moduli are inversely proportional due to softening of molecular force factors with increase in temperature.

There has been inadequate attention paid to entropic effects of elastic properties of network polymer with the degree of cure. We show here evidence of such effects at different thresholds. These effects are fundamental to the understanding and design of molecular networks and their applications.

4.8 Figures

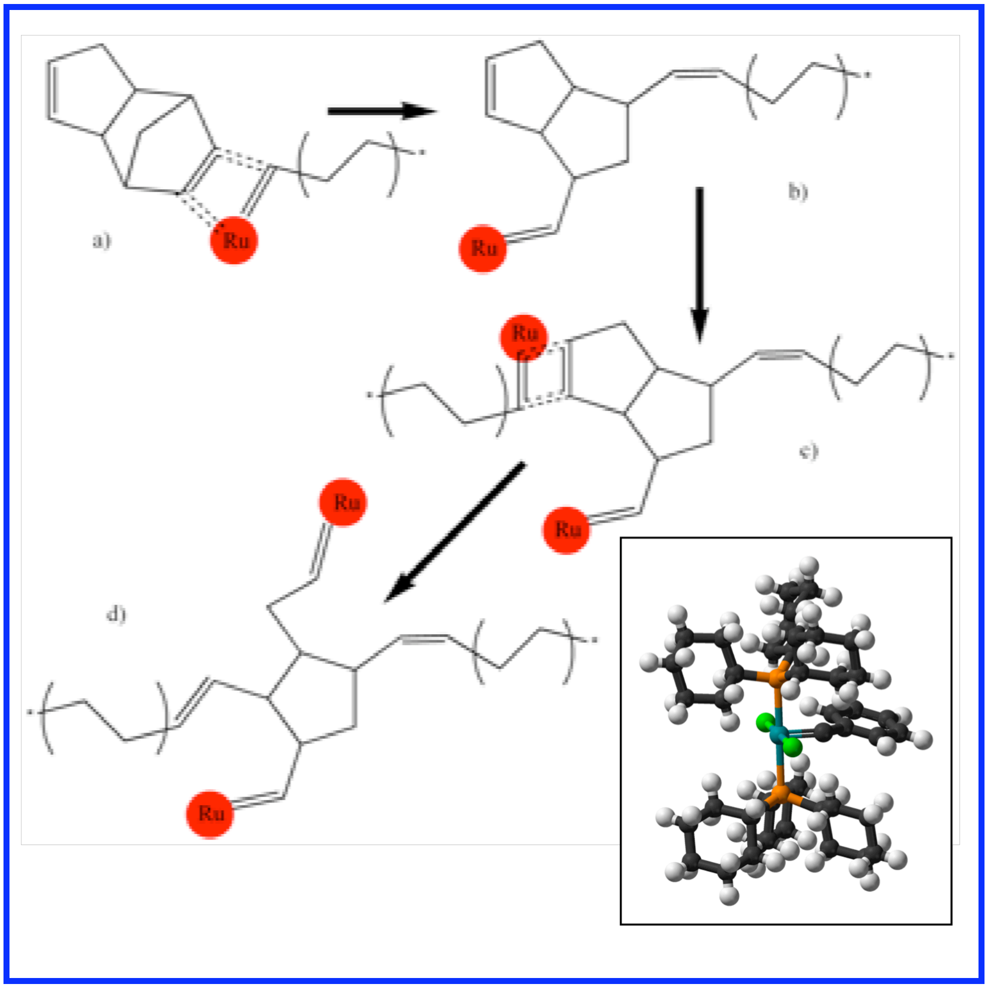

Figure 4.1: ROMP of DCPD reaction. In our simulations the Ruthenium based ligand shown in red is replaced by a CH_2 group. This group is then artificially used as the living tip catalyst that traces the network backbone. The actual catalyst molecule is shown in the inset (Ruthenium is the blue atom) a) shows the attack of catalyst on norborene double bond, b) shows configuration after ring strain release c) shows attack of catalyst on cyclopentene ring and d) shows configuration after cyclopentene ring strain relaxation.

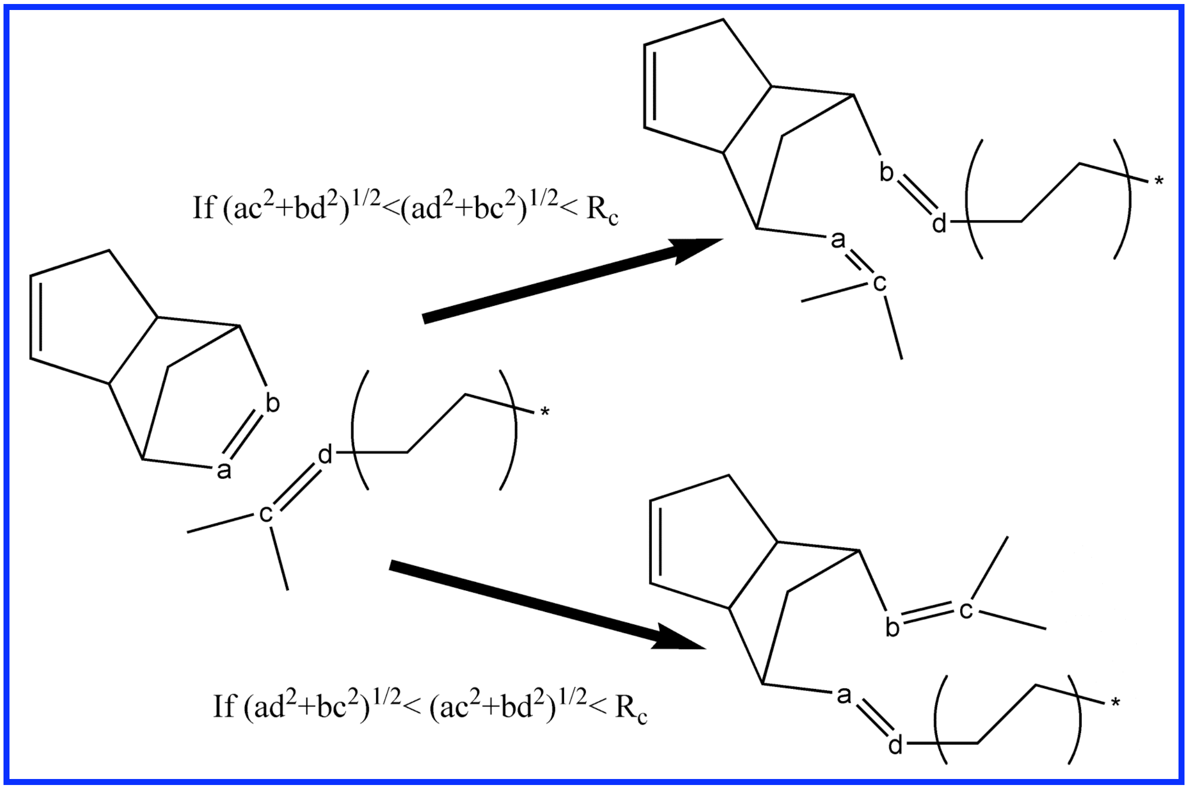

Figure 4.2: DCPD ROMP reaction steric criterion. The proximity criteria allows reaction as shown in the diagram above where R_c = 6.0Å. The reaction proximity criteria used is chosen so that the maximum degree of reaction (α) ~ 0.7. Alternatively choosing R_c = 5.5Å capped reactions to α~0.4 which is too low. Higher values of R_c such as R_c = 7.0Å resulted in higher α but the resultant networks had high internal strain. The RDF of sp_2C shows an intermolecular peak at 4.0Å. If we assume ac = bd (or bc = ad in the other case) then R_c = 6.0 implies ac = bd = 4.2Å. This is slightly larger than the intermolecular peak distance and enables a fast reaction rate. Reaction rate drop considerably as we reduce R_c value.

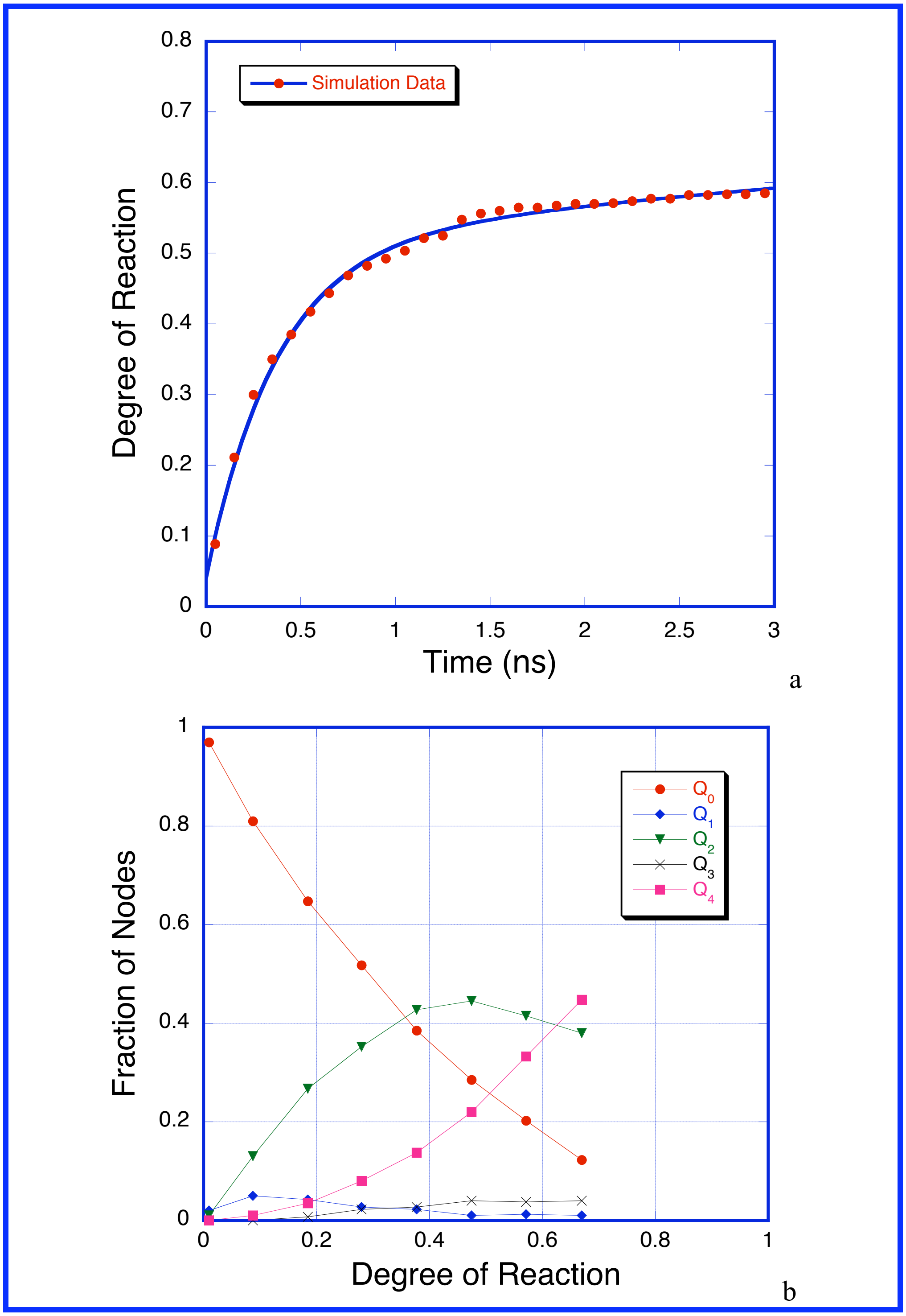

Figure 4.3: Kinetics of atomistic simulations a) degree of reaction vs. time b) component fraction vs. degree of reaction

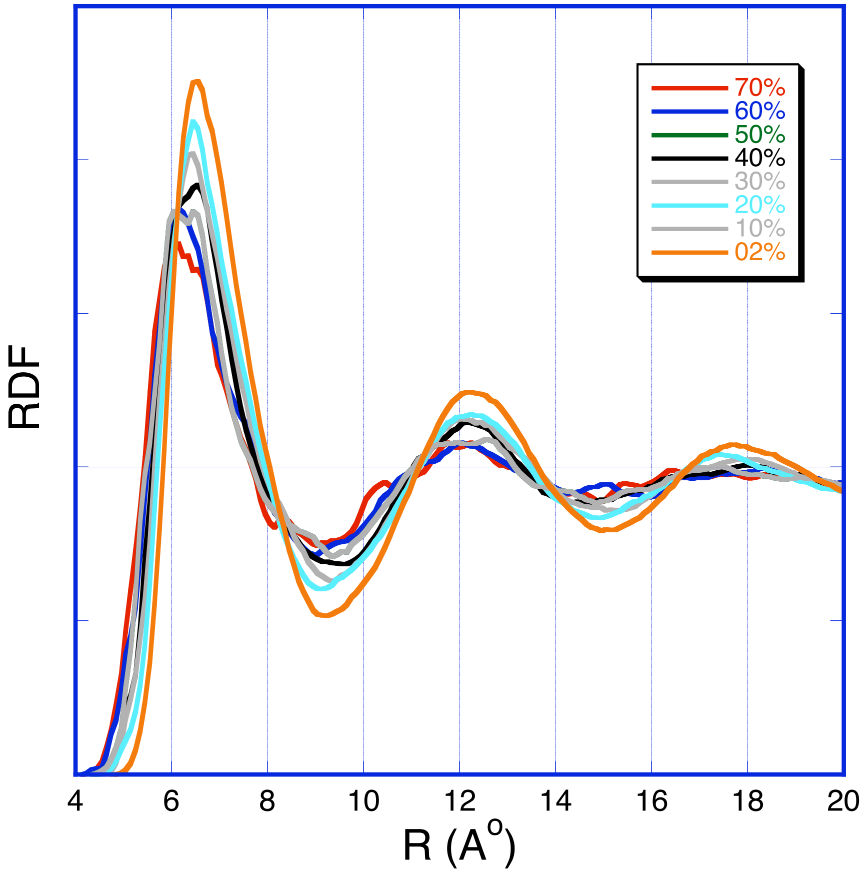

Figure 4.4: Pair correlation functions of the centers of mass of the reacting DCPD system for different degrees of reaction. We note that these correlations functions do not significantly differ as the reaction progresses. This is reflected in the relatively constant density of network during ROMP of DCPD.

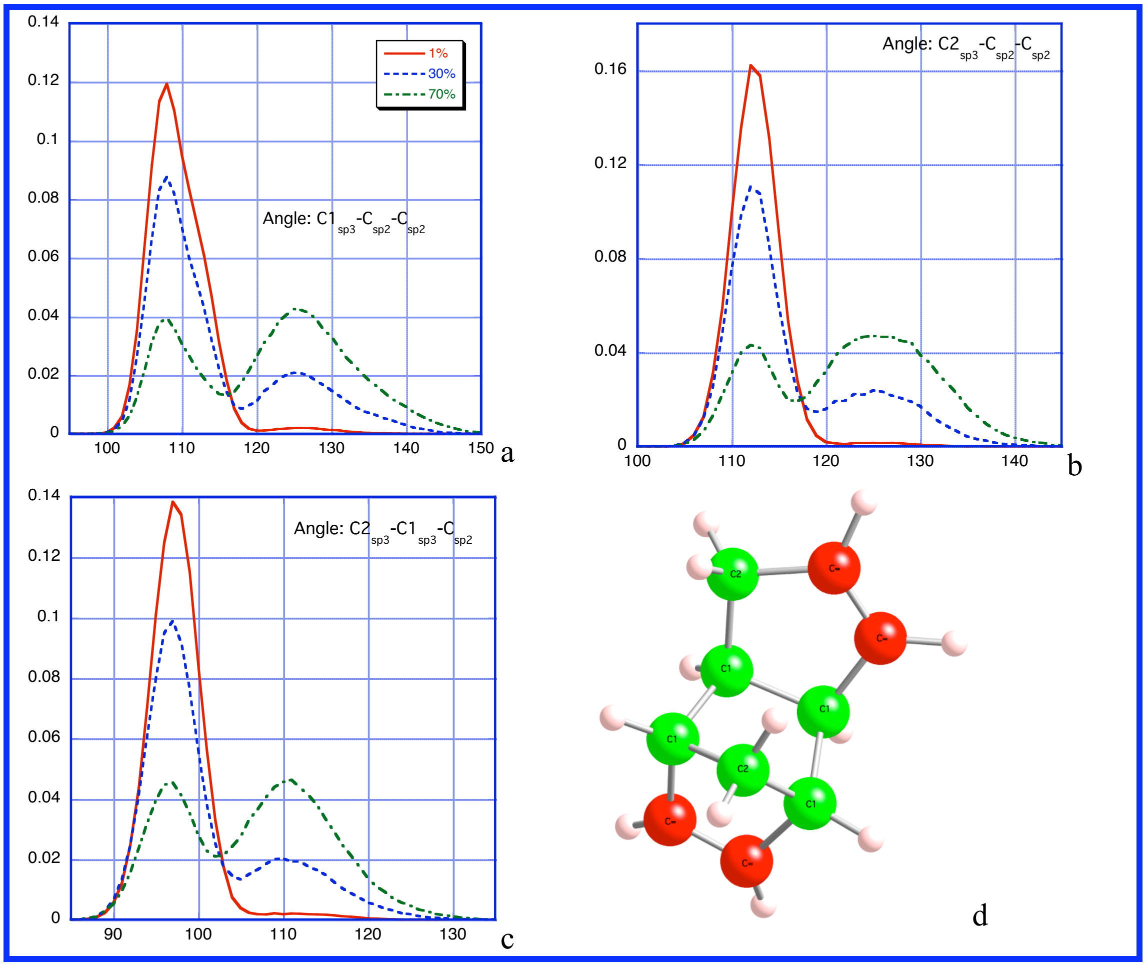

Figure 4.5: Bond angle distribution functions of selected angles (α=1%, 30%, and 70%) that change significantly after the ROMP of the norborene or cyclopentene double bond. a) C1-sp$_2$C-sp$_2$C: there are 3 such angles, the shoulder at 115^{o} is due to the angle on the cyclopentene. b) C2-sp$_2$C-sp$_2$C: only 1 such angle in DCPD c) C2-C1-sp$_2$C: only one such angle in DCPD. d) key for part a b and c: The red atoms are sp$_2$ carbon. The bottom double bond is on the norborene ring and the top double bond is on the cyclopentene ring. The sp$_3$C1 is a carbon with one hydrogen attached and sp$_3$C2 is a carbon with two hydrogen attached. This key is also used in Figure 4.6. he effect of ROMP reaction on norborene is seen in plot (a) and (c), and effect of ROMP on cyclopentene is seen in plots (a) and (b). The evolution of peaks reflects generation of equilibrium values of respective angles due to ring strain release.

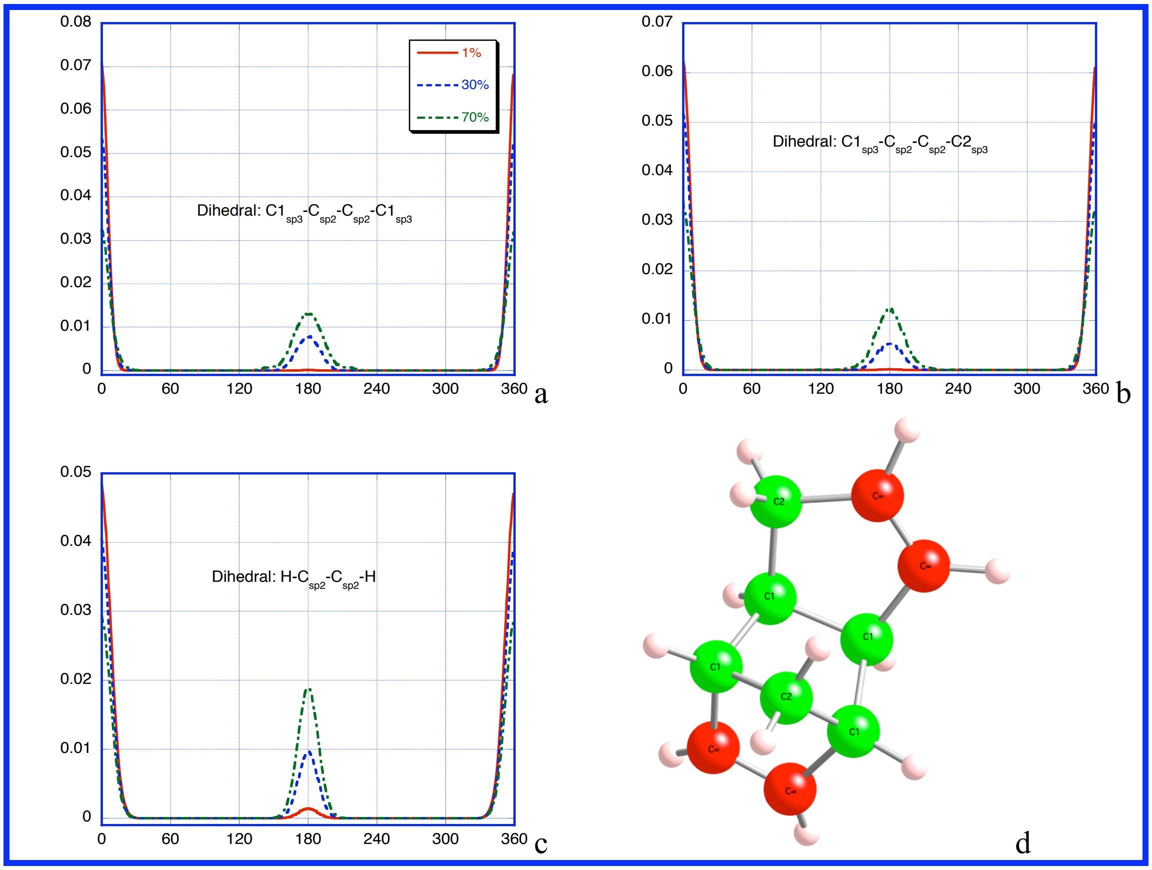

Figure 4.6: Dihedral angle distribution of groups around C=C double bond showing transformations due to the effect of the ROMP reaction. Especially important are the part a) C1-sp$_2$C=sp$_2$C-C1: one such dihedral in DCPD on norborene ring b) C1-sp$_2$C=sp$_2$C-C2: one such dihedral on cyclopentene ring and c) H-sp$_2$C=sp$_2$C-H: 2 dihedrals one on norborene and one on cyclopentene ring that are dihedrals where the C=C is the central. Pure DCPD is 100% *cis* configuration as can be seen from the DCPD molecule. As the system undergoes ROMP the peaks appear at 180^{o} that is the signature of the trans configuration. The reaction process converts the initial *cis* configuration to *trans* configuration with 50% probability.

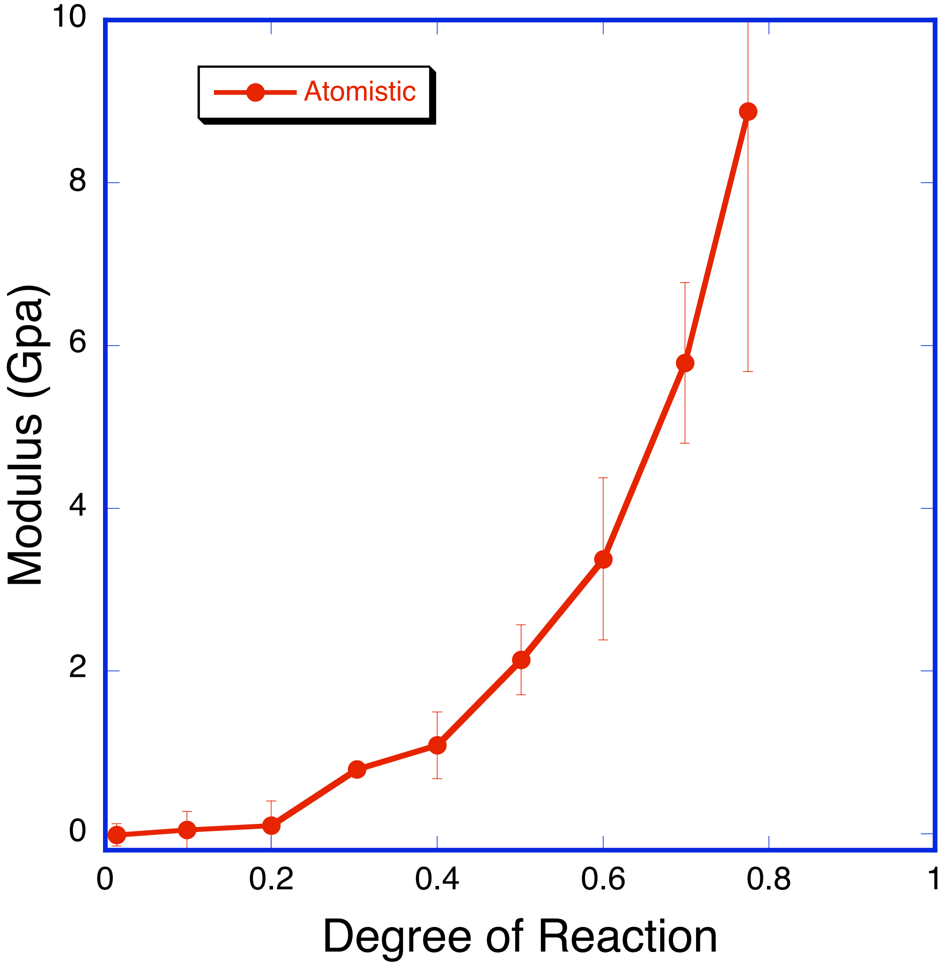

Figure 4.7: Young's modulus for atomistic simulations. We note that the Young's modulus threshold α_P is somewhere between 0.20-0.30.

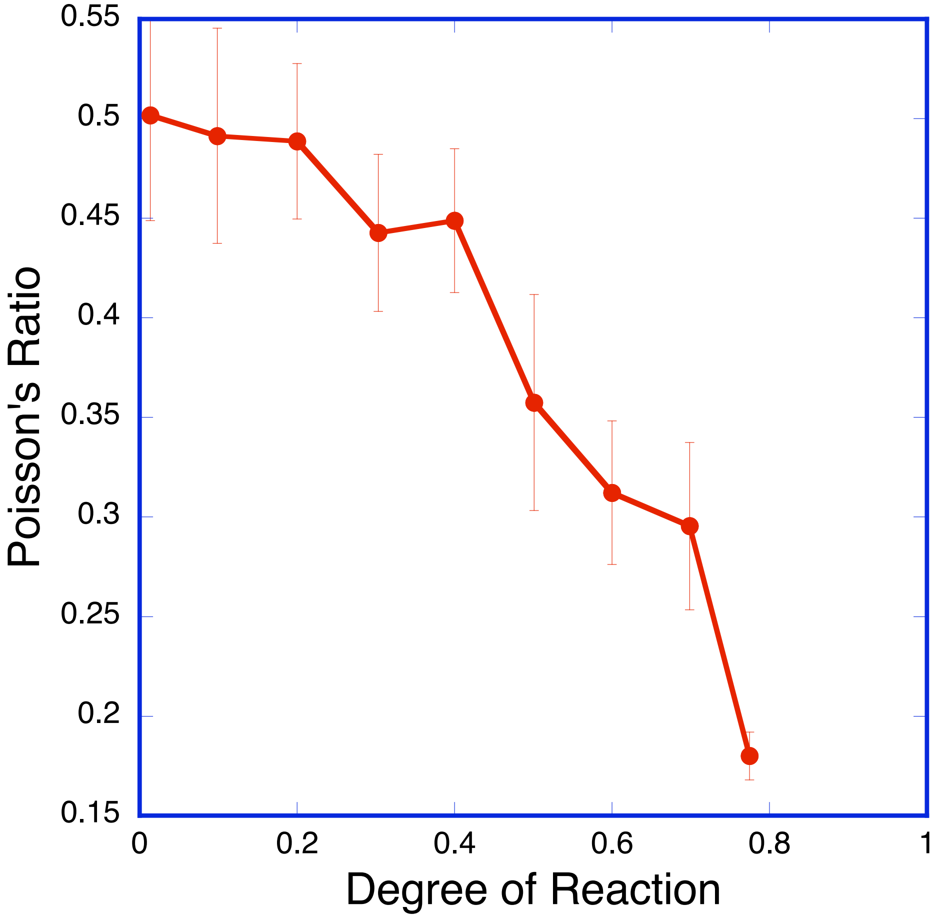

Figure 4.8: Poisson's ratio for atomistic simulations. The Poisson's ratio threshold is difficult to predict due to the noise and probably appears at degree of reaction ~0.4 as can be confirmed from absence of change in internal energy and negligible density change up to this limit from Figure 4.11.and 4.12 respectively.

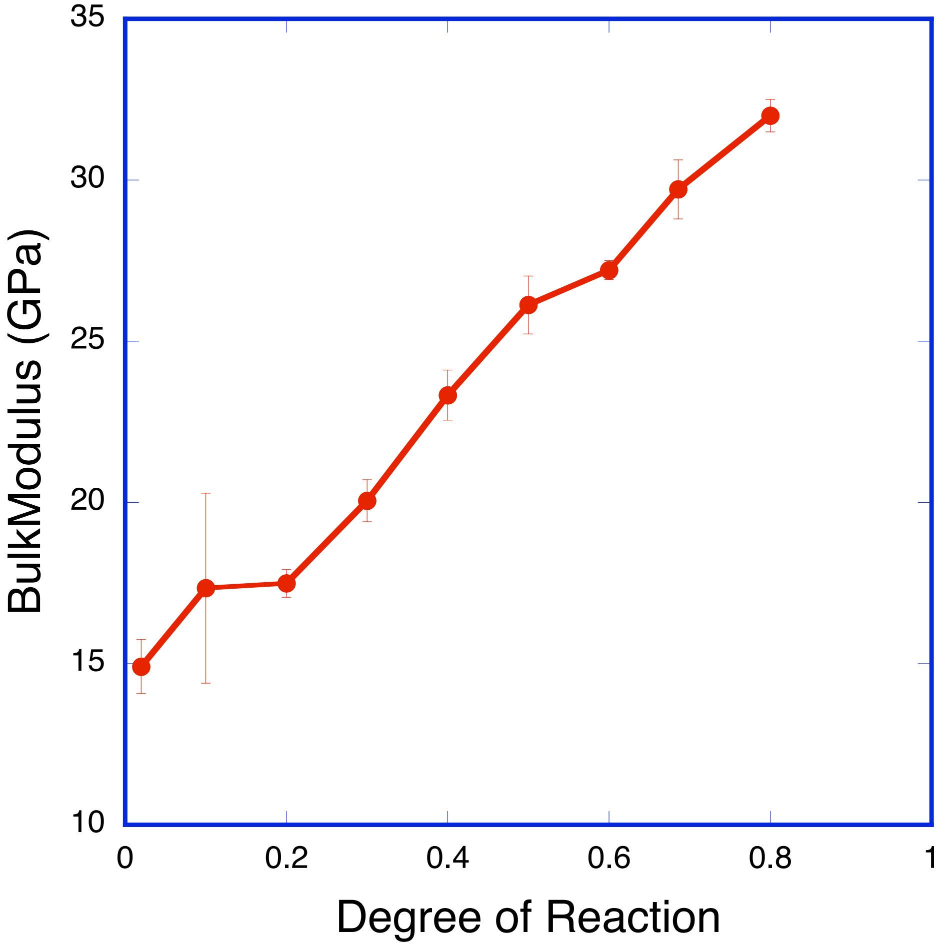

Figure 4.9: Bulk modulus of atomistic simulations versus α. The modulus exhibits linearity with α and does not seem to show characteristic thresholds apparent in the Young's modulus plot or the Poisson's ratio plot.

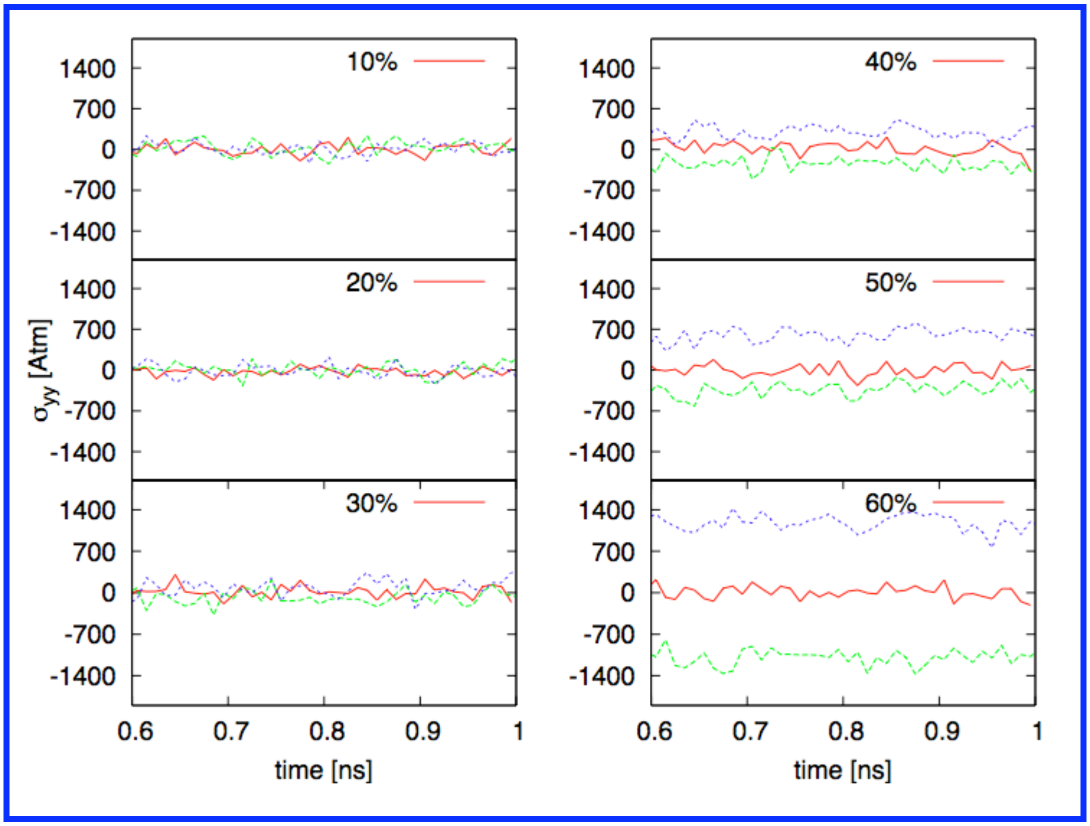

Figure 4.10: Behavior of stress σ_{yy} (atmospheres) versus time for the last 0.4 ns of equilibration for 3 strained states a) neutral in solid red line b) 5% uniaxial extension by dashed green line c) 5% uniaxial compression by dotted blue line. Each sub graph is plotted at different α as shown in their respective titles (10%, 20%, 30 %, 40%, 50% and 60%). Significant differences in σ_{yy} due to deformation is apparent at α = 40% and there is evidence of the same at α=30%. This implies that there is a modulus for networks α ~0.30.

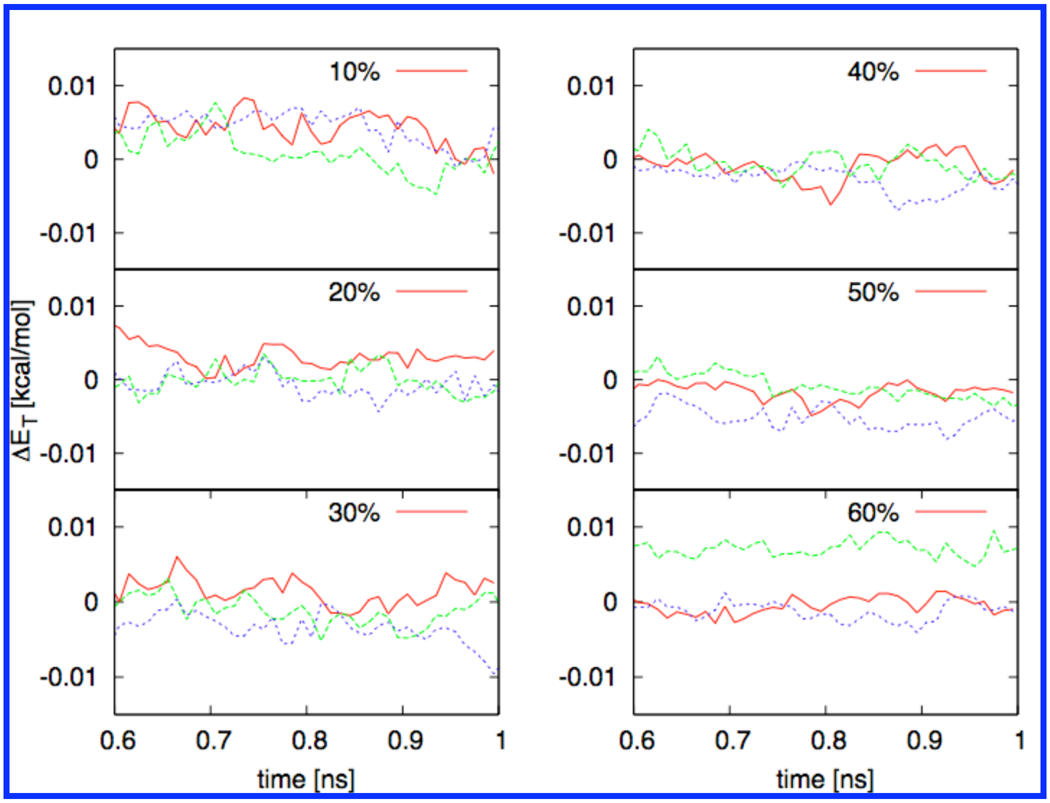

Figure 4.11: Behavior of internal energy ΔE $(kcal/mol)$ versus time (ns) for the last 0.4ns of the 1ns equilibration for 3 strain states a) neutral in solid red line b) 5% uniaxial extension by dashed green line c) 5% uniaxial compression by dotted blue line. Each sub graph is plotted at different α as shown in their title (10%, 20%, 30 %, 40%, 50% and 60%). We note that the change in internal energy is negligible for degree of reaction < 40%. This implies that the Young's modulus is entropic until this limit.

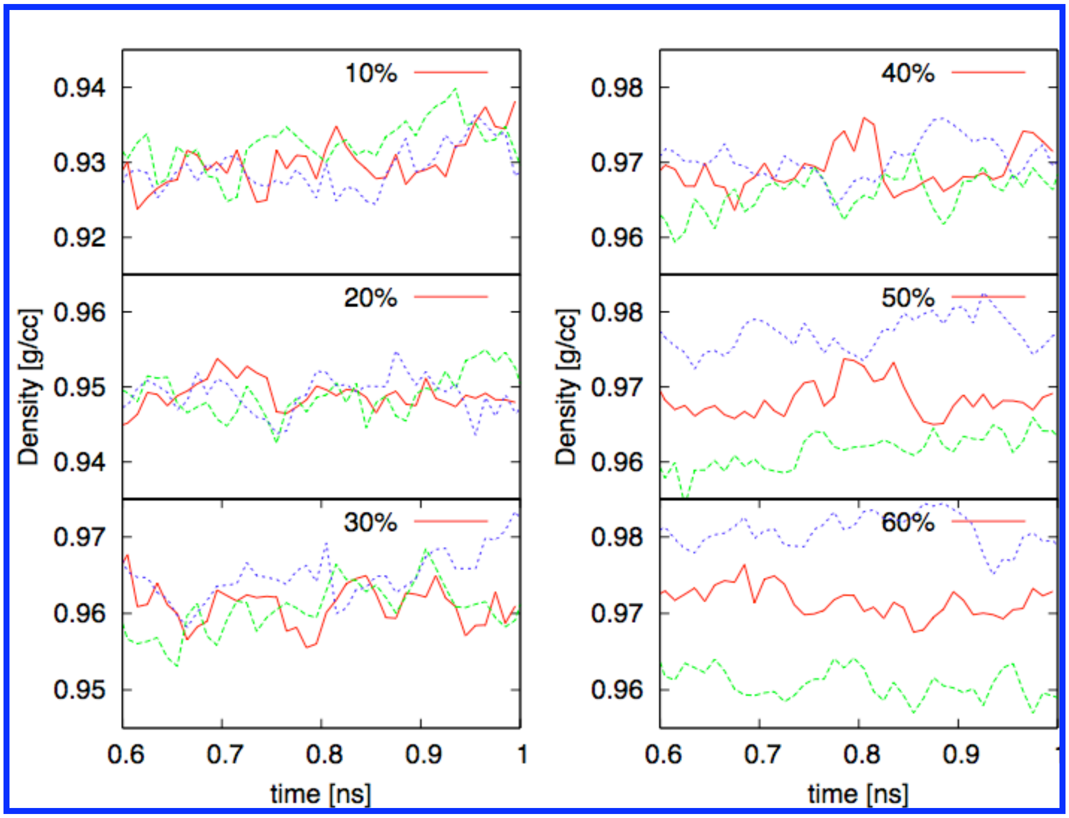

Figure 4.12: Behavior of density ρ(g/cc) versus time for the last 0.4ns of the 1.0ns equilibration for 3 strained states a) neutral in solid red line b) 5% uniaxial extension by dashed green line c) 5% uniaxial compression by dotted blue line. Each sub graph is plotted at different α as shown in their respective titles (10%, 20%, 30 %, 40%, 50% and 60%). Significant differences in density due to deformation is apparent at α = 50%. We note that the density of the system is conserved for degrees of reaction ≤40%. This leads us to believe that the response is enthalpic after threshold of $\alpha_P=\alpha\sim0.40$.

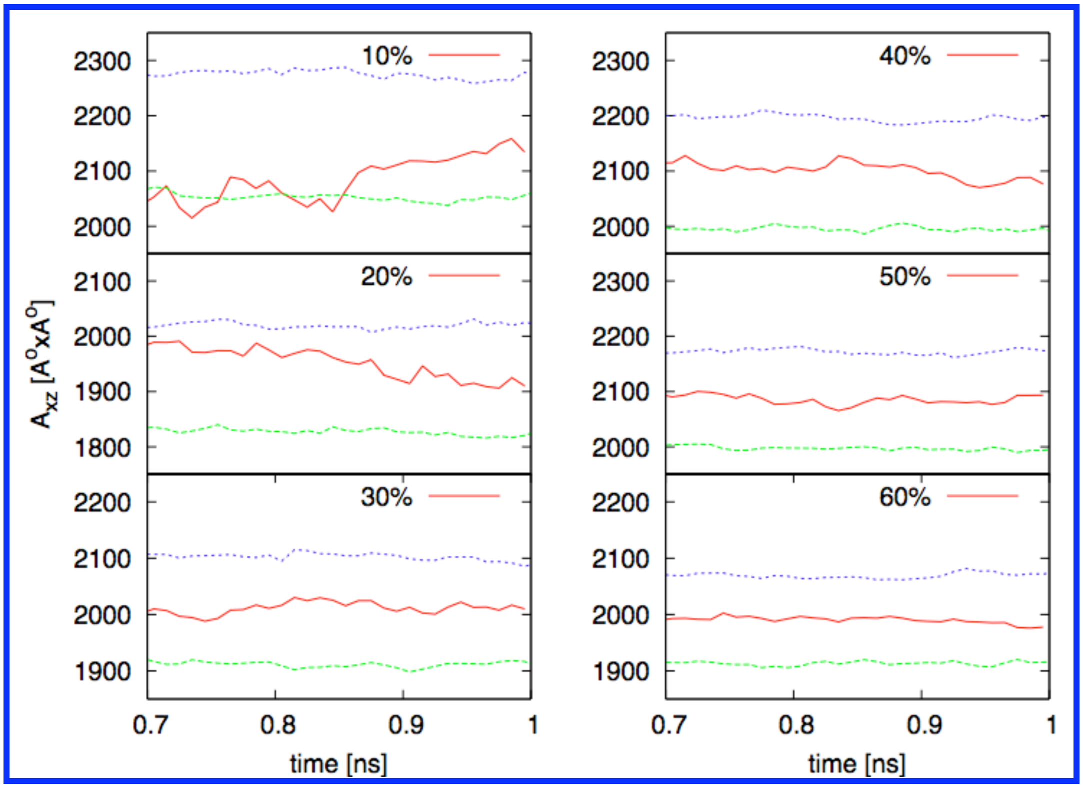

Figure 4.13: Behavior of $Area_{xz}$ $(A^o \times A^o)$, for the last 0.3 ns of equilibration for 3 strained states a) neutral in solid red line b) 5% uniaxial extension by dashed green line c) 5% uniaxial compression by dotted blue line. These results are used to calculate the Poisson's ratio. We note that the drift in initial cross sectional area in α = 10%, 20% is indicative that the networks are fluid at these α.

4.9 References

1. Barnes, S. E. et al. Raman spectroscopic studies of the cure of dicyclopentadiene (DCPD). *Spectrochimica Acta Part A-Molecular and Biomolecular Spectroscopy* **61**, 2946-2952 (2005).
2. Schaubroeck, D., Brughmans, S., Vercaemst, C., Schaubroeck, J. & Verpoort, F. Qualitative FT-Raman investigation of the ring opening metathesis polymerization of dicyclopentadiene. *Journal of Molecular Catalysis A: Chemical* **254**, 180-185 (2006).
3. Wu, C. F. & Xu, W. J. Atomistic molecular simulations of structure and dynamics of crosslinked epoxy resin. *Polymer* **48**, 5802-5812 (2007).
4. Heine, D. R., Grest, G. S., Lorenz, C. D., Tsige, M. & Stevens, M. J. Atomistic simulations of end-linked poly(dimethylsiloxane) networks: Structure and relaxation. *Macromolecules* **37**, 3857-3864 (2004).
5. Komarov, P. V., Chiu, Y. T., Chen, S. M., Khalatur, P. G. & Reineker, P. Highly cross-linked epoxy resins: an atomistic molecular dynamics simulation combined with a mapping/reverse mapping procedure. *Macromolecules* **40**, 8104-8113 (2007).
6. Sun, H. COMPASS: An ab Initio Force-Field Optimized for Condensed-Phase Applications-Overview with Details on Alkane and Benzene Compounds. *Journal of Physical Chemistry B* **102**, 7338-7364 (1998).

7. Plimpton, S. Fast Parallel Algorithms for Short-Range Molecular Dynamics. *Journal of Computational Physics* **117**, 1-19 (1995).
8. Rappe, A. K. & Goddard III, W. A. Charge equilibration for molecular dynamics simulations. *The Journal of Physical Chemistry* **95**, 3358-3363 (1991).
9. Grubbs, R. H. Olefin metathesis. *Tetrahedron* **60**, 7117-7140 (2004).
10. Tuckerman, M. E., Martyna, G. J. & Berne, B. J. Molecular dynamics algorithm for condensed systems with multiple time scales. *The Journal of Chemical Physics* **93**, 1287-1291 (1990).

Chapter 5
Comparisons between Simulations and Experimental Data

5.1 Introduction

In Chapter 3 we derive the factors to convert between LJ units and physical units. We now use these conversion factors to compare the results obtained using the coarse-grained model with those resulting from our atomistic reactive MD simulations. Consistency among the findings from two different numerical approaches can be viewed as a means for initial validation of these methodologies. In Section 5.3 we compare the reaction kinetics and maximum degree of cure values from atomistic, coarse-grained and experimental results. In Section 5.4 we compare the Raman spectra from first principles calculation with experimental data. In Section 5.5 we compare extent of reaction as is calculated from differential scanning calorimetry (DSC) measurements of with our simulation results. Section 5.6 concludes this chapter.

5.2 Coarse-grained Model Validation via Atomistic Simulations

In the following we show how coarse-graining of the atomistic simulations replicates the key features of the ROMP system. Coarse-grained simulations can be used at lesser computational cost and can therefore be used to efficiently scan broad parameter spaces. CG simulations can also provide critical input for atomistic simulation, such as the possible maximum extent of the degree of reaction under various conditions. In Section 5.2.1 we explore the mechanical behaviors of various simulated ROMP networks.

5.2.1 Mechanical Behaviors

Figure 5.1 and Figure 5.2 show the Young's modulus and Poisson's ratio vs. the degree of reaction of networks generated using fully atomistic simulations, coarse-grained simulations based on an interaction model with angular constraints, and coarse-grained simulations without angular constraints, all of the ROMP process. The moduli derived from both CG approaches are converted to real units using a factor of 71 MPa/(LJ unit) as discussed in Chapter 3.

Note that degrees of reaction larger than 0.6 for atomistic simulations required a larger proximity of 6.5Å cut-off distance for reactions to occur. These data are shown for completeness sake. We confine our analysis to the degree of reaction range below ~2/3, which the physically more meaningful as the value coincides with the experimentally observed maximum degree of cure. This has also been the guiding principle for our choice of the reaction cutoff in fully atomistic reactive MD simulations.

While the atomistic simulations and CG simulations with angular constraints yield modulus data that are in good agreement, the CG simulations without angular constraints shows the onset of mechanical rigidity at ~ 0.6 degree of reaction. Apparently, the introduction of angular constraints into the interaction model shifts the percolation threshold to ~ 0.3. In conclusion, we believe that coarse-graining of atomistic simulations cannot be as a simple as a bond only model and still capture essential percolation behavior of DCPD networks.

5.3 Comparison of Reaction Kinetics

In Chapter 3 and Chapter 4 we posit that the reaction processes simulated using fully atomistic and coarse-grained simulations can be described by a rate law consisting of the linear combination of two exponentials. The degree of reaction (α) is well fit by the rate expression below

$$\alpha = 1 - \psi \exp(-t/\tau_1) - \zeta \exp(-t/\tau_2) \tag{5.1}$$

Figure 5.3 shows the experimental [1], scaled fully atomistic reactive MD and scaled angular constraint simulation degree of reaction versus time. The lines represent best fits of the data using eqn(5.1), given above. The scaling factors and parameters for the curve fit are tabulated in Table 5.1. The time scaling factors for atomistic and coarse grained simulations were chosen such that the time required by simulations to achieve α = 0.6 was equal to the real time required to reach maximum degree of reaction ~0.6 as in observed in experiments.

Given the close agreements of the degree of reaction versus time curves of simulations, especially all atomistic simulations, and experiments as can be seen in Figure 5.3, we can state that both the experiments and the simulations follow similar kinetics. This combined with the replication of reaction mechanism gives a high degree of confidence that our simulation effort generates realistic network structure.

We further note that the ratio of the first and second time constants is of great import, we stated in Chapter 3 and 4 that the smaller time constant is a reflection of the reaction kinetic behavior at low degrees of reaction where collisions between catalysts and free sites takes place unimpeded by the nascent network structure. On the other hand the large time constant in the degree of reaction expression is the embodiment of the difficulty of reaction at large degrees of reaction where the catalysts finds it difficult to find neighboring unreacted double bonds. This occurs partly because of the tethered state of the catalyst that in percolated network limits its diffusion, and partly because of the lower diffusion of reaction sites to these catalysts due to impediments imposed by the percolated network. In any case, we find that the comparison ratio of the time constants from the simulations and experiment is good and therefore the major physical features that govern network formation is replicated.

5.4 Experimental and Simulation Raman Spectra Comparison

Since many experimental investigations of the ROMP of DCPD involve Raman spectroscopy, there was interest in comparing the putative Raman spectra of the evolving network structure derived from combined DFT calculations and reactive MD simulations with these experimental results. The DFT calculations of Raman spectra of different molecular groups that exist at intermediate degrees of cure were carried out in collaboration with Changgua Zhen (Materials Science and Engineering, University of Michigan) a member of Prof. John Kieffer's research group.

The following section outlines the method of generating the Raman spectra of structures generated with our MD simulations at various α. We first generate Raman spectra of component molecules that occur within networks generated by the reactive MD simulation using DFT calculations and then compute linear combinations of these spectra in the proportion of the occurrence of the different structural motifs. Figure 5.4b shows us the small fragment molecules that make up the library of all possible molecules formed via ROMP. The methodology for component Raman spectra is explained in Section 5.4.1

and the procedure for using the component Raman spectra in order to generate the network Raman spectra at different α is explained in Section 5.4.2.

5.4.1 Component Raman Spectra Generation Methodology

As discussed in Chapter 2 Section 2.2 we use DFT calculations to investigate properties of DCPD analogues. These DFT simulations also yield Raman spectra along with other salient vibrational spectra of molecules, such as IR and NMR spectra. Since many experimental investigators use Raman spectroscopy to explain the ROMP of DCPD [12] we felt it would be instructive to generate the same for our simulation systems. Calculating Raman spectra of component molecules using DFT overestimates the peak frequencies to a degree that depends on the type of functional used. This overestimation occurs due to the anharmonicity of a vibration and is usually corrected using an empirical correction factor. For the B3LYP/6-31G(d) functional in our DFT simulations. This correction factor is 0.961 [34]

Figure 5.4a shows the resultant Raman spectra for the candidate molecules shown in Figure 5.4b. We restrict our attention to the 1550-1700 (1/cm) frequency range. This frequency range is populated with several peaks that have been assigned to the stretching mode of various C=C bonds. The strained double bonds exhibit a lower C=C stretching frequency that then unstrained C=C. This can be easily understood since an unstrained C=C bond oscillates around its bond energy minima and consequently experiences the largest potential curvature, however a strained bond experiences a curvature of potential that is smaller than the curvature at the minima and hence oscillates at a lower frequency. The ROMP reaction releases the ring strain on its constituent double bonds and the release of ring strain shifts the oscillations from their strained positions to the equilibrium position around the bond energy minima.

Consequently the strained norborene double bond stretching peak initially at 1592(1/cm) and the strained cyclo-pentene double bond stretching peak initially at 1634(1/cm) is shifted to their unstrained stretching frequency of 1660(1/cm) due to the ROMP reaction .

The unstrained C=C stretching frequency closely resembles the ethene double bond stretching peak which in our simulations occurs at 1653(/1/cm). The slight discrepancy is due to the differences in effective mass of the carbons around the networked double bonds. In ethene the carbons are connected to two hydrogens and real molecular networks they are generally connected to one carbon and one hydrogen, which changes their effective mass and hence the frequency of vibration.

5.4.2 Simulated Raman Spectra

In this section we discuss generation of small molecule DFT based Raman spectra. This powerful technique cannot be used for large systems due to large computational overheads required. Raman spectra of large molecules can be approximated by the linear combination of its components, weighting the individual peak heights with component concentrations. This is especially applicable in selected frequency ranges if there is no interference of the peaks in question by other peaks in the same range. In our case we find that the frequency range of interest is 1550-1700(1/cm) and is dominated by the stretching modes of C=C. From our reactive MD simulation as described in Chapter 4 we have an exact picture of how many C=C bonds of each type, whether norborene or cyclopentene, are present in the system at any point in the process.

This insight can be used to formulate the requisite linear combination equation that gives us the Raman spectra at any degree of reaction as is proposed below The molecules **a**, **b**, **c**, and **d** shown in Figure 5.4b can be understood to have the following properties. Molecule **a** is an unreacted DCPD molecule, **b** is a molecule with the norborene ring reacted, **c** is a molecule with the cyclopentene ring reacted, and molecule **d** is a moleule with both rings reacted.

$$R(\nu,\alpha)=\begin{bmatrix} a_o(\alpha)R_o(\nu)+a_1(\alpha)R_{nb\_rxt}(\nu)+ \\ a_2(\alpha)R_{cp\_rxt}(\nu)+a_3(\alpha)R_{both\_rxt}(\nu) \end{bmatrix} \tag{5.2}$$

Where α is the degree of reaction, $a_o(\alpha)$ is the fraction of unreacted DCPD at a degree of reaction α, $a_1(\alpha)$ is the fraction of monomers with only the norborene ring reacted, $a_2(\alpha)$ is the fraction of monomers with only cyclopentene reacted and $a_3(\alpha)$ is the fraction of monomers with both sites reacted. $R_o(\nu)$ $R_{nb\_rxt}(\nu)$ $R_{cp\_rxt}(\nu), R_{both\_rxt}(\nu)$ are the Raman spectra of molecules **a**, **b**, **c**, and **d**, respectively. In our simulations both the norborene ring and the cyclopentene ring react with equal probability as can be seen in Figure 5.5b and therefore we can recast eqn(5.2) as

$$R(\nu,\alpha)=\begin{bmatrix} a_o(\alpha)R_o(\nu)+a_3(\alpha)R_{both\_rxt}(\nu) \\ +\frac{a_s(\alpha)}{2}\left(R_{cp\_rxt}(\nu)+R_{nb\_rxt}(\nu)\right) \end{bmatrix} \tag{5.3}$$

Where $a_s(\alpha)$ is the fraction of monomers with only one of their double bonds reacted. The reacted molecules **b**, **c**, and **d** are species that occur in our simulated configuration with one important caveat: they are connected to other monomers and not capped off by the CH_2 groups as assumed for the DFT calculations. We therefore have to subtract the frequency peaks due to double bonded CH_2 in the spectrum. We propose that this peak is similar to the shifted ethene stretching peak also shown in Figure 5.4a. A straightforward subtraction is not the ideal solution since it neglects molecular cross-section and density details we use a pre-factor to multiply the ethene $CH_2=CH_2$ stretching intensity before subtracting it from component Raman spectra of molecules **b**, **c**, and **d**. Therefore we propose

$$R_{nb\_rxt}(\nu) = R_b(\nu) - fR_{ethene}(\nu) \tag{5.4}$$

$$R_{cp\_rxt}(\nu) = R_c(\nu) - fR_{ethene}(\nu) \tag{5.5}$$

$$R_{both\_rxt}(\nu) = R_d(\nu) - 2fR_{ethene}(\nu) \tag{5.6}$$

Where $f = 5.0$ and Raman spectra of the components along with that of the ethene molecule is given in Figure 5.4a. Figure 5.6 shows the simulated Raman spectra of the DCPD system for our reactive MD simulation and Figure 5.7 shows experimental results from Schaubroeck et al. [1]. The simulated Raman spectra reproduce the transformation peak shifts observed in experimental work,[21] except for the development of a shoulder on the peak assigned to the C=C bond in cyclopentene ring. The emergence of this shoulder has been explained as due to the relaxation of the cyclopentene ring upon opening of the norborene ring. DFT calculations are seemingly not sensitive enough to pick up this nuance.

5.5 Simulated Extent of Reaction via Comparison to DSC Data and Raman Data

DSC is a popular measure for determining the progress of reactions in many chemical systems that are either endothermic or exothermic. The key information is the heat of reaction of the various reactions that take place during the ROMP process. Figure 5.8 shows the reaction pathway of DCPD and the resultant structures that are formed.

In order to calculate the heat of reaction at various degrees of cure we use DFT calculated total ground state energies of component molecules to calculate the associated heat of reaction of ROMP of the norborene and cyclo-pentene rings, as discussed in Chapter 2.

The heat of reaction for the ROMP of the norborene site of DCPD, the cyclo-pentene site, and both sites combined is equivalent to the ring strain energies as tabulated in Chapter 2. We use these values to replicate DSC measurements in a recent work by Mauldin et. Al.,[5] which describes measurements of the extent of reaction of the DCPD system using DSC. The degree of reaction is defined as

$$\beta(t) = \frac{H(t)}{H_R}, \tag{5.7}$$

where H(t) is the total heat evolved during time t and H_R is the combined heat of reaction of norborene and cyclo-pentene C=C bonds reacting via the ROMP. This degree of reaction is at variance with our definition of the degree of reaction α(t) defined by eqn(5.8), and corresponds to the fraction of double bonds reacted. However we can convert the degree of reaction observed in our simulations to experimentally observable DSC calculated degree of reaction by using eqn(5.9).

$$\alpha(t) = \frac{(\alpha_{nb} + \alpha_{cp} + 2\alpha_R)}{2} \tag{5.8}$$

$$\beta(t) = \frac{(\alpha_{nb} H_{nb} + \alpha_{cp} H_{cp} + \alpha_R H_R)}{H_R} \tag{5.9}$$

Where α_{nb}, α_{cp} and α_R are the fractions of **b**, **c**, and **d** species. H_{nb}, H_{cp} and H_R are the heats of reaction of the 3 reactions as described above. Table 2.2 and Table 2.3 shows the values of the heats of reaction of these reactions for exo and endo DCPD respectively.

It is immediately obvious from the magnitudes of H_{nb},, H_{cp},, H_R that DSC measurements of the degree of reaction cannot capture the cross-linking reaction process adequately. The cross-linking reaction releases only miniscule amount of heat or even consumes heat liberated for the endo-DCPD system. For the exo-DCPD system the heat released by the cyclopentene group is smaller than the norborene group and one cannot decipher what double bond has reacted based on the heat generated as the reaction progresses.

In trying to model the DSC data from reference [5] we assume that the exo-DCPD plausibly follows only the all-exothermic path to the final cross-linked state, which corresponds to a pathway of reaction 1 followed by reaction 3, as described in Figure 5.8 then (5.9) reduces to

$$\beta(t) = \frac{(\alpha_{nb} H_{nb} + \alpha_R H_R)}{H_R} \tag{5.10}$$

This is because we assume that only the norborene reaction releases heat and the cyclopentene reaction only releases heat if the norborene ring on its monomer is reacted, and that combined heat of reaction is assimilated by the H_R term. Based on this transformation we plot $\beta(t)$ with $\alpha(t)$ for our atomistic simulations in Figure 5.9 for the exo-DCPD system. We can see that the final data point observed by DSC measurements [5] coincides with our simulated DSC measurements at a maximum degree of cure of 0.6377. However this analysis is based on a set of very restrictive assumptions and needs further experimental verification. We believe that describing the degree of reaction as suggested in eqn(5.9) is inadequate and experimental characterization techniques such as analyzing Raman spectra are superior since they directly probe the molecular transformations that take place. Figure 5.3 show experimental results [1] and our simulation results for the kinetics of reaction.

One of the critical parameters of our reactive MD simulation is the reaction cut-off distance, which was chosen based on the criteria of reaching experimentally observed maximum degree of reaction of 60%. A reaction cut-off distance greater than 6.0 Å resulted in conversion greater than 60% and vice versa in computationally accessible times of < 500 hours given system sizes under consideration. The greater than 60% conversion shown in some graphs in this work were achieved after resetting the reaction cut-offs to 6.5 Å however we believe these degrees of reaction are merely of academic interest and is unlikely to occur naturally with current generation catalysts.

5.6 Conclusions

We show that the simulations reproduce experimental observations in many key areas such as reaction kinetics, maximum extent of reaction and the evolution of Raman spectra. We hope shortly that we will be able to validate the modulus simulation results after experimental investigation currently underway using Brillouin spectroscopy is completed.

As a result of this simulation work it is now possible to predict the mechanical performance of new generation catalysts provided models of how they react to form networks is made available. This allows us to design the network structure in unique ways, drive experimental work and perhaps as methods increase in sophistication subsume them completely. Also with such success we can now think of creating other amorphous network polymers such as epoxies and explore their mechanical properties with a great degree of flexibility.

5.7 Tables

Table 5.1:Scaling factors and other details of the fit to eqn(5.1).

System	**Time Scale**	ψ	ζ	τ_1 (min)	τ_2 (min)	$\frac{\tau_1}{\tau_2}$
Experimental	1.0	0.54	0.46	11358	335	34
Atomistic Simulation	1100 (min/ns)	0.5	0.5	19129	412	46
Angular ROMP Simulation	0.132 (min/τ)	0.42	0.58	20283	416	49

The ratio τ_1/τ_2 is a good indicator that simulations and experiments are kinetically comparable even though the simulations acheive α = 0.6 in a simulation time of 5.0ns whereas in reality this process takes a few hours. We can see that the 2 simulation techniques are roughly comparable, however there is a significant difference in the ratio. This means that our simulations do not capture all the features that govern the kinetics present in the real system.

5.8 Figures:

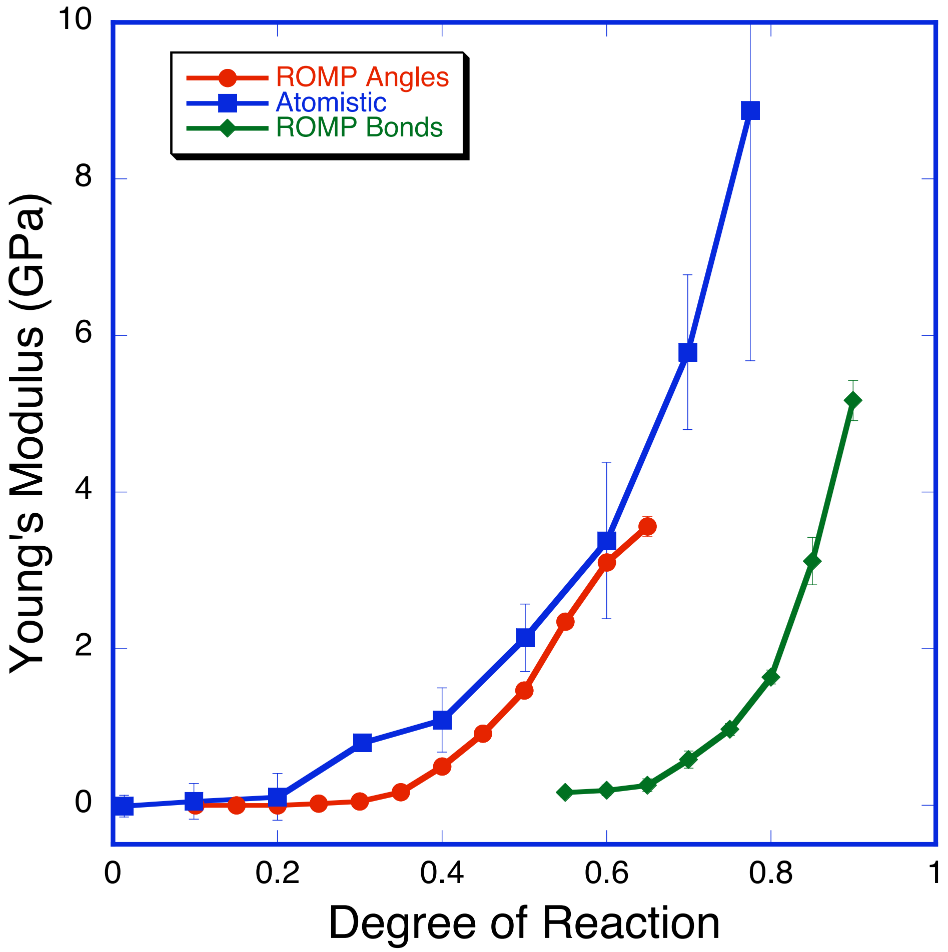

Figure 5.1:Young's modulus of atomistic, angular coarse grained and non-angular coarse-grained networks. The ROMP network with angular constraints shows good agreement with our all atomistic simulations. The ROMP networks with no angular constraints show drastically different behavior.

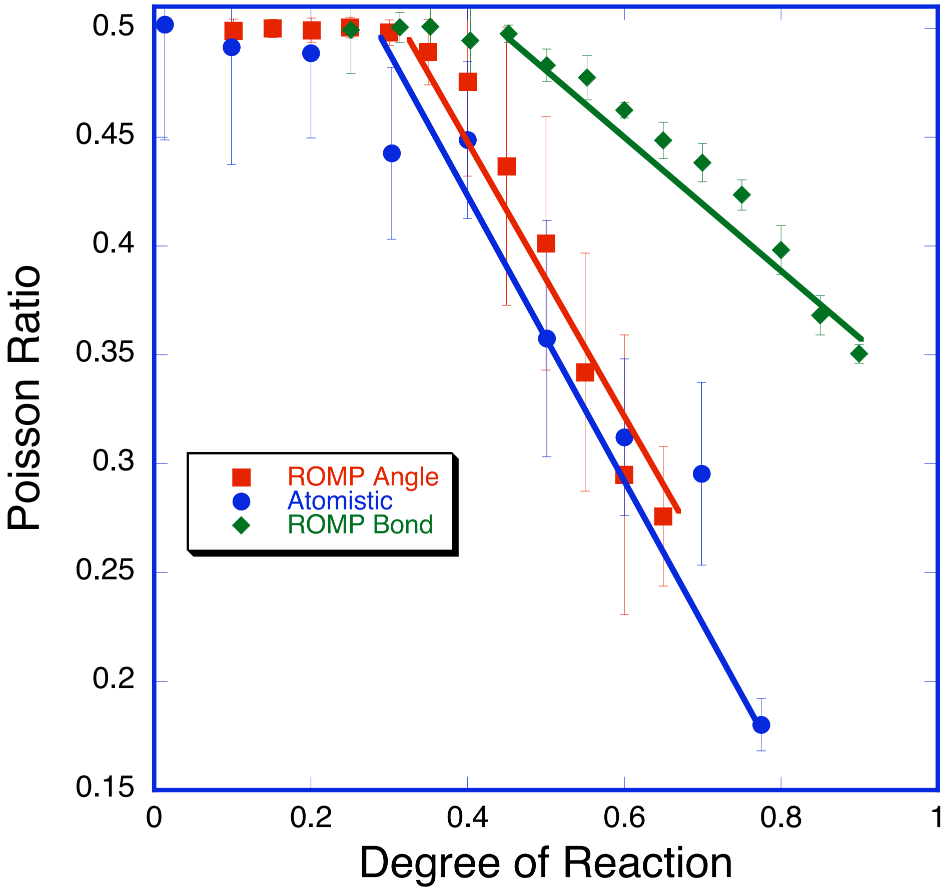

Figure 5.2: Poisson's ratio of atomistic, angular coarse grained and non-angular coarse grained networks

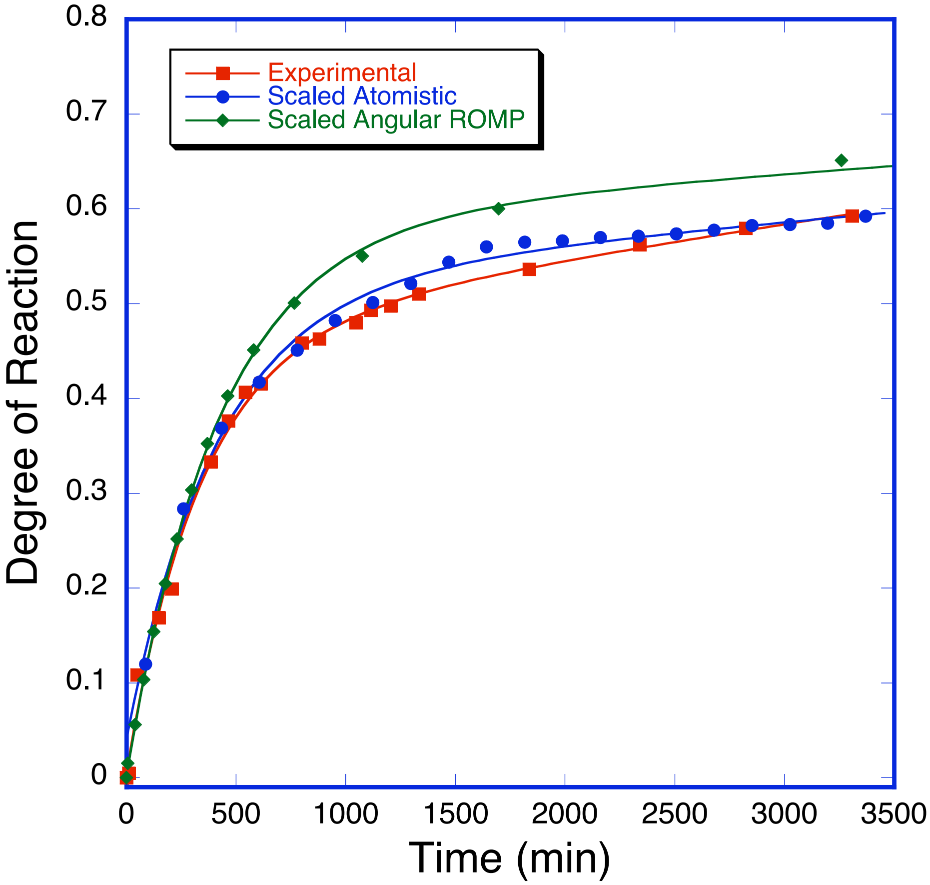

Figure 5.3: Experimental, Scaled Atomistic and Scaled Angular ROMP Degree of reaction with time.

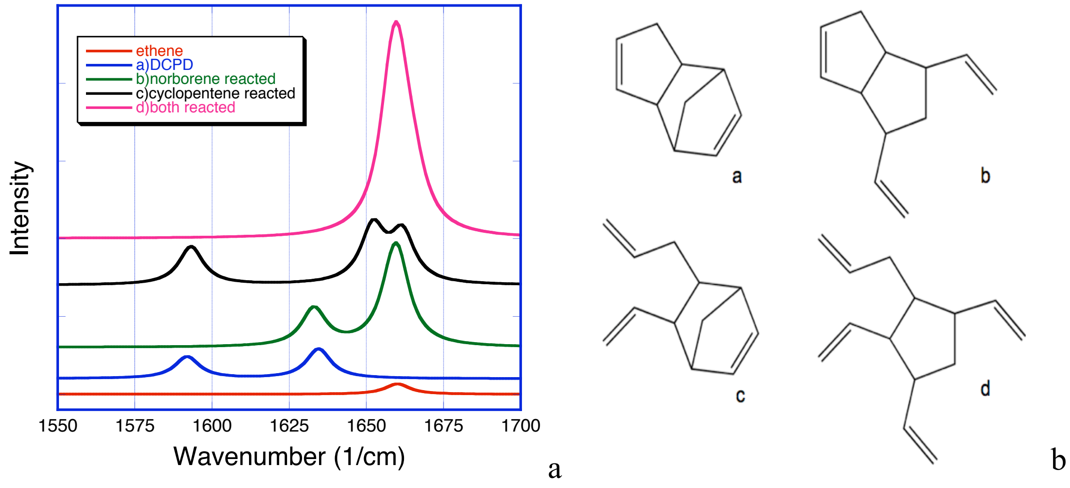

Figure 5.4: a) Component DFT Raman spectra b) Molecule Visualization

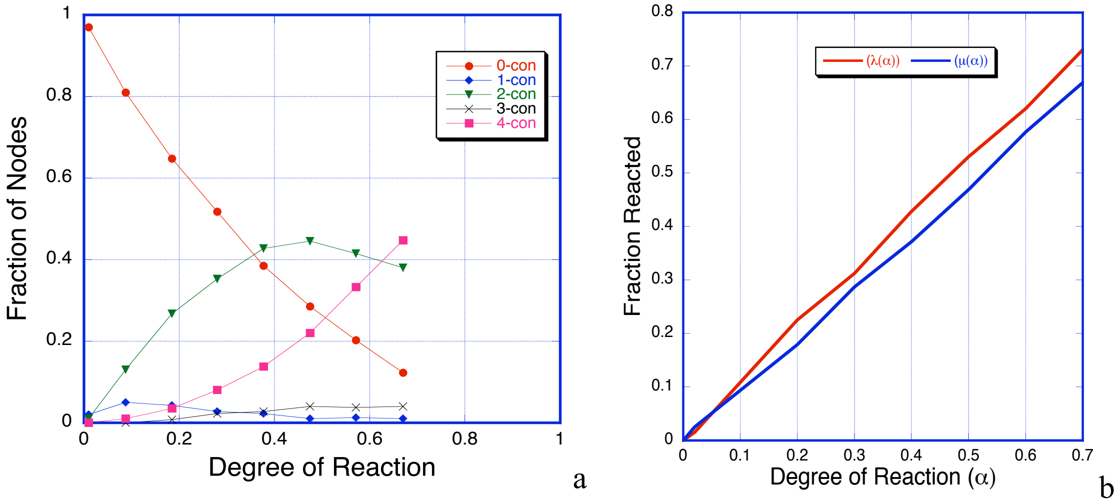

Figure 5.5: a) Node Connectivity b) $\lambda(\alpha)$ (norborene)/ $\mu(\alpha)$ (cyclopentene) vs degree of reaction

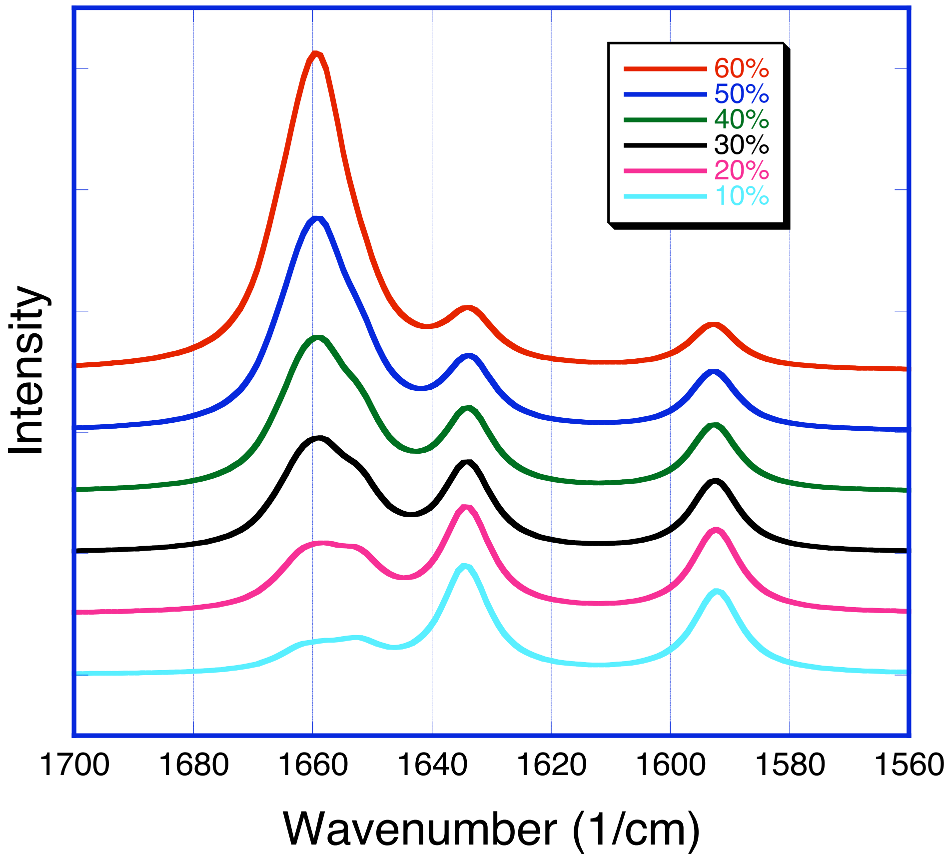

Figure 5.6: Simulated Raman spectra: MD reaction model and DFT. The legend represents the degree of reaction. The simulated Raman spectra reproduces the key features of the experimental observations. Increase in the 1660 peak with concurrent decrease in the peaks at 1635 and 1593. A shoulder at 1650 is also discernable at low degrees of reaction.

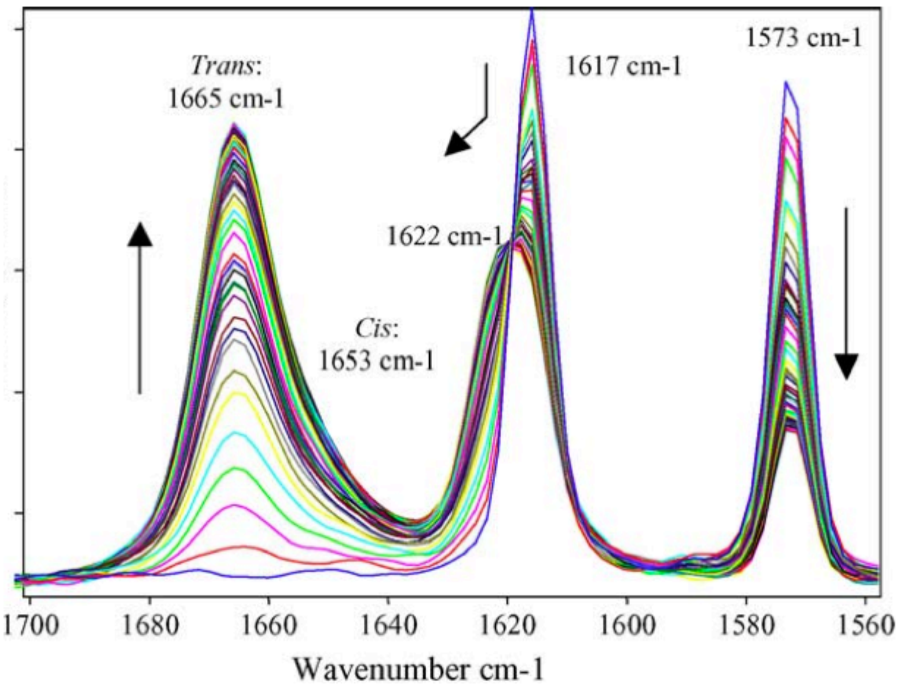

Figure 5.7: Experimental Raman spectra of DCPD undergoing ROMP Schaubroeck et al[1]. We see increase in the 1665 peak with concurrent decrease in 1570 peak along with a decrease in 1617 peak.

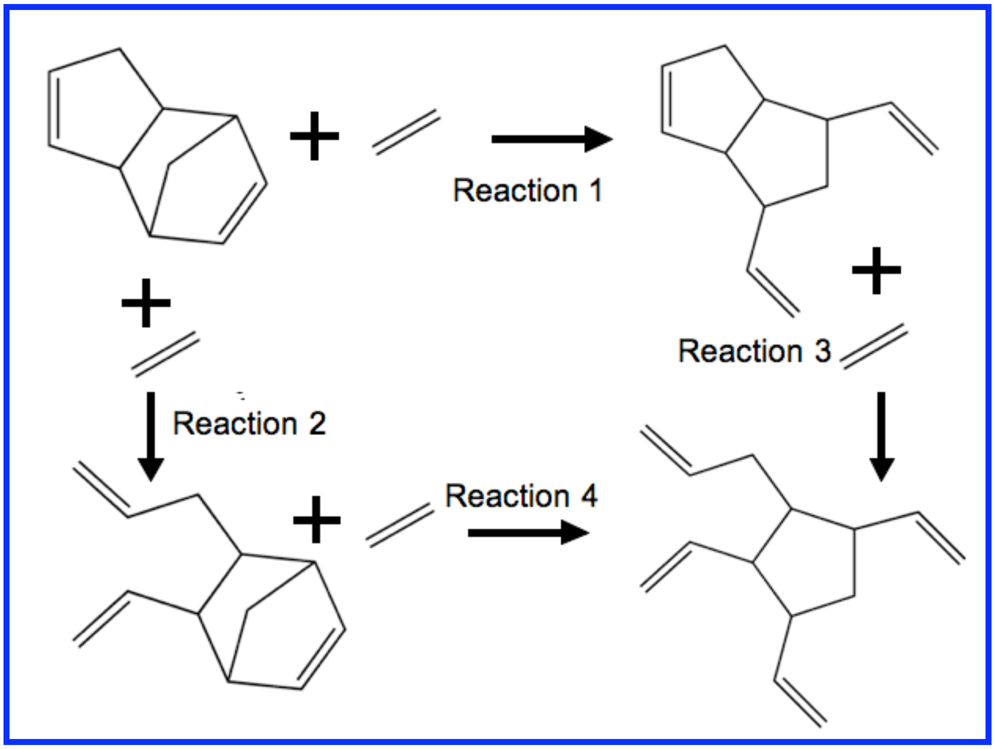

Figure 5.8: Reaction Pathways of DCPD undergoing ROMP with ethene. Reaction (1) is the norborene ring opening, Reaction (2) is the cyclo-pentene ring opening. Reaction (3) is the cyclo-pentene ring opening after reaction 1 and Reaction (4) is the norborene ring opening after reaction (2).

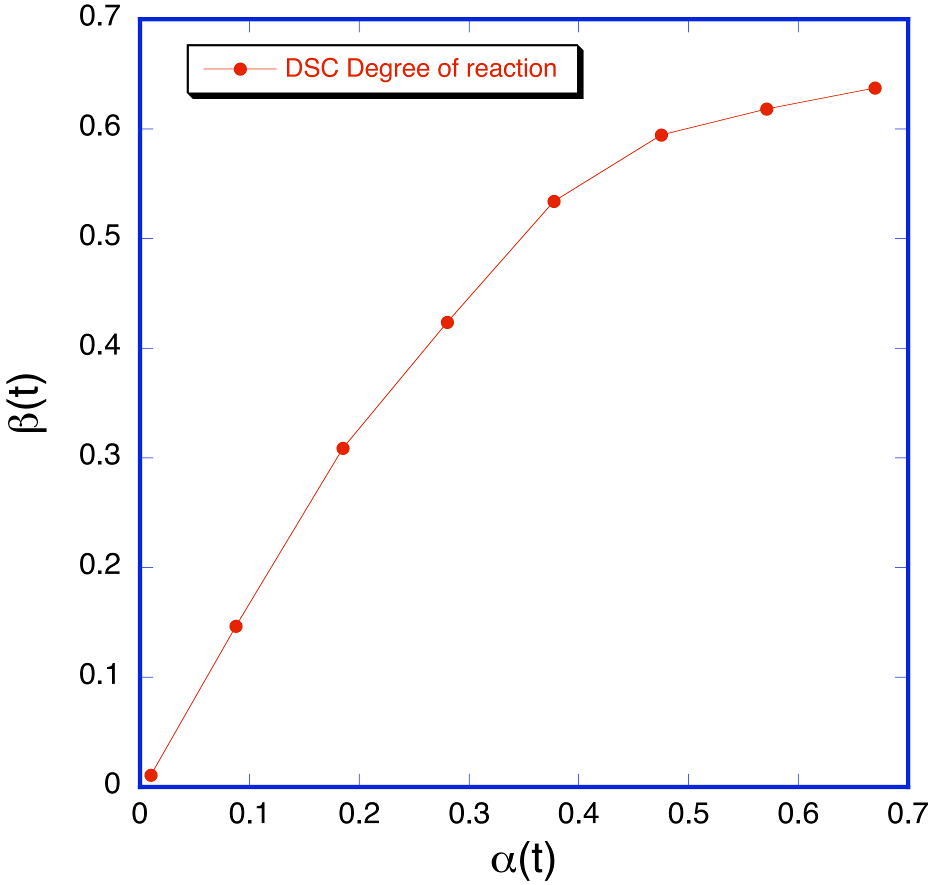

Figure 5.9: DSC calculated degree of reaction (y-axis) vs. actual degree of reaction (x-axis). The simulation prediction of the DSC maximum extent of reaction is 0.65 is closed to what is measured in experiments.

5.9 References

1. Schaubroeck, D., Brughmans, S., Vercaemst, C., Schaubroeck, J. & Verpoort, F. Qualitative FT-Raman investigation of the ring opening metathesis polymerization of dicyclopentadiene. *Journal of Molecular Catalysis A: Chemical* **254**, 180-185 (2006).
2. Barnes, S. E. et al. Raman spectroscopic studies of the cure of dicyclopentadiene (DCPD). *Spectrochimica Acta Part A-Molecular and Biomolecular Spectroscopy* **61**, 2946-2952 (2005).
3. Scott, A. P. & Radom, L. Harmonic Vibrational Frequencies: An Evaluation of Hartree-Fock, Moller-Plesset, Quadratic Configuration Interaction, Density Functional Theory, and Semiempirical Scale Factors. *Journal of Physical Chemistry Journal of Physical Chemistry J. Phys. Chem.* **100**, 16502-16513 (1996).
4. Szczepaniak, K., Szczesniak, M. M. & Person, W. B. Raman and Infrared Spectra of Thymine. A Matrix Isolation and DFT Study. *Journal of Physical Chemistry A Journal of Physical Chemistry A J. Phys. Chem. A* **104**, 3852-3863 (2000).
5. Mauldin, T. C., Rule, J. D., Sottos, N. R., White, S. R. & Moore, J. S. Self-healing kinetics and the stereoisomers of dicyclopentadiene. *Journal of The Royal Society Interface* **4**, 389-393 (2007).

Chapter 6
Graph Theory Characterization of Networks

6.1 Introduction

In Chapters 3 and 4 we reveal the importance of structure for the mechanical behavior of amorphous polymer networks, separate from the strengths of bonds, bond angles and dihedral angles and other short range interactions that are commonly assumed to be responsible for the mechanical properties in most materials. In Chapter 3 and Chapter 4 we show the modulus behavior below the Poisson threshold (α_P) is primarily due to entropic contributions. Therefore networks behave more like polymers rather than ionic glasses under this limit.

Amorphous materials such as cross-linked polymer networks are fundamentally different from other amorphous materials such as covalent, ionic, or metallic glasses, which generally exhibit different bonding topology. We posit that cross-linked polymer networks derive their elastic behavior from their specific topology of their connections. Below the Poisson's threshold, network polymers retain the ability to reorient themselves under deformation without changing internal energy and density. This ability is lost above the Poisson's threshold and can be seen in either the increase in internal energy, a feature that is hard to measure for small strains, or by the more easily observed decrease in density with deformation. Below α_P the form of interaction potentials of bonds, dihedrals, and other non-pair interactions does not play a role in elastic behavior, what is more important is the geometric constraints imposed by such interactions. Rubbery elasticity is due to a change in configurational states available to the network after deformation

Many simulations and experiments of glasses report the bulk modulus, however such measurements do not take into account regimes where the glasses behave like polymers since such behavior is generally not expected. These phenomena is however critical in the evolution of elastic properties of polymers. We note that bulk modulus is quantity that necessarily probes the strength of particle interactions due to its isotropic nature. Bulk modulus measurements always result in changes in density and internal energy unlike a Young's modulus measurement where deformations can occur with no change in density or internal energy In Uniaxial measurements such as the Young's modulus test that we use to probe mechanical properties allow transverse axes rearrangements. This allows response to deformation conserving internal energy and therefore density. Most physical deformations are not isotropic in nature and therefore Young's modulus is a better indicator of material properties than the bulk modulus.

Here we explore whether the key difference between amorphous network polymers and ionic glasses can be understood through their representation in graph theory terms. Consider a covalent network polymer made up of atoms bonded to each other. Each atom can be thought of as a node in the network and each constraint a unit value in the so-called adjacency matrix reflecting the connection between two nodes.

For example if atom i is connected to atom j with a bond then we can think of an interaction adjacency matrix A such that

$$A_{ij} = 1; \tag{6.1}$$

otherwise, if particles *i* and *j* are not connected, this matrix element is zero. Similarly if 3 nodes *i-j-k* form an angle,

$$A_{ik} = 1 \tag{6.2}$$

Since we have already included the bonding interaction *i-j* and *j-k* in eqn(6.1) we have also completely described the angular interaction. Now let us consider the dihedral interaction *i-j-k-l* , a strong dihedral interaction such as that in a double bond constrains the *i* and *l* nodes to the same plane. Therefore we can then state that

$$A_{il} = 1 \tag{6.3}$$

We can therefore create a matrix representation of all interactions between participating nodes of a molecular network in our adjacency matrix as described above. All these interactions occur within a definable cutoff radius and therefore yield a matrix that is sparse.

Ionic glasses such as silicates on the other hand contain charges that make this description difficult since the effect of coulomb interactions at long distances though individually small is collectively still significant. These long-range interactions in effect nullify the sparse matrix assumption for the case of ionic glasses that we can successfully make for polymer networks.

Therefore mechanical characterization analysis routinely used for glasses does not translate well to network polymers. In the following sections we concentrate on of molecular networks with only covalent bonding interactions to identify network measures that correlate with the observed Young's modulus behavior.

Briefly we will discuss Eigenvalue centrality in Section 6.2, Fractal dimension in Section 6.3, Fiedler partitioning in Section 6.4 and average crosslink density in Section

6.5. Section 6.6 discusses the results of such network characterizations and their utility as indicators of elastic modulus. We note that our analysis is limited to only bonding interactions and we discount any angular or dihedral interactions as mentioned above. This assumption limits us to probing networks that only have bonding interactions. In our case we concentrate on ROMP and RANDOM network without angular constraints as described in Chapter 3, and for atomistic simulations we make the simplifying assumption that the complicated bonding interactions between monomers, consisting of bonds dihedrals and multiple atoms, can be approximated by simple bonds between the center of masses and due to the inherent flexibility of these connections there exist no angular or dihedral constraints between connected monomer center of masses.

6.2 Eigenvalue Centrality Measure

The eigenvalue centrality (EC) measure assigns a score to a node in a network based on its connections to other nodes. It is based on the assumption that a node with connections to other higher scoring nodes itself gets a higher score as compared to another node with the same number of connections to lower scoring nodes. The magnitude of the EC of a node is a measure of the burden assumed by this node in the network. We are therefore motivated by the idea that the number of higher scoring nodes in a network could also be indicative of the network mechanical performance.

The eigenvalue centrality of a node in a network can be calculated as follows. Let us assume that node i is given a score of x. According to the fundamental assumption stated above let the score of node i be proportional to the sum of the scores of nodes it connects to. We can therefore write

$$x_i = \frac{1}{\lambda} \sum_{j \in E(i)} x_j \tag{6.4}$$

Where $E(i)$ is the set of nodes connected to *i*. This can then be framed as below

$$x_i = \frac{1}{\lambda} \sum_{j=1}^{N} A_{ij} x_j \tag{6.5}$$

where λ is an eigenvalue of A_{ij} and

$$A_{ij} = \begin{bmatrix} 1 & \mathit{if}\ i - j\ \mathit{connected} \\ 0 & \mathit{if}\ \mathit{not\ connected} \end{bmatrix} \tag{6.6}$$

We note that eqn(6.6) is the standard definition of an undirected adjacency matrix. The adjacency matrix is a symmetric matrix that by definition has real positive eigenvalues. Immediately we can reframe eqn(6.5) into an eigenvalue problem as below

$$A_{ij} x = \lambda x \tag{6.7}$$

There are N (equal to number of nodes) real positive eigenvalues of the matrix A. However the condition that all $x_i > 0$, can only be satisfied for the largest eigenvalue, henceforth called the cardinal eigenvalue. The fact that the largest eigenvalue ensures that all eigenvector coefficients are positive is a direct consequence of the famous Perron–Frobenius theorem in graph theory. The coefficients of the eigenvector represented by the array x_i for the cardinal eigenvalue is therefore the score we aim to calculate. This score is called the eigenvalue centrality or simply centrality of a node or in this work alternatively also called the cardinal eigenvalue centrality.

It can be seen that for a simulation system that is N atoms large, the eigenvalue problem is $O(N^2)$. A typical MD simulation in this study used systems that were ~10000 atoms. The eigenvalue problem of the full matrix therefore becomes difficult to solve. However it is to be noted that the number of connections for each node/atom is quite low (typically <4) for our molecular systems and therefore the adjacency matrix is sparse and is O(E). Where is E is the number of edges that is approximately O(N).

We used the sparse matrix libraries in the Python module **pysparse** to calculate the largest eigenvalues of the simulation adjacency matrix. The results of these calculations are discussed in Section 6.6. We normalize the eigenvector coefficient obtained by dividing with $N^{0.5}$ since an ideal network is a crystalline structure. This implies that all nodes in the crystal lattice are equally important and consequently will have the same eigenvector coefficient equal to $N^{0.5}$. This value is therefore used to normalize the eigenvector coefficients calculated for our networks

Figure 6.1 shows the spectrum of the normalized eigenvector centrality scores for a ROMP network, Figure 6.2 shows the spectrum of eigenvector centrality of a RANDOM network and Figure 6.3 shows the spectrum of centrality scores for the atomistic center of mass network. If we compare Figure 6.1 and Figure 6.2 we can see that the ROMP network exhibits a maxima at eigenvector coefficients values than the corresponding RANDOM case. For example we find that the maxima for $\alpha = 0.6$ in ROMP occurs at between -17 and -16 in the graph whereas the same occurs in the RANDOM case at a value of -18 and -19. This implies that there are a lot of nodes in ROMP networks of high centrality as compared to the RANDOM case. In effect this points to the fact that ROMP networks at almost all but the highest degree of reaction have a larger number of nodes that are better connected to each other.

We cannot directly compare Figure 6.3 with Figure 6.1 and Figure 6.2 since the system sizes are different and the scaling of centrality values of nodes makes it hard to normalize for system size. However we can see that since the atomistic networks follow the ROMP mechanism they too show the same trend of high centrality nodes at low degrees of reaction. A better comparison is to calculate the fraction of high centrality nodes as is discussed below.

Figure 6.4 shows the fraction of monomers in each system that has an eigenvalue centrality greater than 10^{-30} i.e. the machine precision limit of the sparse matrix solver. We find that the ROMP network shows a lower threshold for percolation of the high centrality fraction. This figure shows that ROMP and atomistic networks have the similar profile of high centrality nodes since they both follow the same reaction mechanisms. However the atomistic networks percolate seemingly at a lower threshold than both ROMP and RANDOM networks. This is because we have used the same cutoff for determining the high centrality nodes all three curves. Choosing the right cutoff for high centrality changes the threshold and the value itself is dependant on system size. In this exploratory work we have not been able to determine the exact criteria for choosing cutoffs and this is part of the outlook for such characterization methods.

6.3 Graph Fractal Dimension

Conventional formulations of fractal dimension derived from the RDFs of atomic positions in a simulation [1] [2] of networks cannot exceed the dimension of the physical space that a system exists in. However we can define a graph theoretical fractal dimension that is based on the connectivity of the network. as suggested by Shanker [3]. We can define a function $V(r)$ that is the total number of nodes reachable by shortest paths less than r bonds moves from a given central node. In general $V(r)$ scales as

$$V(r) = kr^{d}, \tag{6.8}$$

where we term *d* as the graph fractal dimension. We note that the graph fractal dimension for any network cannot exceed the maximum connectivity of any node. In our systems we are limited to a maximum of 4 bonds per node and therefore $d < 4$.

Intuitively V(r) can be understood as a volume function that describes the graph node volume within r bond moves of a central point in the network. However we note that a move along a bond could double back in real space according to the coordinates of the bond in question. Equivalently we define a surface function S(r) that is the number of nodes that have exactly r links in their shortest path to a central node. S(r) can be written as shown below.

$$S(r) = kdr^{d-1} \tag{6.9}$$

We are interested in knowing how the graph fractal dimension scales with the mechanical properties of a network. This is especially interesting since we think that a larger fractal dimension implies a larger Young's modulus because of it denotes a network that is better connected. Therefore we believe that this measure may be a promising candidate network characteristic.

We calculate the graph fractal dimension using the following procedure. We randomly choose N/2 of the nodes and calculate the S(r) for values of r up to 5. For each randomly chosen node we average the individual values of S(r) over all the randomly chosen nodes to a value $\langle S(r) \rangle$, where the average is given by

$$\langle S(r) \rangle = \frac{\sum_{j}^{N/2} S(r)}{N/2}, \tag{6.10}$$

where node j is one of the randomly chosen nodes form the network. We then fit the value s of $\langle S(r) \rangle$ at different r to eqn(6.9) to get the value of d and k for a given network.

The choice of N/2 random nodes is ad-hoc and for large networks this fraction could be even smaller. A larger fraction only reduces the noise in the S(r) values.

We note that we cannot use large values of r in our calculations of $\langle S(r) \rangle$ because the analysis is only valid for infinite systems and if we include periodic images of particles at larger distances, the analysis is no longer valid. To avoid this problem we ensure that the volume function V(r) at the highest r is around N/2. Assuming that d<4 from previous discussion, we can see that our choice of r≤5 places an upper limit on the volume. At r = 5 $V(r) \leq 5^4 = 625$, which satisfies keeping the volume function to less than N/2 in our of coarse-grained simulations with 16000 nodes. For our atomistic systems we only fit $S(r)$ up to r = 4 since the number of monomers in our atomistic simulations is 400. $V(r) \leq 4^4 = 256$ which is close to the N/2 limit. Note that our atomistic simulations in general have ~8000 atoms but we choose to analyze the atomistic network based on monomer connectivity and not atomic connectivity

The results of the graph fractal dimension calculation for ROMP, RANDOM and all atomistic DCPD center of mass (COM) networks is shown in Figure 6.5

6.4 Fiedler Partitioning of Graphs

Graph partitioning is a well-studied problem with many different methodologies that enable graph partitioning. Fiedler partitioning of graphs is a method that allows graphs to be partitioned into 2 almost equal parts with the minimum number of edge cuts. Recently this method has been used by Sibsankar and Kundu[4] to delineate protein structures to identify hinge points in their structure, so as to access low frequency motions of the macromolecule. We therefore propose to use this technique to identify the bonds that partition the simulation network into two components. Intuitively the number of bonds that constitute the edge cut is a good indication of the mechanical properties of the network. It may be argued that the edge cut is more indicative of the strength or fracture toughness of a structure than its elastic modulus. However since these quantities are related we believe that the Fiedler partitioning could provide a useful indicator of network properties.

Calculation of the Fiedler partition of a network involves finding eigenvalues of the Laplacian matrix of the graph. The Laplacian matrix is related to an adjacency matrix and is defined as

$$L = D - A \qquad (6.11)$$

Where D is the diagonal matrix whose elements are given by

$$D_{ii} = \sum_j A_{ij} \qquad (6.12)$$

The eigenvalues of the Laplacian matrix have many interesting properties. If we assume that $\lambda_1, \lambda_2, \lambda_3, \cdots \lambda_i \cdots \lambda_N$ are the eigenvalues of the Laplacian matrix then the number of times 0 appears as eigenvalues is equivalent to the number of disjoint sub graphs in the system. It is well known that symmetric real matrices have only positive real eigenvalues.

More interesting for our purposes is the behavior of the smallest non-zero eigenvalue, also called the Laplacian spectral gap henceforth referred to as λ_S. One interesting property is that the larger λ_S, the better connected is the network. The eigenvector of the eigenvalue λ_S yields a set of coefficients for each node of the network. The positive and negative coefficients values automatically delineate the nodes into two roughly equal parts and the edges that span nodes with coefficients of opposite sign are then the cut edges that divide the network.

Solving the Laplacian matrix in its full form for even reasonably sized graphs such as ours, where system sizes of N~10000 makes the full matrix solution prohibitive as in Section 6.2. As discussed before we use the Python module **pysparse** for sparse matrix calculations, since the Laplacian matrix shares the O(E) scaling behavior of adjacency matrix. However for networks with significant fractions of unreacted monomers or smaller unconnected fragments it becomes necessary to select the giant component or the largest fully connected fragment of the network and then perform the Laplacian eigenvalue analysis for the smallest non-zero eigenvalue. This is because of the fact that we would get a number of zeros equivalent to the number of disjointed components of the submitted network as eigenvalues, when we subject an incompletely connected graph to Fiedler analysis. The sparse matrix solver works the best when deployed to calculate a small number of eigenvalues around a certain range we want. In our case for Fiedler analysis we want the smallest non-zero positive eigenvalue and therefore we set the sparse matrix solver to calculate values near zero. In order to achieve this we use the Python **igraph** module to extract the largest connected component among all fully connected components and then use **pysparse** to calculate the smallest positive eigenvalue.

We also investigated the relation of the fraction defined by the number of the cut edges divided by the total number of surface nodes S_N (S_N: defined below) among various networks i.e. ROMP, RANDOM and atomistic-COM systems. We define surface nodes as follows, in a simulation box with periodic boundary conditions (PBC), an intuitive way to separate a graph into two disjoint parts is to cut the box along all periodic surfaces and then apply a final cutting surface thru the middle of the box in the plane that creates the least surface area. This involves cleaving the box along six faces and one extra plane for a total of 7 planes that creates two sub-volumes of a simulation box, with no contiguous path of nearest-neighbor nodes between the two components. For a cubic box with N total nodes the number of nodes on these 7 surfaces assuming uniform density is given by

$$S_N = 7N^{2/3} \tag{6.13}$$

We divide by the fraction of surface nodes because Fiedler partitioning is basically a surface generating procedure that scales according to surface area and not volume and therefore dividing by the total number of nodes is not the correct normalization procedure. We show the Fiedler cut fraction for configurations generated according to the coarse grained ROMP, coarse grained RANDOM and atomistic center of mass graphs in Figure 6.6. In this case the plot shows on the fraction of bonds that need to be cut to split the network in to two disconnected sub-graphs. The fraction is calculated as the number of bonds to be cut using the Fiedler partitioning algorithm divided by the number of bonds that would be cut if we artificially created planar surfaces on the boundaries of the simulation box at any degree of reaction. The plot shows that the ROMP networks have a slightly lower point at which percolation of cut bonds takes place. The atomistic center of mass curves closely follows the ROMP network. We note here the scaling according to system size is more easily achieved. This is because the denominator and the numerator of the fraction calculated scale similarly as we change system size.

6.5 Average Cross-link Density.

As discussed in Chapter 1 many theories polymer networks such as Flory et al [5] suggest that the modulus values of networks scale as the density if cross-link per unit volume. The cross-link density can be thought of as the fraction of nodes that have 3 or greater number of bonds. Cross-link density is plotted as a function of the degree of reaction for ROMP, RANDOM and atomistic-COM network in Figure 6.7. We can see that the curves for cross-link fraction are smooth unlike the other calculated network quantities and does not show any threshold behavior. Also we note the RANDOM network has a larger fraction of cross-linked nodes than the ROMP network. This would suggest that the RANDOM network is mechanically superior to the ROMP network contrary to what is observed. These two factors lead us to conclude that this characteristic of networks is insufficient to explain observed mechanical behavior. The curve for atomistic networks is provided for comparison purposes to the ROMP network . It shows that even though the mechanisms of network formation in atomistic is similar to that of the ROMP network the speciation is significantly different and therefore likely to affect mechanical behavior.

6.6 Results and Discussion

We tried 4 network characterization methods 1) Eigenvector centrality 2) Graph spectral dimension 3) Fiedler partitioning and 4) Crosslink fraction. We then plot the Young's modulus of atomistic networks with the calculated network measure as shown in Figure 6.8. It appears from the good linearity of the Figure 6.8d that the crosslink density is the best indicator of mechanical properties as is suggested in classical polymer elasticity theories. However we see from Figure 6.7 that the RANDOM networks have a higher crosslink fraction than the ROMP networks and therefore should in theory have a higher modulus as predicted by classical entropic formulations as is discussed in Chapter 1. However it is evident from our simulations of ROMP and RANDOM networks that the reverse trend i.e. that of the Young's modulus of ROMP networks being greater than that of RANDOM networks is manifest. This discrepancy can be explained by the larger fraction of free ends and unreacted monomers in RANDOM networks as compared to ROMP networks. Secondly, the fraction of cross-links with degree of reaction does not show a threshold behavior we have come to expect from our simulations therefore while the correlations are good the suitability of this measure is suspect.

We see that the best characterization technique among those we tried is the Fiedler partitioning method. Not only do we see good linear behavior in Figure 6.8c we also see that the partitioning method correctly predicts the ROMP network to have a higher modulus than the RANDOM network as can be seen from the trend in Figure 6.6.

In conclusion therefore we propose the Fiedler vector cut bond per surface node characterization the most reliable predictor of modulus behavior and recommend further investigations in other materials. We also note that the eigenvalue centrality cutoff was arbitrarily chosen to classify high centrality as any node, which has an eigenvector coefficient greater than machine precision (here 10^{30}). This choice is ad-hoc and we believe there may be a correlation between nodes of high centrality and their influence on mechanical behavior. This however will be the topic of future exploration.

The graph fractal dimension does not show the threshold behavior that is expected but nevertheless still communicates the basic premise that the network coalesces fast as the degree of reaction increases and then this measure saturates to a maximum value.

6.7 Conclusion

One major question that remains unanswered is the prediction of the Young's and Poisson's threshold values for arbitrary networks. These thresholds appear to be different from the ordinarily known percolation thresholds such as those stated by glassy theories. Our attempt to characterize the networks does not address this question completely, though it offers correlations with the Young's modulus data. This question is relevant to many other materials whose elastic response is yet undelineated into fluid, entropic, or enthalpic regimes. A deeper understanding of such phenomena is part of our future endeavors.

We also state here without proof based on our physical understanding that the Young's modulus below the Young's threshold is linearly dependant on temperature as is well understood from polymer theories. The modulus behavior above the Poisson's threshold shows a temperature dependence directly proportional to the temperature dependence of the spring constants of particle interactions. We know that the spring constants of particle interactions in real systems decreases as temperature increases causing a softening however a combination of entropic hardening and enthalpic softening at the Poisson's threshold offers interesting possibilities.

This is a question that can be readily answered by running modulus experiments at higher temperatures and is part of the outlook for this project.

6.8 Figures

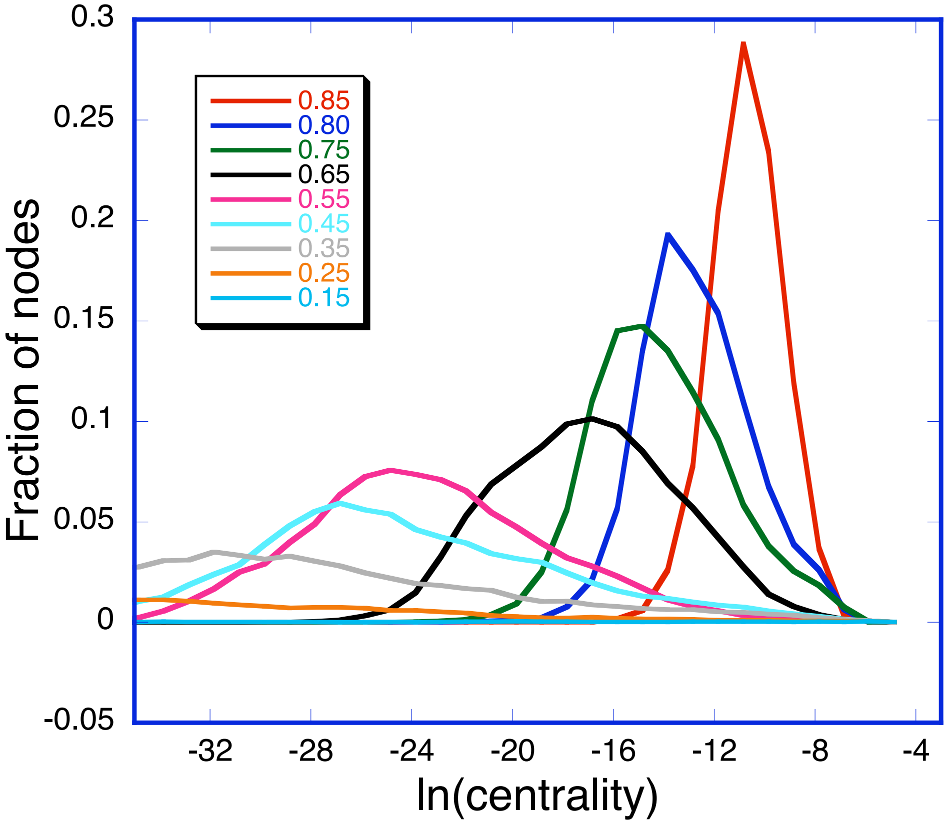

Figure 6.1: Eigenvector centrality measured by the magnitude of the cardinal eigenvector coefficient or eigenvector centrality value for ROMP networks. The x-axis is the natural log of the centrality value and the y-axis is the fraction of nodes with that value. Each curve shows the centrality distribution for a different degree of reaction.

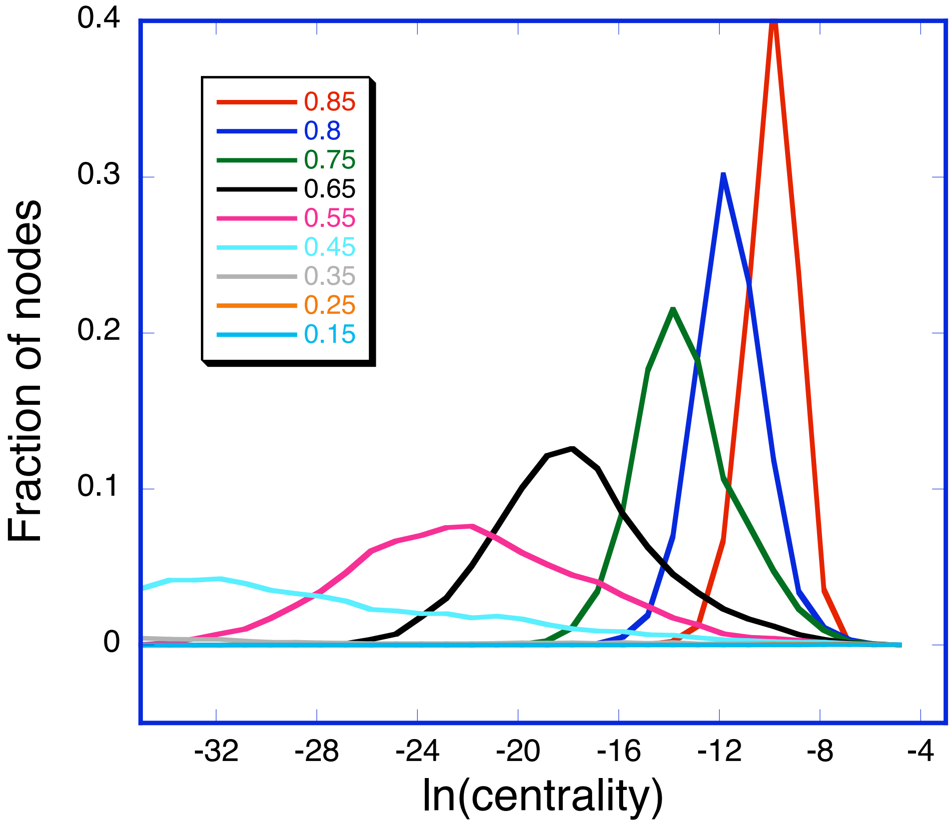

Figure 6.2: Eigenvector centrality measured by the magnitude of the cardinal eigenvector coefficient or eigenvector centrality value for RANDOM networks. The x-axis is the natural log of the centrality value and the y-axis is the fraction of nodes with that value. Each curve shows the centrality distribution for a different degree of reaction.

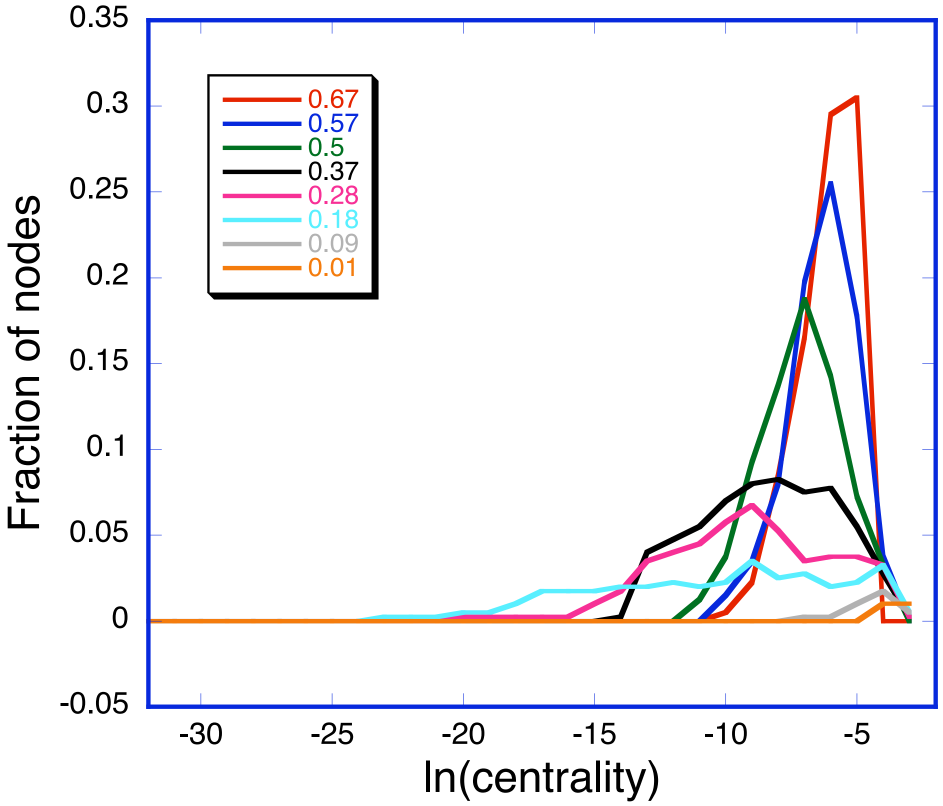

Figure 6.3: Eigenvector centrality measured by the magnitude of the cardinal eigenvector coefficient or eigenvector centrality value for Atomistic-COM networks. The x-axis is the natural log of the centrality value and the y-axis is the fraction of nodes with that value. Each curve shows the centrality distribution for a different degree of reaction.

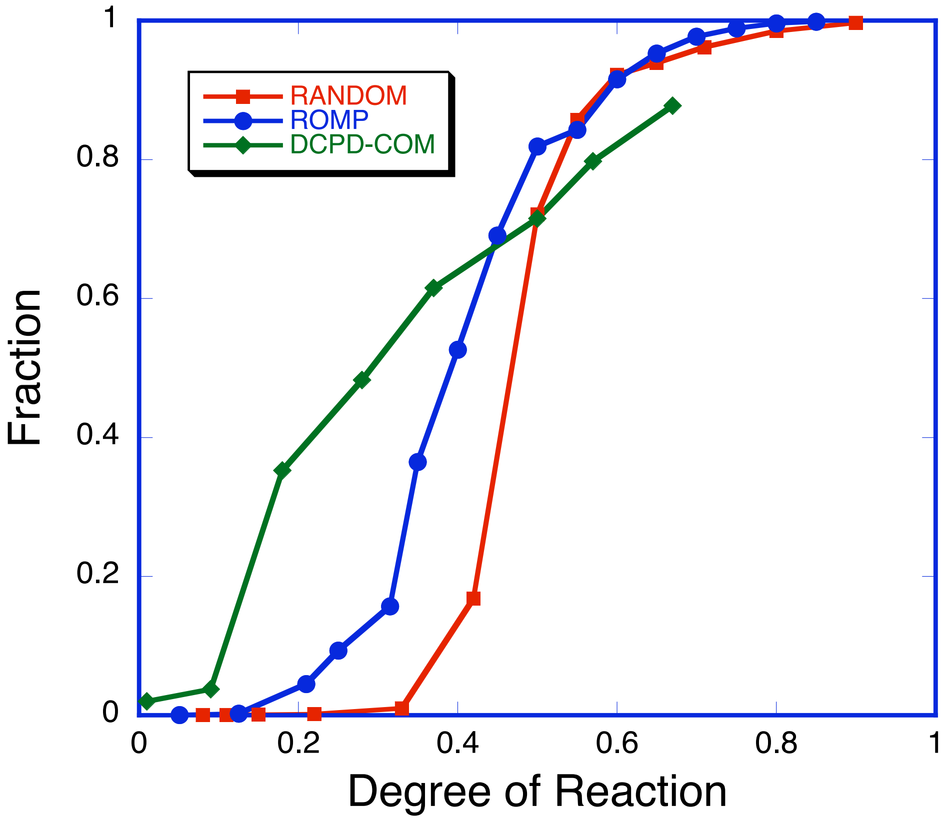

Figure 6.4: Fraction of nodes with high centrality or high eigenvector coefficients (i.e. centrality value >10^{-30}). This cutoff value was chosen since it is equivalent to machine precison. The graphs approximately show the fraction of nodes that are connected to the giant component.

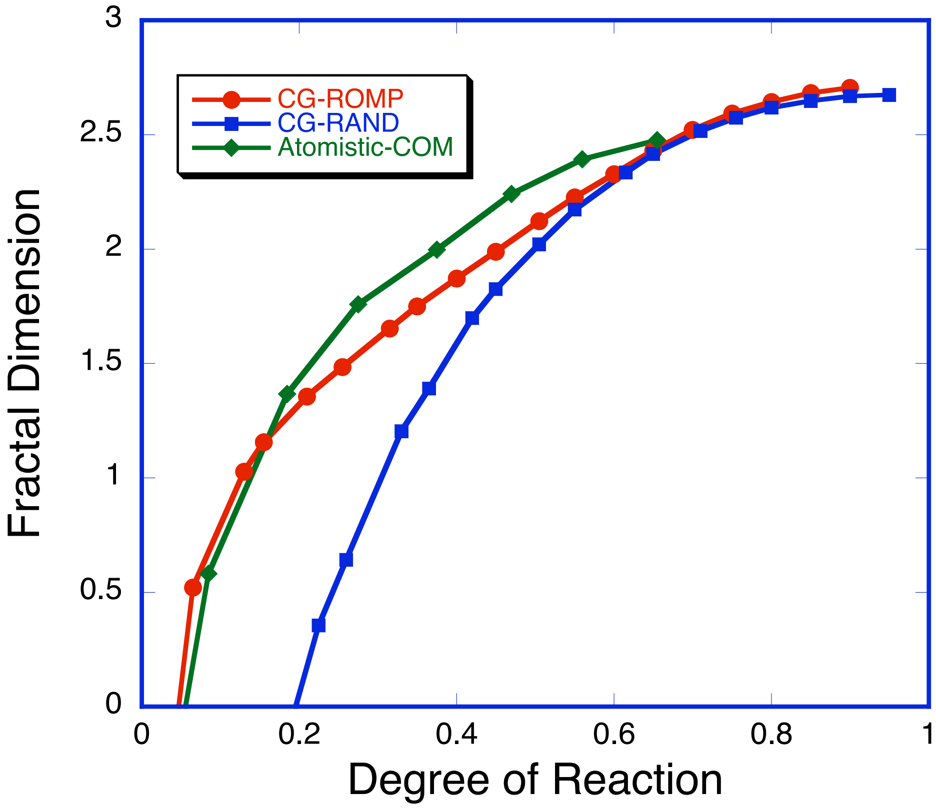

Figure 6.5: Graph fractal dimension. There are significant differences in the ROMP and RANDOM CG models fractal dimension at low degrees of reaction that later converges at high degrees of reaction. The atomistic center of mass fractal dimension is calculated by considering each molecule as a node connected to other molecules and not as individual atoms. The Atomistic-COM corresponds to the CG-ROMP curves. Close similarity between CG-ROMP and Atomistic-COM curves is indicative that they both create similar networks, however we find significant differences in curves at $\alpha>0.15$.

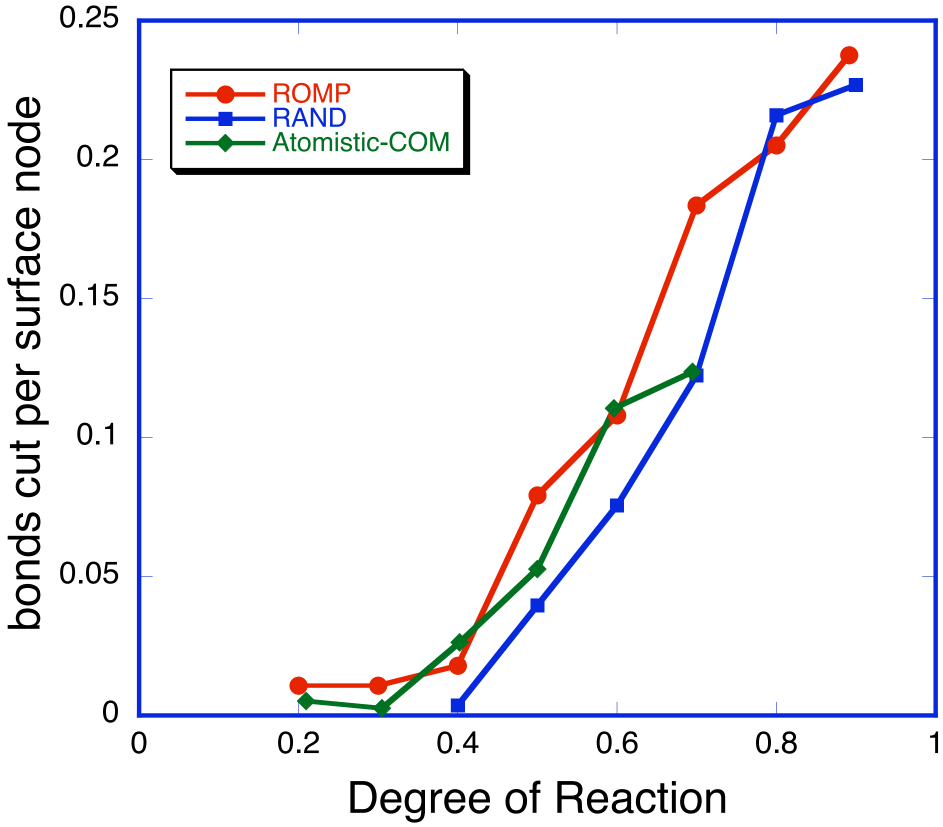

Figure 6.6: Fiedler partitioning cut bonds per unit surface node.

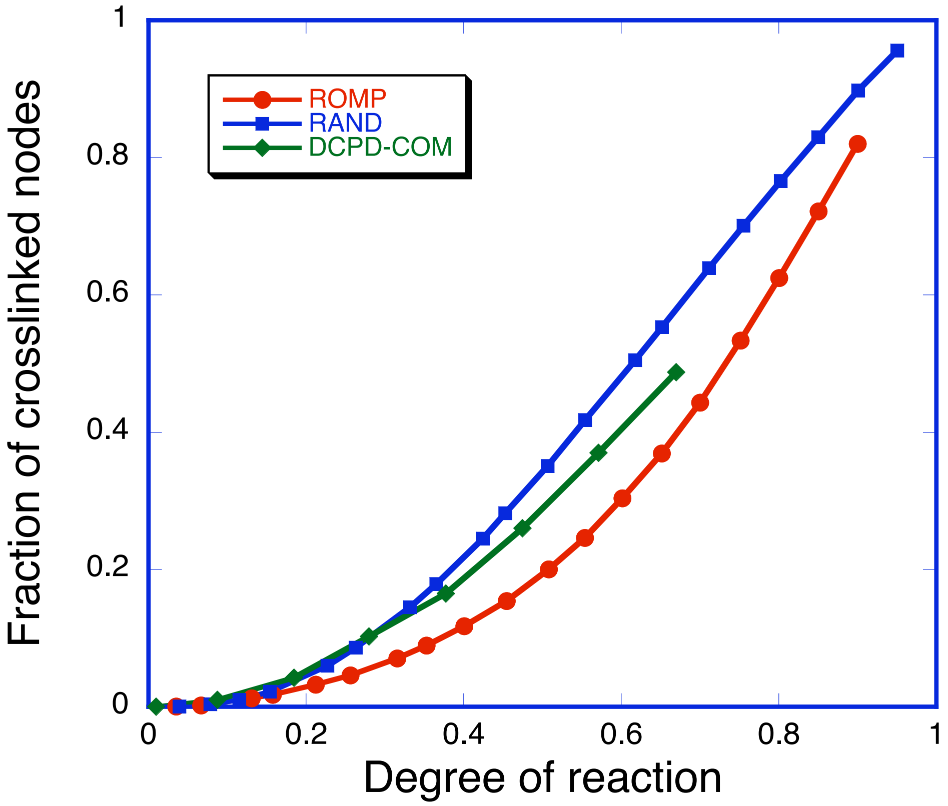

Figure 6.7: Fraction of cross-linked nodes in ROMP, RANDOM and atomistic-COM systems.

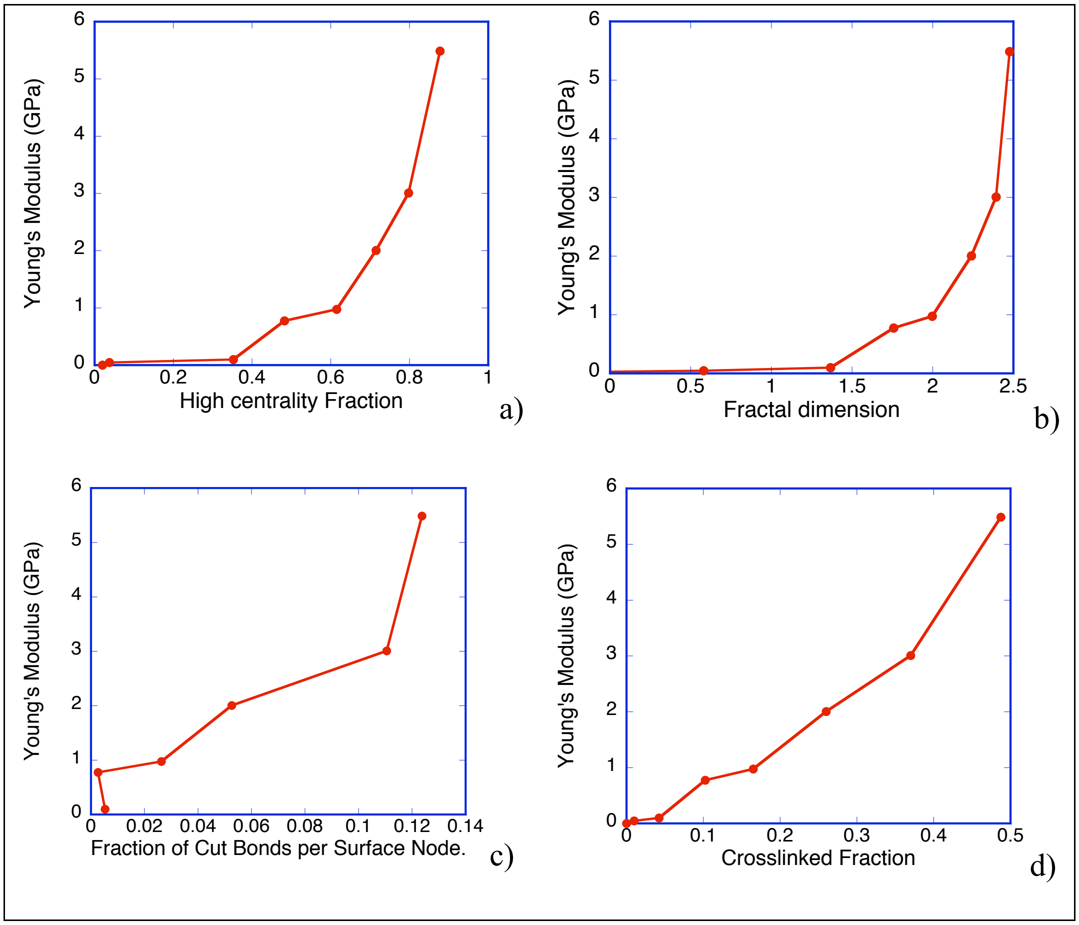

Figure 6.8: Young's modulus of atomistic networks plotted against calculated network measures a) high eigenvector centrality fraction b) graph fractal dimension c) Fiedler partitioning fraction per surface node d) crosslink fraction

6.9 References

1. Kieffer, J. & Angell, C. A. Generation of Fractal Silicas by Negative Pressure Rupturing of SiO_2 Glass. *Molecular Simulation* **3**, 137 (1989).
2. Kieffer, J. & Angell, C. A. Structural Incompatibilities and Liquid Phase Separation in Molten Binary Silicates: A Computer Simulation. *J. Chem. Phys* **90**, 4982 (1988).
3. Shanker, O. Defining dimension of a complex network. *Modern Physics Letters B* **21**, 321-326 (2007).
4. Sibsankar Kundu, Dan C. Sorensen, George N. Phillips, Jr. Automatic domain decomposition of proteins by a Gaussian Network Model. *Proteins: Structure, Function, and Bioinformatics* **57**, 725-733 (2004).
5. Flory, P. J. & Erman, B. Theory of elasticity of polymer networks. 3. *Macromolecules* **15**, 800-806 (1982).

Chapter 7
Summary and Outlook

Our investigation on cross-linked polymers have brought together for the much clarity to ROMP catalyzed DCPD networks.

We use DFT calculations in Chapter 2 to clarify the ROMP cross-linking process in DCPD. To the best of our knowledge this work is the first to quantify the heat of reactions for the ROMP of DCPD. In doing so we were able to explain the observed kinetic phenomena in experiments. Based on these results we propose endo-DCPD is likely to form linear chains and exo-DCPD is more likely to form cross-links via the ROMP mechanism.

In Chapter 3 we compare networks formed by ROMP process to networks created by RANDOM insertion of bonds. We find significant differences in mechanical properties based on internal topology at similar degrees of reaction. This is a nuance yet unappreciated in literature where all networks at a given degree of reaction are expected to have similar properties. Significantly, we discover a novel delineation of networks in to three different phases based on their degree of cure, characterized by their response to deformation. We show that percolation phenomena in networks exhibit two distinct thresholds instead of the commonly assumed single threshold. We term them a) Young's modulus threshold (α_Y) and b) Poisson's ratio threshold (α_P) where $\alpha_Y < \alpha_P$. In region 1 for degree of cure below α_Y the network is fluid-like. At degrees of cure between α_Y and α_P the network exhibits a predominantly entropic response to deformation and is rubber-like. Finally above α_P the network shows an enthalpic response. Region 1 being fluid like shows zero modulus and exhibits only viscous behavior, region 2 shows rubber like response to small deformations, where the volume and internal energy do not change, yet there is an observed Young's modulus. The origin of this modulus is entropic in nature and well explained by polymer statistical mechanics. It is only in region 3 where small deformation actually strains bonds and other potential interactions. It is only in this region do we see a change in internal energy and volume. We term this as enthalpic response. In this chapter we also show a simple scaling procedure applicable to any network with a degree of cure below α_P. This procedure is used to convert the coarse grained results into real units for comparison with atomistic simulations. CG simulations also directed parameterization of reactions for our atomistic simulations helping us define a reaction cutoff.

In Chapter 4 we create atomistic models of DCPD networks using a novel reactive MD scheme. The creation procedure closely implements intuition gained from DFT calculations, CG simulations, and experimental observations from literature. We report for the first time mechanical properties (Young's modulus, Poisson's ratio and Bulk modulus) of DCPD networks at various degrees of cure and delineate the α_Y and α_P thresholds for this system. Our atomistic simulations reinforce the results obtained by CG simulations by closely reproducing the two thresholds along with reaction kinetics. The created networks are now available for further investigation of properties such as diffusion etc.

Chapter 5 is a comparison of our network generation results with experimental observations from DSC and Raman spectroscopy. We combine results obtained from

Reactive MD simulations from Chapter 4 and DFT data from Chapter 2. This attempt shows a procedure to systematically approach this question. The DCPD network generated are ultimately only as good as the assumptions made while creating them. There are still unanswered questions that affect the evolution of network structure such as the effect of ROMP reaction on one site affecting reactivity of ROMP on the other site in DPCD. Regardless we were able to replicate key features of experimental observations.

Chapter 6 is an attempt to characterize networks using novel graph theory concepts. We explored four different characteristics 1) Eigenvector centrality, 2) Graph fractal dimension 3) Fiedler partitioning 4) Fraction of cross-linked nodes. From initial observations we propose the Fiedler partitioning measure as the best candidate for predicting mechanical properties based on its high correlation with our modulus results. An important question that remains unanswered is the formulation of characterization tools that pinpoint the onset of the two observed thresholds in modulus behavior. This effort is part of the future outlook.

Appendix A: Topology and COMPASS Parameters

A.1: Molecular Topology

A.1.1: Atom Types

Type	Atom
1	${}_{sp3}C_{H}$
2	${}_{sp2}C$
3	${}_{sp3}C_{H_2}$
4	H

A.1.2: Bond Topology

Bond Type	Atom1	Atom2
1	1	1
2	1	3
3	1	4
4	1	2
5	2	2
6	2	4
7	3	4
8	2	3
9	2	2
10	2	2

A.1.3: Angle Topology

Angle Type	Atom1	Atom2	Atom3
1	1	1	1
2	1	1	3
3	1	1	4
4	3	1	4
5	1	1	2
6	2	1	3
7	2	1	4
8	1	2	2
9	1	2	4
10	2	2	4
11	1	3	1
12	1	3	4
13	4	3	4
14	1	3	2
15	2	3	4
16	2	2	3
17	3	2	4
18	4	2	4

A.1.5: Improper Topology

Improper Type	Atom1	Atom2	Atom3	Atom4
1	1	2	2	4
2	2	2	3	4
3	1	1	1	3
4	1	1	1	4
5	1	1	3	4
6	1	1	2	3
7	1	1	2	4
8	2	1	3	4
9	1	1	1	2
10	1	3	1	4
11	1	3	4	4
12	1	3	2	4
13	2	3	4	4
14	4	2	2	4

A.1.4: Dihedral Topology

Dihedral Type	Atom 1	Atom 2	Atom 3	Atom 4
1	1	1	1	2
2	1	1	1	3
3	1	1	1	4
4	2	1	1	3
5	3	1	1	3
6	3	1	1	4
7	2	1	1	4
8	4	1	1	4
9	1	1	1	1
10	1	1	3	2
11	1	1	3	4
12	4	1	3	2
13	4	1	3	4
14	1	1	2	2
15	1	1	2	4
16	3	1	2	2
17	3	1	2	4
18	4	1	2	2
19	4	1	2	4
20	2	1	3	1
21	2	1	3	4
22	1	1	3	1
23	4	1	3	1
24	1	2	2	1
25	1	2	2	4
26	4	2	2	4
27	2	1	1	2
28	2	2	3	1
29	4	2	3	1
30	2	2	3	4
31	4	2	3	4
32	1	2	2	3
33	3	2	2	4
34	3	2	2	3

A.2: Interaction Parameters

A.2.1: Pair and Coulomb Interaction Parameters

$$E_{pair} = \varepsilon\left(2\frac{\sigma^9}{r^9} - 3\frac{\sigma^6}{r^6}\right),\ E_{coul} = \frac{Kq_1q_2}{r^2}$$

Type	$\varepsilon(Kcal/Mol)$	$\sigma(A^o)$	$q(e)$	Comments for charge
1	0.054000	4.0100	0.0 or -0.1	0.0 if connected to a type 2
2	0.064000	4.0100	-0.2	
3	0.054000	4.0100	-0.2 or -0.1	-0.1 if connected to a type 2
4	0.020000	2.9950	0.1	

A.2.2: Bond Interaction Parameters

$$E_{bond} = k_2(r - r_o)^2 + k_3(r - r_o)^3 + k_4(r - r_o)^4$$

Type	$r_0(A^o)$	$K_1[kcal/(mol \times (A^o)^2)]$	K_2	K_3
1	1.5330	299.67	-501.77	679.81
2	1.5330	299.67	-501.77	679.81
3	1.1010	341.00	-691.89	844.60
4	1.5060	312.35	-582.19	339.90
5	1.3521	545.27	-1005.6	1225.7
6	1.0883	365.77	-725.54	781.66
7	1.1010	341.00	-691.89	844.60
8	1.5060	312.35	-582.19	339.90
9	1.3521	545.27	-1005.6	1225.7
10	1.3521	545.27	-1005.6	1225.7

A2.3: Angle Interaction Parameters: $E_{angle} = E_a + E_{bb} + E_{ab}$

$$E_a = K_2(\theta - \theta_o)^2 + K_3(\theta - \theta_o)^3 + K_4(\theta - \theta_o)^4$$

Type	θ_o(deg)	$K_2[(kcal/mol)/rad^2]$	K_3	K_4
1	112.67	39.516	-7.4430	-9.5583
2	112.67	39.516	-7.4430	-9.5583
3	110.77	41.453	-10.604	5.1290
4	110.77	41.453	-10.604	5.1290
5	111.76	45.703	-10.640	-9.9121
6	111.76	45.703	-10.640	-9.9121
7	110.06	41.278	-14.296	-5.2229
8	126.26	43.825	-27.727	1.0056
9	117.27	30.094	-8.0826	-8.6781
10	124.88	35.277	-17.774	-1.6215
11	112.67	39.516	-7.4430	-9.5583
12	110.77	41.453	-10.604	5.1290
13	107.66	39.641	-12.921	-2.4318
14	111.76	45.703	-10.640	-9.9121
15	110.06	41.278	-14.296	5.2229
16	126.26	43.825	-27.727	1.0056
17	117.27	30.094	-8.0826	-8.6781
18	117.27	30.094	-8.0826	-8.6781

$E_{bb} = M(r_1 - r_{ij})(r_2 - r_{jk})$

Type	$M[kcal/(mol \times (A^o)^2)]$	$r_1(A^o)$	$r_2(A^o)$
1	0.0000	1.5330	1.5330
2	0.0000	1.5330	1.5330
3	3.3872	1.5330	1.1010
4	3.3872	1.5330	1.1010
5	7.7827	1.5330	1.5060
6	7.7827	1.5060	1.5330
7	9.9922	1.5060	1.1010
8	17.791	1.5060	1.3521
9	3.4394	1.5060	1.0883
10	10.105	1.3521	1.0883
11	0.0000	1.5330	1.5330
12	3.3872	1.5330	1.1010
13	5.3316	1.1010	1.1010
14	7.7827	1.5330	1.5060
15	9.9922	1.5060	1.1010
16	17.791	1.3521	1.5060
17	3.4394	1.5060	1.0883
18	3.4394	1.5060	1.0883

$$E_{ab} = -[N_1(r_1 - r_{ij}) + N_2(r_2 - r_{jk})](\theta - \theta_o)$$

Type	$N_1[kcal/mol/A^o/rad]$	$N_2[kcal/mol/A^o/rad]$	$r_1(A^o)$	$r_2(A^o)$
1	8.0160	8.0160	1.5330	1.5330
2	8.0160	8.0160	1.5330	1.5330
3	20.754	11.421	1.5330	1.1010
4	20.754	11.421	1.5330	1.1010
5	15.982	18.978	1.5330	1.5060
6	18.978	15.982	1.5060	1.5330
7	20.877	14.274	1.5060	1.1010
8	31.588	24.225	1.5060	1.3521
9	17.645	15.349	1.5060	1.0883
10	23.359	19.059	1.3521	1.0883
11	8.0160	8.0160	1.5330	1.5330
12	20.754	11.421	1.5330	1.1010
13	18.103	18.103	1.1010	1.1010
14	15.982	18.978	1.5330	1.5060
15	20.877	14.274	1.5060	1.1010
16	24.225	31.588	1.3521	1.5060
17	17.645	15.349	1.5060	1.0883
18	17.645	15.349	1.5060	1.0883

A2.4: Dihedral Interaction Parameters:

$$E_{dihed} = E_d + E_{mbt} + E_{ebt} + E_{at} + E_{aat} + E_{bb13} \text{ and } E_d = \sum_{n=1}^{3} D_j\left[1 - \cos(n\phi - \phi_n)\right]$$

Type	$D_1(kcal/mol)$	ϕ(deg)	$D_2(kcal/mol)$	ϕ(deg)	$D_3(kcal/mol)$	ϕ(deg)
1	0.088300	0.0000	0.0000	0.0000	-0.019800	0.0000
2	0.12230	0.0000	0.051400	0.0000	-0.22300	0.0000
3	0.0000	0.0000	0.031600	0.0000	-0.17810	0.0000
4	0.088300	0.0000	0.0000	0.0000	-0.019800	0.0000
5	0.12230	0.0000	0.051400	0.0000	-0.22300	0.0000
6	0.0000	0.0000	0.031600	0.0000	-0.17810	0.0000
7	0.0000	0.0000	0.0000	0.0000	-0.11660	0.0000
8	-0.24320	0.0000	0.061700	0.0000	-0.13830	0.0000
9	0.12230	0.0000	0.051400	0.0000	-0.22300	0.0000
10	0.088300	0.0000	0.0000	0.0000	-0.019800	0.0000
11	0.0000	0.0000	0.031600	0.0000	-0.17810	0.0000
12	0.0000	0.0000	0.0000	0.0000	-0.11660	0.0000
13	-0.24320	0.0000	0.061700	0.0000	-0.13830	0.0000
14	-0.24330	0.0000	0.0000	0.0000	0.10400	0.0000
15	-0.24330	0.0000	0.0000	0.0000	-0.32810	0.0000
16	0.24330	0.0000	0.0000	0.0000	0.10400	0.0000
17	-0.24330	0.0000	0.0000	0.0000	-0.32810	0.0000
18	0.11430	0.0000	0.0000	0.0000	0.18540	0.0000
19	-0.11430	0.0000	0.0000	0.0000	-0.13490	0.0000
20	0.088300	0.0000	0.0000	0.0000	-0.019800	0.0000
21	0.0000	0.0000	0.0000	0.0000	-0.11660	0.0000
22	0.12230	0.0000	0.051400	0.0000	-0.22300	0.0000
23	0.0000	0.0000	0.031600	0.0000	-0.17810	0.0000
24	0.086000	0.0000	5.1995	0.0000	0.0000	0.0000
25	0.0000	0.0000	5.2097	0.0000	0.0000	0.0000
26	0.0000	0.0000	4.8974	0.0000	0.0000	0.0000
27	0.0000	0.0000	0.0000	0.0000	-0.31600	0.0000
28	0.24330	0.0000	0.0000	0.0000	0.10400	0.0000
29	-0.24330	0.0000	0.0000	0.0000	-0.32810	0.0000
30	0.11430	0.0000	0.0000	0.0000	0.18540	0.0000
31	-0.11430	0.0000	0.0000	0.0000	-0.13490	0.0000
32	0.086000	0.0000	5.1995	0.0000	0.0000	0.0000
33	0.0000	0.0000	5.2097	0.0000	0.0000	0.0000
34	0.0000	0.0000	5.2097	0.0000	0.0000	0.0000

$$E_{aat} = M(\theta_{ijk} - \theta_1)(\theta_{jkl} - \theta_2)\cos(\phi)$$

Type	$M(kcal/mol)$	θ_1(deg)	θ_2(deg)
1	-27.913	112.67	111.76
2	-22.045	112.67	112.67
3	-16.164	112.67	110.77
4	-27.913	111.76	112.67
5	-22.045	112.67	112.67
6	-16.164	112.67	110.77
7	-18.372	111.76	110.77
8	-12.564	110.77	110.77
9	-22.045	112.67	112.67
10	-27.913	112.67	111.76
11	-16.164	112.67	110.77
12	-18.372	110.77	111.76
13	-12.564	110.77	110.77
14	-20.371	111.76	126.26
15	-16.899	111.76	117.27
16	-20.371	111.76	126.26
17	-16.899	111.76	117.27
18	-13.683	110.06	126.26
19	-10.951	110.06	117.27
20	-27.913	111.76	112.67
21	-18.372	111.76	110.77
22	-22.045	112.67	112.67
23	-16.164	110.77	112.67
24	-5.5205	126.26	126.26
25	-7.6912	126.26	124.88
26	-7.0058	124.88	124.88
27	-9.6558	111.76	111.76
28	-20.371	126.26	111.76
29	-16.899	117.27	111.76
30	-13.683	126.26	110.06
31	-10.951	117.27	110.06
32	-5.5205	126.26	126.26
33	-7.6912	126.26	124.88
34	-7.6912	126.26	124.88

$$E_{ebt} = \begin{bmatrix} (r_{ij} - r_1)\left[B_1\cos(\phi) + B_2\cos(2\phi) + B_3\cos(3\phi)\right] + \\ (r_{kl} - r_3)\left[C_1\cos(\phi) + C_2\cos(2\phi) + C_3\cos(3\phi)\right] \end{bmatrix}$$

Type	B_1	B_2	B_3	C_1	C_2	C_3	r_1	r_3
1	-0.6028	0.0000	0.7675	1.0356	0.0000	0.0506	1.5330	1.5060
2	-0.0732	0.0000	0.0000	-0.0732	0.0000	0.0000	1.5330	1.5330
3	0.2486	0.2422	-0.0925	0.0814	0.0591	0.2219	1.5330	1.1010
4	1.0356	0.0000	0.0506	-0.6028	0.0000	0.7675	1.5060	1.5330
5	-0.0732	0.0000	0.0000	-0.0732	0.0000	0.0000	1.5330	1.5330
6	0.2486	0.2422	-0.0925	0.0814	0.0591	0.2219	1.5330	1.1010
7	0.9856	0.0000	-0.0864	0.1954	0.0000	-0.0871	1.5060	1.1010
8	0.2130	0.3120	0.0777	0.2130	0.312	0.0777	1.1010	1.1010
9	-0.0732	0.0000	0.0000	-0.0732	0.0000	0.0000	1.5330	1.5330
10	-0.6028	0.0000	0.7675	1.0356	0.0000	0.0506	1.5330	1.5060
11	0.2486	0.2422	-0.0925	0.0814	0.0591	0.2219	1.5330	1.1010
12	0.1954	0.0000	-0.0871	0.9856	0.0000	-0.0864	1.1010	1.5060
13	0.2130	0.3120	0.0777	0.2130	0.3120	0.0777	1.1010	1.1010
14	0.1159	0.0000	-0.8513	-0.6486	0.0000	0.8394	1.5330	1.3521
15	0.1852	0.0000	0.5906	1.1730	0.0000	-0.0582	1.5330	1.0883
16	0.1159	0.0000	-0.8513	-0.6486	0.0000	0.8394	1.5330	1.3521
17	0.1852	0.0000	0.5906	1.1730	0.0000	-0.0582	1.5330	1.0883
18	1.9787	0.0000	-0.1805	0.8566	0.0000	0.0811	1.1010	1.3521
19	0.2212	0.0000	0.0915	0.5934	0.0000	0.0424	1.1010	1.0883
20	1.0356	0.0000	0.0506	-0.6028	0.0000	0.7675	1.5060	1.5330
21	0.9856	0.0000	-0.0864	0.1954	0.0000	-0.0871	1.5060	1.1010
22	-0.0732	0.0000	0.0000	-0.0732	0.0000	0.0000	1.5330	1.5330
23	0.0814	0.0591	0.2219	0.2486	0.2422	-0.0925	1.1010	1.5330
24	-0.5916	0.0000	-0.5440	-0.5916	0.0000	-0.5440	1.5060	1.5060
25	-0.2201	0.6770	0.0000	0.5406	-0.1611	0.0000	1.5060	1.0883
26	0.7129	0.5161	0.0000	0.7129	0.5161	0.0000	1.0883	1.0883
27	1.0166	0.0000	0.0446	1.0166	0.0000	0.0446	1.5060	1.5060
28	-0.6486	0.0000	-0.8394	0.1159	0.0000	-0.8513	1.3521	1.5330
29	1.1730	0.0000	-0.0582	0.1852	0.0000	0.5906	1.0883	1.5330
30	0.8566	0.0000	0.0811	1.9787	0.0000	-0.1805	1.3521	1.1010
31	0.5934	0.0000	0.0424	0.2212	0.0000	0.0915	1.0883	1.1010
32	-0.5916	0.0000	-0.5440	-0.5916	0.0000	-0.544	1.5060	1.5060
33	-0.2201	0.6770	0.0000	0.5406	-0.1611	0.0000	1.5060	1.0883
34	-0.2201	0.6770	0.0000	0.5406	-0.1611	0.0000	1.5060	1.0883

$$E_{mbt} = (r_{jk} - r_2)\left[A_1 \cos(\phi) + A_2 \cos(2\phi) + A_3 \cos(3\phi)\right]$$

Type	A_1(kcal/mol.Å)	A_2	A_3	r_2
1	-2.2408	0.0000	-5.4870	1.5330
2	-17.787	-7.1877	0.0000	1.5330
3	-14.879	-3.6581	-0.3138	1.5330
4	-2.2408	0.0000	-5.487	1.5330
5	-17.787	-7.1877	0.0000	1.5330
6	-14.879	-3.6581	-0.3138	1.5330
7	-5.0113	0.0000	0.58950	1.5330
8	-14.261	-0.5322	-0.4864	1.5330
9	-17.787	-7.1877	0.0000	1.5330
10	-2.2408	0.0000	-5.4870	1.5330
11	-14.879	-3.6581	-0.3138	1.5330
12	-5.0113	0.0000	0.58950	1.5330
13	-14.261	-0.5322	-0.4864	1.5330
14	-2.1444	0.0000	-0.1038	1.5060
15	1.2814	0.0000	-1.1022	1.5060
16	-2.1444	0.0000	-0.1038	1.5060
17	1.2814	0.0000	-1.1022	1.5060
18	-1.5727	0.0000	0.65650	1.5060
19	1.8730	0.0000	-0.3702	1.5060
20	-2.2408	0.0000	-5.4870	1.5330
21	-5.0113	0.0000	0.58950	1.5330
22	-17.787	-7.1877	0.0000	1.5330
23	-14.879	-3.6581	-0.3138	1.5330
24	-0.18990	5.5768	0.0000	1.3521
25	1.1220	6.0669	0.0000	1.3521
26	-0.85580	6.3911	0.0000	1.3521
27	-0.35460	0.0000	0.04830	1.5330
28	-2.1444	0.0000	-0.1038	1.5060
29	1.2814	0.0000	-1.1022	1.5060
30	-1.5727	0.0000	0.65650	1.5060
31	1.8730	0.0000	-0.3702	1.5060
32	-0.18990	5.5768	0.0000	1.3521
33	1.1220	6.0669	0.0000	1.3521
34	1.1220	6.0669	0.0000	1.3521

$$E_{bb13} = N(r_{ij} - r_1)(r_{kl} - r_3)$$

Type	N $\frac{kcal}{mol \times \left(A^o\right)^2}$	$r_1(A^o)$	$r_2(A^o)$
1	0.0000	1.5330	1.5060
2	0.0000	1.5330	1.5330
3	0.0000	1.5330	1.1010
4	0.0000	1.5060	1.5330
5	0.0000	1.5330	1.5330
6	0.0000	1.5330	1.1010
7	0.0000	1.5060	1.1010
8	0.0000	1.1010	1.1010
9	0.0000	1.5330	1.5330
10	0.0000	1.5330	1.5060
11	0.0000	1.5330	1.1010
12	0.0000	1.1010	1.5060
13	0.0000	1.1010	1.1010
14	0.0000	1.5330	1.3521
15	0.0000	1.5330	1.0883
16	0.0000	1.5330	1.3521
17	0.0000	1.5330	1.0883
18	0.0000	1.1010	1.3521
19	0.0000	1.1010	1.0883
20	0.0000	1.5060	1.5330
21	0.0000	1.5060	1.1010
22	0.0000	1.5330	1.5330
23	0.0000	1.1010	1.5330
24	0.0000	1.5060	1.5060
25	0.0000	1.5060	1.0883
26	0.0000	1.0883	1.0883
27	0.0000	1.5060	1.5060
28	0.0000	1.3521	1.5330
29	0.0000	1.0883	1.5330
30	0.0000	1.3521	1.1010
31	0.0000	1.0883	1.1010
32	0.0000	1.5060	1.5060
33	0.0000	1.5060	1.0883
34	0.0000	1.5060	1.0883

$$E_{at} = \begin{bmatrix} (\theta_{jk} - \theta_1)\left[D_1\cos(\phi) + D_2\cos(2\phi) + D_3\cos(3\phi)\right] + \\ (\theta_{ij} - \theta_2)\left[E_1\cos(\phi) + E_2\cos(2\phi) + E_3\cos(3\phi)\right] \end{bmatrix}$$

Type	D_1	D_2 kcal/mol	D_3	E_1	E_2	E_3	θ_1(deg)	θ_1(deg)
1	2.4027	0.0000	0.0000	1.1559	0.0000	-1.2900	112.6	111.76
2	0.38860	-0.3139	0.13890	0.38860	-0.3139	0.13890	112.6	112.67
3	-0.2454	0.0000	-0.1136	0.31130	0.45160	-0.1988	112.6	110.77
4	1.1559	0.0000	-1.2900	2.4027	0.0000	0.0000	111.7	112.67
5	0.38860	-0.3139	0.1389	0.38860	-0.3139	0.13890	112.6	112.67
6	-0.2454	0.0000	-0.1136	0.31130	0.45160	-0.1988	112.6	110.77
7	0.60830	0.0000	0.0000	-0.8714	0.0000	0.0000	111.7	110.77
8	-0.8085	0.5569	-0.2466	-0.8085	0.55690	-0.2466	110.7	110.77
9	0.38860	-0.3139	0.1389	0.38860	-0.3139	0.13890	112.6	112.67
10	2.4027	0.0000	0.0000	1.1559	0.0000	-1.2900	112.6	111.76
11	-0.2454	0.0000	-0.1136	0.31130	0.45160	-0.1988	112.6	110.77
12	-0.8714	0.0000	0.0000	0.60830	0.0000	0.0000	110.7	111.76
13	-0.8085	0.5569	-0.2466	-0.8085	0.55690	-0.2466	110.7	110.77
14	-0.2409	0.0000	0.38700	-0.1646	0.0000	0.0000	111.7	126.26
15	0.53110	0.0000	0.0000	-0.9172	0.0000	0.0000	111.7	117.27
16	-0.2409	0.0000	0.3870	-0.1646	0.0000	0.0000	111.7	126.26
17	0.53110	0.0000	0.0000	-0.9172	0.0000	0.0000	111.7	117.27
18	1.5982	0.0000	0.0000	-1.8873	0.0000	0.0000	110.0	126.26
19	1.9061	0.0000	0.0000	-0.0677	0.0000	0.0000	110.0	117.27
20	1.1559	0.0000	-1.2900	2.4027	0.0000	0.0000	111.7	112.67
21	0.60830	0.0000	0.0000	-0.8714	0.0000	0.0000	111.7	110.77
22	0.38860	-0.3139	0.13890	0.38860	-0.3139	0.1389	112.6	112.67
23	0.31130	0.4516	-0.1988	-0.2454	0.0000	-0.1136	110.7	112.67
24	-4.3970	2.5810	0.0000	-4.3970	2.5810	0.0000	126.2	126.26
25	-5.4082	1.4731	0.0000	-1.5176	3.7112	0.0000	126.2	124.88
26	-1.8911	3.2540	0.0000	-1.8911	3.2540	0.0000	124.8	124.88
27	-0.4053	0.0000	0.43000	-0.4053	0.0000	0.4300	111.7	111.76
28	-0.1646	0.0000	0.0000	-0.2409	0.0000	0.3870	126.2	111.76
29	-0.9172	0.0000	0.0000	0.53110	0.0000	0.0000	117.2	111.76
30	-1.8873	0.0000	0.0000	1.5982	0.0000	0.0000	126.2	110.06
31	-0.0677	0.0000	0.0000	1.9061	0.0000	0.0000	117.2	110.06
32	-4.3970	2.5810	0.0000	-4.3970	2.5810	0.0000	126.2	126.26
33	-5.4082	1.4731	0.0000	-1.5176	3.7112	0.0000	126.2	124.88
34	-5.4082	1.4731	0.0000	-1.5176	3.7112	0.0000	126.2	124.88

A2.5: Improper Interaction Parameters: $E_{improper} = E_i + E_{aa}$

$$E_i = K\left[\frac{\chi_{ijkl} + \chi_{kjli} + \chi_{ljik}}{3} - \chi_o\right]^2 \text{ and } E_{aa} = \begin{bmatrix} M_1(\theta_{ijk} - \theta_1)(\theta_{kjl} - \theta_3) + \\ M_2(\theta_{ijk} - \theta_1)(\theta_{ijl} - \theta_2) + \\ M_3(\theta_{ijl} - \theta_2)(\theta_{kjl} - \theta_3) \end{bmatrix}$$

Type	$K(kcal/mol)$	χ_o
1	2.0765	0.0000
2	2.0765	0.0000
3	0.0000	0.0000
4	0.0000	0.0000
5	0.0000	0.0000
6	0.0000	0.0000
7	0.0000	0.0000
8	0.0000	0.0000
9	0.0000	0.0000
10	0.0000	0.0000
11	0.0000	0.0000
12	0.0000	0.0000
13	0.0000	0.0000
14	2.0765	0.0000

Type	$M_1(kcal/mol)$	M_1	M_1	θ_1(deg)	θ_2(deg)	θ_3(deg)
1	0.0000	0.0000	0.0000	126.26	124.88	117.27
2	0.0000	0.0000	0.0000	126.26	117.27	124.88
3	-0.17290	-0.17290	-0.17290	112.67	112.67	112.67
4	-1.3199	-1.3199	0.11840	112.67	110.77	110.77
5	-1.3199	-1.3199	0.11840	112.67	110.77	110.77
6	0.0000	0.0000	0.0000	111.76	111.76	112.67
7	0.97470	-1.4639	4.1941	111.76	110.06	110.77
8	-1.4639	0.97470	4.1941	111.76	110.77	110.06
9	0.0000	0.0000	0.0000	112.67	111.76	111.76
10	-1.3199	-1.3199	0.11840	112.67	110.77	110.77
11	0.27380	-0.48250	0.27380	110.77	107.66	110.77
12	0.97470	-1.4639	4.1941	111.76	110.06	110.77
13	-0.11410	-8.2464	-0.11410	110.06	107.66	110.06
14	0.0000	0.0000	0.0000	126.26	124.88	117.27

Appendix B: Atomistic Network Generation Code

This is a perl script that takes the xyz coordinates of atoms in xyzfile, the bonding information from the bndfile along with a topologyfile type2topoinfofile to exchange the bonding in DCPD. The reaction distance is typically adjusted to get reasonable reaction rates and has to be chosen carefully to get valid results. A low value results in almost no reactions and a high value results in high strain at large degrees of reaction. The program header show required files for the reaction code to run. It can be modified to change atom types also although here it only changes bonding topology. A sample topoinfo file is shown after the code that is designed for ROMP in DCPD.

```
# this program reads a timestep bndfile xyzfile and type2topoinfo file
and creates a new lammps input file
# mech.txt that can be used to start off a new simulation
# this program creates bondlist anglelist dihedrallist improperlist
from just the bonding and atomtype data
# This program requires a file called coeff.txt that lists all the
bond, angle,dihedral,improper coeffs in a simulation
# each angletype/dihedral/improper is uniquely determined by the type
of its constituents
# the type2topoinfofile gives this information and has to be created
before this script can be used
# if a given topology type is not mentioned in the topology file  then
the output of the dihderal/angle/improper type is "NA" and cannot be
run.

# created May 4th 2007

$argc= @ARGV;
$argc == 6 || $argc ==7 || die " enter: timestep bndfile xyzfile
type2topoinfofile rxnbondtype rxndistance (finalbondtype)\n";
$snapnum = $ARGV[0];

open (BND, "$ARGV[1]");
open (XYZ, "$ARGV[2]");
open (TOPO, "$ARGV[3]");
$rxnbondtype = $ARGV[4];
$sqrxndist = 2*$ARGV[5]*$ARGV[5];
if ($argc ==7) {$finbndtype = $ARGV[6];}

#$atmtypes = 0;
#$bndtypes = 0;
#$angtypes = 0;
#$dihtypes = 0;
#$imptypes = 0;
@bndtypelist = ();
@angtypelist = ();
@dihtypelist = ();
```

```
@imptypelist = ();

$test = 0;
while (<TOPO>){
  if ($test == 0){
    $temp = $_;
    @t =split(" ",$temp);
    if ($t[1] eq "atom"){
      $atmtypes = $t[0];
      $test++;
      print ("atmtypes = $atmtypes\n");
    }
  }
  if ($test == 1){
    $temp = $_;
    @t =split(" ",$temp);
    if ($t[1] eq "bond"){
      $bndtypes = $t[0];
      $test++;
      print ("bndtypes = $bndtypes\n");
    }
  }
  if ($test == 2){
    $temp = $_;
    @t =split(" ",$temp);
    if ($t[1] eq "angle"){
      $angtypes = $t[0];
      $test++;
      print ("angtypes = $angtypes\n");
    }
  }
  if ($test == 3){
    $temp = $_;
    @t =split(" ",$temp);
    if ($t[1] eq "dihedral"){
      $dihtypes = $t[0];
      $test++;
      print ("dihtypes = $dihtypes\n");
    }
  }
  if ($test == 4){
    $temp = $_;
    @t =split(" ",$temp);
    if ($t[1] eq "improper"){
      $imptypes = $t[0];
      $test++;
      print ("imptypes = $imptypes\n");
    }
  }
  # input a list of bondtypes based on atomtypes
  if ($test == 5){
    $temp = $_;
    @t =split(" ",$temp);
    if ($t[0] eq "bndtype"){
      #print ("bndtype\n");
      for ($i=1; $i<=$bndtypes; $i++){
        $temp = <TOPO>;
        @t =split(" ",$temp);
```

```
        $bndtypelist[$t[0]][0] = $t[1];
        $bndtypelist[$t[0]][1] = $t[2];
      }
      $test++;
    }
  }
  # input a list of angletypes based on atomtypes
  if ($test == 6){
    $temp = $_;
    @t =split(" ",$temp);
    if ($t[0] eq "angtype"){
      #print ("angtype\n");
      for ($i=1; $i<=$angtypes; $i++){
        $temp = <TOPO>;
        @t =split(" ",$temp);
        $angtypelist[$t[0]][0] = $t[1];
        $angtypelist[$t[0]][1] = $t[2];
        $angtypelist[$t[0]][2] = $t[3];
      }
      $test++;
    }
  }
  # input a list of dihedraltypes based on atomtypes
  if ($test == 7){
    $temp = $_;
    @t =split(" ",$temp);
    if ($t[0] eq "dihtype"){
      #print ("dihtype\n");
      for ($i=1; $i<=$dihtypes; $i++){
        $temp = <TOPO>;
        @t =split(" ",$temp);
        $dihtypelist[$t[0]][0] = $t[1];
        $dihtypelist[$t[0]][1] = $t[2];
        $dihtypelist[$t[0]][2] = $t[3];
        $dihtypelist[$t[0]][3] = $t[4];
      }
      $test++;
    }
  }
  if ($test == 8){
    $temp = $_;
    @t =split(" ",$temp);
    if ($t[0] eq "imptype"){
      #print ("imptype\n");
      for ($i=1; $i<=$imptypes; $i++){
        $temp = <TOPO>;
        @t =split(" ",$temp);
        $imptypelist[$t[0]][0] = $t[1];
        $imptypelist[$t[0]][1] = $t[2];
        $imptypelist[$t[0]][2] = $t[3];
        $imptypelist[$t[0]][3] = $t[4];
        #print
("$t[0],$imptypelist[$t[0]][0],$imptypelist[$t[0]][1],$imptypelist[$t[0
]][2],$imptypelist[$t[0]][3]\n");
      }
      $test++;
    }
  }
```

```
}
print ("finished topofile reading\n");

# we just finished getting all the data about the what atom types  make
bond, angle and dihedral and improper type


# we now start getting information about atom positions and box size
etc etc
$numatoms =0;
$numbnd=0;
$numang=0;
$numdih=0;
$numimp=0;

$test = 0;
while (<XYZ>){
  if ($test == 0){
    $temp = $_;
    @t = split (" ", $temp);
    if ($t[1] eq "TIMESTEP"){
      $temp = <XYZ>;
      @t = split (" ", $temp);
      if ($t[0]==$snapnum){
        $test =1;
      }
    }
    if ($test == 1){
      $temp =<XYZ>; # skip line ITEM: NUMBER OF ATOM
      $temp = <XYZ>;
      @t = split (" ", $temp);
      $numatoms = $t[0];
      <XYZ>; #skip line ITEM: BOX BOUNDS
      $temp = <XYZ>;
      @t = split (" ", $temp);
      $xboxmin = round($t[0]);
      $xboxmax = round($t[1]);
      $xbox = $xboxmax-$xboxmin;
      $temp = <XYZ>;
      @t = split (" ", $temp);
      $yboxmin = round($t[0]);
      $yboxmax = round($t[1]);
      $ybox = $yboxmax-$yboxmin;
      $temp = <XYZ>;
      @t = split (" ", $temp);
      $zboxmin = round($t[0]);
      $zboxmax = round($t[1]);
      $zbox = $zboxmax-$zboxmin;
      <XYZ>; # skip line ITEM: ATOMS
      $bondcnt = 0; #total num bonds contains the implicit dnagling
bond of
      $croscnt = 0;
      $catcnt = 0;
      for ($i=0; $i< $numatoms; $i++){
        $temp =<XYZ> ;
        @t = split (" ", $temp);
        $tag = $t[0];
        $mol[$tag] = $t[1];
```

```
        $type[$tag] = $t[2];
        $q[$tag] = $t[3];
        $x[$tag] = $t[4];
        $y[$tag] = $t[5];
        $z[$tag] = $t[6];

        #$x[$tag] = ($t[3]-$xboxmin)/($xboxmax-$xboxmin);
        #$y[$tag] = ($t[4]-$yboxmin)/($yboxmax-$yboxmin);
        #$z[$tag] = ($t[5]-$zboxmin)/($zboxmax-$zboxmin);
      }
    }

  }
}
print ("finished xyzfile reading\n");

# atom position are now in memory and can be used for topology updates
if need be (this is not implemented yet)


# we now start making a topology list for a data file to be input from
lammps it uses nothing but bonding info.

$test = 0;

# initial listspace for bond of $i+1
for ($i=0; $i<$numatoms; $i++){
 @tmp =();
 @list = ();
 $list[$i]= [@tmp];
}

while (<BND>) {
  if ($test == 0){
    $temp = $_;
    @t = split (" ", $temp);
    if ($t[0]==$snapnum){
        $test =1;
    }

    if ($test == 1){
      $temp = <BND>;
      $temp =<BND>; # skip line ITEM: NUMBER OF BONDS
      $temp = <BND>;
      @t = split (" ", $temp);
      $numbonds = $t[0];
      print ("numbonds in file = $numbonds\n");
      # initialize a bondlist to hold max 2x num of bonds
      @bondlist = ();
      for ($i=0; $i<$numbonds; $i++){
          @bondtmp =();
          $bondlist[$i]= [@bondtmp];
       }

      <BND>; #skip line ITEM: BONDS
      $count = 0;
      for ($i=0; $i< $numbonds; $i++){
        $temp =<BND> ;
```

```
        @t = split (" ", $temp);
        $valid = 0;
        for ($j=0; $j<@{$list[$t[2]]}; $j++){
          if (${$list[$t[2]]}[$j] == $t[3]) {$valid=1;}
        }
        if ($valid == 0) {
          push (@{$list[$t[3]]}, $t[2]);
          push (@{$list[$t[2]]}, $t[3]);
          #next 3 lines makes a bondlist that will be used by the angle
section
          push (@{$bondlist[$count]}, $t[2]);
          push (@{$bondlist[$count]}, $t[3]);
          push (@{$bondlist[$count]}, $t[1]);
          #print ("type$t[1] atom1=$t[2] atom2=$t[3]\n");
        #print ("type = ${$bondlist[$count]}[2]
atom1=${$bondlist[$count]}[0],atom2=${$bondlist[$count]}[1]\n");
          $count++;
        }
      }
    }
  }
}

print ("finished reading bnd file\n");

$numbnd = $count;
print ("unique bonds = $numbnd\n");

# At this point there is all the data required to make any topology
updates as necessary. you need to import a periodic distance fn from
dump2pov.pl ~/bin/
# then we will look at a list of all bonds of a certain type and try
and exchange it with other nearby bonds of the same type
# also need a randomizer for these lists so that when reactions take
place they do so randomly

@bndtemp = ();
@tbndlist = ();
@marker = ();
$count = 0;
for ($i=0; $i<$numbnd;$i++){
  $btype = ${$bondlist[$i]}[2];
  if($btype == $rxnbondtype){
    # make a marker that count if a swap takes place
    $marker[$count]=0;
    $tbndlist[$count] = [@bndtemp];
    # save the 2 atoms in the bond and the position in global bond list
    push (@{$tbndlist[$count]}, ${$bondlist[$i]}[0]);
    push (@{$tbndlist[$count]}, ${$bondlist[$i]}[1]);
    push (@{$tbndlist[$count]}, $i);
    $count++;
  }
}

print ("finished creating list of size=$count of all
bondtype=$rxnbondtype\n");

# randomly shuffle the tbndlist to ensure mixing
```

```
for ($i=0;$i<@tbndlist;$i++){
  shuffle(\@tbndlist);
}
print ("shuffled the list \n");

@marker = ();
for ($i=0;$i<$count; $i++){
  $marker[$i]=0;
}

#check for reactions
$rxtcount =0;
for ($i=0; $i<$count; $i++){
  $b1 = ${$tbndlist[$i]}[0];
  $b2 = ${$tbndlist[$i]}[1];
  $pos1 = ${$tbndlist[$i]}[2];
  if ($marker[$i]==0){
    for ($j=0; $j<$count; $j++){
      if($marker[$j]==0 && $i!=$j){
        $c1 = ${$tbndlist[$j]}[0];
        $c2 = ${$tbndlist[$j]}[1];
        $pos2 = ${$tbndlist[$j]}[2];
        $d1 = getdistance($b1, $c1);
        $d2 = getdistance($b2, $c2);
        $d3 = getdistance($b1, $c2);
        $d4 = getdistance($b2, $c1);
        $case1 = $d1+$d2;
        $case2 = $d3+$d4;
        #print ("$i reacting $j/$count :  sqdist1 $case1 sqdist2 $case2
dist for  sqrxndist=$sqrxndist\n");
        if ($case1>$case2 && $case2< $sqrxndist){
          print ("swapping $b1-$b2 $i/$count with $c1-$c2
$j/$count\n");
          $marker[$j]=1;
          $marker[$i]=1;
          $bondlist[$pos1][1]=$c1;
          $bondlist[$pos2][0]=$b2;
          if($argc ==7) {
            $bondlist[$pos1][2]=$finbndtype;
            $bondlist[$pos2][2]=$finbndtype;
          }
          for ($i1=0; $i1<@{$list[$b1]};$i1++){
            if (${$list[$b1]}[$i1]==$b2) {${$list[$b1]}[$i1]=$c1;}
          }
          for ($i1=0; $i1<@{$list[$b2]};$i1++){
            if (${$list[$b2]}[$i1]==$b1) {${$list[$b2]}[$i1]=$c2;}
          }
          for ($i1=0; $i1<@{$list[$c1]};$i1++){
            if (${$list[$c1]}[$i1]==$c2) {${$list[$c1]}[$i1]=$b1;}
          }
          for ($i1=0; $i1<@{$list[$c2]};$i1++){
            if (${$list[$c2]}[$i1]==$c1) {${$list[$c2]}[$i1]=$b2;}
          }
          $rxtcount++;
          break;
        } elsif ($case2>$case1 && $case1< $sqrxndist){
          print ("swapping bond $b1-$b2 $i/$count with $c2-$c1
$j/$count\n");
```

```
          $marker[$j]=1;
          $marker[$i]=1;
          $bondlist[$pos1][1]=$c2;
          $bondlist[$pos2][1]=$b2;
          if($argc ==7) {
            $bondlist[$pos1][2]=$finbndtype;
            $bondlist[$pos2][2]=$finbndtype;
          }
          for ($i1=0; $i1<@{$list[$b1]};$i1++){
            if (${$list[$b1]}[$i1]==$b2) {${$list[$b1]}[$i1]=$c2;}
          }
          for ($i1=0; $i1<@{$list[$b2]};$i1++){
            if (${$list[$b2]}[$i1]==$b1) {${$list[$b2]}[$i1]=$c1;}
          }
          for ($i1=0; $i1<@{$list[$c1]};$i1++){
            if (${$list[$c1]}[$i1]==$c2) {${$list[$c1]}[$i1]=$b2;}
          }
          for ($i1=0; $i1<@{$list[$c2]};$i1++){
            if (${$list[$c2]}[$i1]==$c1) {${$list[$c2]}[$i1]=$b1;}
          }
          $rxtcount++;
          break;
        }
      }
    }
  }
}
print ("$rxtcount reactions completed and updated all topology
changes\n");


$count =0;
open (DATA, ">bndtemp");
print (DATA "\nBonds\n\n");
for($i=0; $i<$numbnd; $i++){
  $count++;
  $btype = ${$bondlist[$i]}[2];
  $bond1 = ${$bondlist[$i]}[0];
  $bond2 = ${$bondlist[$i]}[1];
  print (DATA "$count $btype\t$bond1\t$bond2\n")
}
# list now has the bond data and at a specific time step looks at the
bond profile and and creates a list of angles.
close (DATA);
print ("finished bndtemp formation\n");

$count =0;
open (DATA, ">angtemp");
print (DATA "\nAngles\n\n");
for ($i=1; $i<=$numatoms; $i++){
  $localbnd = @{$list[$i]};
  $a2=$i;
  $t2=$type[$a2];
  for ($j=0;$j<$localbnd; $j++){
    $a1=${$list[$i]}[$j];
    $t1=$type[$a1];
    for ($k=$j+1; $k<$localbnd; $k++){
      $a3=${$list[$i]}[$k];
```

```
      if ($a1 != $a3) {
        $t3=$type[$a3];
        $count++;
        $angletype = getangletype($t1,$t2,$t3);
        print (DATA "$count\t$angletype\t$a1\t$a2\t$a3\n");
      }
    }
  }
}
$numang = $count;
close (DATA);
print ("finished angtemp formation\n");

$count =0;
open (DATA, ">dihedtemp");
print (DATA "\nDihedrals\n\n");
# dihedral is p-b1-b2-q
for ($i=0; $i<$numbnd; $i++){
  $b1 = ${$bondlist[$i]}[0];
  $b2 = ${$bondlist[$i]}[1];
  $t2=$type[$b1];
  $t3=$type[$b2];
  for ($j=0;$j<@{$list[$b1]}; $j++){
    $p = ${$list[$b1]}[$j];
    $t1=$type[$p];
    for ($k=0;$k<@{$list[$b2]}; $k++){
      $q = ${$list[$b2]}[$k];
      $t4=$type[$q];
      # this $p>$q ensure each dihedral is counted only once
      if ($q!=$b1 && $p!=$b2){
        $count++;
        $dihedtype = getdihedtype($t1,$t2,$t3,$t4);
        print (DATA "$count\t$dihedtype\t$p\t$b1\t$b2\t$q\n");
      }
    }
  }
}
$numdih = $count;
close (DATA);
print ("finished dihedtemp formation\n");

$count =0;
open (DATA, ">improtemp");
print (DATA "\nImpropers\n\n");
# dihedral is p-c: q-c: r-c: c = center and p q r are connected atoms
for ($i=1; $i<=$numatoms; $i++){
  #$tempatm= $i;
  $localbnd = @{$list[$i]};
  $c = $i;
  $t2 = $type[$c];
  for ($j=0; $j<$localbnd; $j++){
    $p = ${$list[$i]}[$j];
    $t1 = $type[$p];
    for ($k=$j+1; $k<$localbnd; $k++){
      $q = ${$list[$i]}[$k];
      $t3 = $type[$q];
      for ($l=$k+1; $l<$localbnd; $l++){
        $r = ${$list[$i]}[$l];
```

```
        $t4 = $type[$r];
        $count++;
        $improtype = getimprotype($t1,$t2,$t3,$t4);
        print (DATA "$count\t$improtype\t$p\t$c\t$q\t$r\n");
      }
    }
  }
}
$numimp = $count;
close (DATA);

print ("finished improtemp formation\n");

printheader();
printatoms();


close (BND);
close (XYZ);
system "cat hdrtemp coeffs.txt atmtemp bndtemp angtemp dihedtemp
improtemp >mech.txt";
system "rm hdrtemp atmtemp bndtemp angtemp dihedtemp improtemp ";

exit();

sub printheader {
  my $header;
  $header = "Datafile at timestep $snapnum of $ARGV[1]\n";
  $header = "$header\n$numatoms\tatoms\n$numbnd\tbonds";
  $header =
"$header\n$numang\tangles\n$numdih\tdihedrals\n$numimp\timpropers\n";
  $header = "$header\n$atmtypes\tatom types\n$bndtypes\tbond
types\n$angtypes\tangle types\n$dihtypes\tdihedral
types\n$imptypes\timproper types\n";
  $header = "$header\n$xboxmin $xboxmax xlo xhi";
  $header = "$header\n$yboxmin $yboxmax ylo yhi";
  $header = "$header\n$zboxmin $zboxmax zlo zhi";
  open (HDR, ">hdrtemp");
  print (HDR "$header\n");
  close(HDR);
}


sub printatoms {
  my $i, $tag;
  open (ATM, ">atmtemp");
  print (ATM "\nAtoms\n\n");
  for ($i=0; $i < $numatoms; $i++){
    $tag = $i+1;
    print (ATM
"$tag\t$mol[$tag]\t$type[$tag]\t$q[$tag]\t$x[$tag]\t$y[$tag]\t$z[$tag]\
n");
  }
  close (ATM);
}

sub round {
  my $in, $out, $dec3;
```

```
  $in = $_[0];
  $dec3 = $in*1000 - int($in*1000);
  if ($dec3 > 5){
    $out = int($in*100+1)/100;
  } elsif ($dec3 < -5) {
    $out = int($in*100-1)/100;
  } else {
    $out = int($in*100)/100;
  }

  return $out;
}

sub getangletype {
  my $i1, $at1, $at2, $at3, $cat1, $cat2, $cat3, $cangtype;
  $at1 = $_[0];
  $at2 = $_[1];
  $at3 = $_[2];
  $cangtype = "NA";
  for ($i1=1; $i1<=$angtypes; $i1++){
    $cat1 = $angtypelist[$i1][0];
    $cat2 = $angtypelist[$i1][1];
    $cat3 = $angtypelist[$i1][2];
    if (($cat1==$at1 && $cat2==$at2 && $cat3==$at3) || (($cat1==$at3 &&
$cat2==$at2 && $cat3==$at1))){
      $cangtype = $i1;
    }
  }
  if ($cangtype == "NA") {print ("no angtype: $at1 $at2 $at3\n");}
  return $cangtype;
}

sub getdihedtype {
  my $i1, $at1, $at2, $at3, $at4, $cat1, $cat2, $cat3, $cat4,
$cdihtype;
  $at1 = $_[0];
  $at2 = $_[1];
  $at3 = $_[2];
  $at4 = $_[3];
  $cdihtype = "NA";
  for ($i1=1; $i1<=$dihtypes; $i1++){
    $cat1 = $dihtypelist[$i1][0];
    $cat2 = $dihtypelist[$i1][1];
    $cat3 = $dihtypelist[$i1][2];
    $cat4 = $dihtypelist[$i1][3];
    if (($cat1==$at1 && $cat2==$at2 && $cat3==$at3 && $cat4==$at4 ) ||
(($cat1==$at4 && $cat2==$at3 && $cat3==$at2 && $cat4==$at1))){
      $cdihtype = $i1;
    }
  }
  if ($cdihtype == "NA") {print ("no dihtype: $at1 $at2 $at3 $at4\n");}
  return $cdihtype;
}

sub getimprotype {
  my $i1, $at1, $at2, $at3, $at4, $cat1, $cat2, $cat3, $cat4,
$cimptype;
  $at1 = $_[0];
```

```
  $at2 = $_[1];
  $at3 = $_[2];
  $at4 = $_[3];
  $cimptype = "NA";
  for ($i1=1; $i1<=$imptypes; $i1++){
    $cat1 = $imptypelist[$i1][0];
    $cat2 = $imptypelist[$i1][1];
    $cat3 = $imptypelist[$i1][2];
    $cat4 = $imptypelist[$i1][3];
    if ($cat2==$at2 && (($cat1==$at1 && $cat3==$at3 &&
$cat4==$at4)||($cat1==$at4 && $cat3==$at1 && $cat4==$at3)||($cat1==$at3
&& $cat3==$at4 && $cat4==$at1)
                      ||($cat1==$at1 && $cat3==$at4 &&
$cat4==$at3)||($cat1==$at4 && $cat3==$at3 && $cat4==$at1)||($cat1==$at3
&& $cat3==$at1 && $cat4==$at4))){
      $cimptype = $i1;
    }
  }
  #if ($cimptype == "NA") {print ("no imptype: $at1 $at2 $at3
$at4\n");}
  return $cimptype;
}

sub getdistance {
  my $sqdist, $n1, $n2, $dx, $dy, $dz;
  $n1 = $_[0];
  $n2 = $_[1];
        $dx = ($x[$n1]-$x[$n2])/$xbox;
        $dy = ($y[$n1]-$y[$n2])/$ybox;
        $dz = ($z[$n1]-$z[$n2])/$zbox;
        #print ("$dx $dy $dz\n");
        if ($dx >0.5) {$dx -= 1;}
        elsif ($dx < -0.9) {$dx += 1;}
        if ($dy >0.5) {$dy -= 1;}
        elsif ($dy < -0.9) {$dy += 1;}
        if ($dz >0.5) {$dz -= 1;}
        elsif ($dz < -0.9) {$dz += 1;}
        $sqdist = $dx*$dx*$xbox*$xbox + $dy*$dy*$ybox*$ybox +
$dz*$dz*$zbox*$zbox;
   return $sqdist;
}

# Shuffle taken in toto from
http://www.unix.org.ua/orelly/perl/cookbook/ch04_18.htm
sub shuffle {
    my $array = shift;
    my $i2;
    for ($i2 = @$array; --$i2; ) {
        my $j2 = int rand ($i2+1);
        next if $i2 == $j2;
        @$array[$i2,$j2] = @$array[$j2,$i2];
    }
}
```

Topoinfofile:

```
4 atom types
   11 bond types
  18 angle types
  34 dihedral types
  14 improper types

atmtype
1 sp3Ch
2 sp2C
3 sp3CH2
4 H


bndtype type1 type2
1       1       1
2       1       3
3       1       4
4       1       2
5       2       2
6       2       4
7       3       4
8       2       3
9       2       2
10       2       2
11       2       2

sp3ch=1: sp2C=2: sp3ch2=3: H=4
angtype     typea typeb typec
1     1     1     1
2     1     1     3
3     1     1     4
4     3     1     4
5     1     1     2
6     2     1     3
7     2     1     4
8     1     2     2
9     1     2     4
10    2     2     4
11    1     3     1
12    1     3     4
13    4     3     4
14    1     3     2
15    2     3     4
16    2     2     3
17    3     2     4
18    4     2     4

1 = sp3CH: 2 = sp2C: 3 = sp3CH2: 4 = H (this is not a united atom
simulation, sp3CH implies the C is sp3 and has only one H)
dihtype     typea typeb typec typed
1     1     1     1     2
2     1     1     1     3
3     1     1     1     4
4     2     1     1     3
```

```
5     3     1     1     3
6     3     1     1     4
7     2     1     1     4
8     4     1     1     4
9     1     1     1     1
10    1     1     3     2
11    1     1     3     4
12    4     1     3     2
13    4     1     3     4
14    1     1     2     2
15    1     1     2     4
16    3     1     2     2
17    3     1     2     4
18    4     1     2     2
19    4     1     2     4
20    2     1     3     1
21    2     1     3     4
22    1     1     3     1
23    4     1     3     1
24    1     2     2     1
25    1     2     2     4
26    4     2     2     4
27    2     1     1     2
28    2     2     3     1
29    4     2     3     1
30    2     2     3     4
31    4     2     3     4
32    1     2     2     3
33    3     2     2     4
34    3     2     2     3

sp3Ch=1: sp2C=2: sp3CH2=3: H=4
imptype     typea typeb typec typed
1     1     2     2     4
2     2     2     3     4
3     1     1     1     3
4     1     1     1     4
5     1     1     3     4
6     1     1     2     3
7     1     1     2     4
8     2     1     3     4
9     1     1     1     2
10    1     3     1     4
11    1     3     4     4
12    1     3     2     4
13    2     3     4     4
14    4     2     2     4
```